UNIVERSITY OF CALIFORNIA,
IRVINE

Chemical Investigations of Sources and Formation Processes of Ultrafine Aerosol Precursors

DISSERTATION

submitted in partial satisfaction of the requirements
for the degree of

DOCTOR OF PHILOSOPHY

in Chemistry

by

Michelia Dam

Dissertation Committee:
Professor James N. Smith, Chair
Professor Ann Marie Carlton
Professor Sergey Nizkorodov

2023

DEDICATION

for Mom & for Nguyên

a foreign place, the saving

grace was the feeling

TABLE OF CONTENTS

LIST OF FIGURES

LIST OF TABLES

ACKNOWLEDGMENTS

Thank you to Jim, the captain of the ultrafine ship, who has always guided us with an incredible depth of knowledge, skill and expertise. Who is always short on time, but can always be found in lab. Who is amazingly resourceful and finds one CPC on eBay every year, on average. Who has repaired said CPCs and every other instrument in lab countless times. Who can climb a mountain with impressive speed and has logged an insane amount of miles on his bike. Who can make really difficult chemical measurements in any environment. Who treats us as humans and supports our endeavors. Who always trusted my process, however unorthodox. Who built a lab that allows everyone to thrive.

Thank you to Annalise, for pushing me off the metaphorical branch and showing me that the air was a place for someone like me. Thank you to Kim, Evelin, Mei, Patricia, Tom, Rasha, Kenia and Tina for sharing stories under the hood, which I have never forgotten.

Thank you to Julie and Andrey and Emily for your enthusiasm regarding nitrogen, swagelok, tacos and hot sauce. Thank you for all the support and brain-power on the nitrate project.

Thank you to all members of AirUCI, especially Professor Finalysonn-Pitts, Professor Guenther, Professor Nizkorodov, Professor Carlton and Melissa Sweet for all the collaborations and support. Thank you to Vero, for your constant commitment to making good measurements. For your overwhelming generosity with time and your joyfullness. Thank you to Lisa, for your incredible thoughtfulness and creativity regarding aerosol chemistry. For your honesty and humor.

Thank you to Mike Lawler, for many conversations, about science among other things, that I store in my collection as good memories. For very patiently imparting so much knowledge to us. To John Ortega, to all your hard work on the GC system and your excellent tutelage. Thank you to Nanna, for being a truly inspirational scientist. Thank you to Paulus, for your dad jokes and massively wrinkled brain. For the kindness and joy with which you conduct science and life.

Thank you to Danielle, who was essential for making all the projects listed here possible. Who is a magical human full of whimsy and knowledge. Who personifies lab objects more than anyone I know. Thank you to Sabrina, for asserting dominance over the instruments but treating people with great care. For all the invaluable time we spend understanding things together. Thank you to Hayley, for your advocacy in all things and your awareness of the human aspect of science. For the hot goss and culture. To Deanna, for your amazing determination and positivity. For the real housewives and puppy updates. Thank you to Jeremy for your earnestness and perspective. For your Labrador energy. Thank you to Adam, who is brilliant and warm, with humility that obscures his excellence. Who adds such immense joy to life and science.

Thank you to Madi and to Zac, for making sharing an apartment a wonderful experience. For being responsible for lots of positive times during deep pandemic and afterwards. Thank

you to Audrey, Ricki, David Buckley and Nguyen, for all the miles you traveled during these years to stay connected. Your friendship has always kept me grounded and sustained. Thank you to the supportive community that exists in UCI Chemistry, including but not limited to Gabe, Dorothy, Anneka, Joe, Paul, Tristen and Cynthia.

Thank you to the DamBSHo+ family, who have given me hot assists since before I was born. Thank you to my brother, Orion, who enriches the lives of everyone around him. At my most, I find myself seeing the world as he does. Thank you to my dad, who gave me his name and all the stories that come with it, which have been fundamental in my pursuit of science and happiness.

Chapter 3 of this dissertation is a reprint of the material as it appears in: "Observations of gas-phase products from the nitrate-radical-initiated oxidation of four monoterpenes." *Atmos. Chem. Phys.* **2022**. 22, 9017–9031. DOI: https://doi.org/10.5194/acp-22-9017-2022., used with permission from Coppurnicus Publications. The co-authors listed in this publication are Danielle Draper, Andrey Marsavin, Juliane Fry, and James N. Smith. Chapter 4 of this dissertation is a reprint of the material as it appears in: "Formation of Highly Oxidized Organic Compounds and Secondary Organic Aerosol from a-Thujene Ozonolysis" *J. Phys. Chem. A.* Accepted for publication. **2023**. https://doi.org/10.1021/acs.jpca.3c02584., used with permission from American Chemical Society Publications. The co-authors listed in this publication are Adam E. Thomas and James N. Smith. Thank you to the US National Science Foundation (NSF; grant no. AGS-1762098) and from the US Department of Energy (DOE; grant no. DE-SC0019000) for funding the monoterpene oxidation projects, and the California Department of Justice for funding the brake-wear project.

VITA

Michelia Dam

EDUCATION

Doctor of Philosophy in Chemistry **2018–2023**
University of California, Irvine *Irvine, CA*

Bachelor of Science in Chemistry **2015–2018**
San Jose State University *San Jose, CA*

RESEARCH EXPERIENCE

Graduate Research Assistant **2018–2023**
University of California, Irvine *Irvine, California*

Principal Investigator: James N. Smith

- Developed an iodide (I-) reagent source and operational method for a high resolution chemical ionization mass spectrometer (CIMS, Aerodyne LTOF) with a home-built transverse ion inlet.
- Measured reaction products in the gas and particle phase with a suite of analytical techniques (high resolution mass spectrometry (NO_3- and I- CIMS), SMPS, GC-FID, FTIR).
- Elucidated the oxidation mechanisms of night time chemistry of the atmosphere by designing and implementing laboratory chamber experiments that simulate nitrate radical-induced oxidation of monoterpenes.
- Collaborated with Prof. Julianne Fry (Reed College) on kinetic modeling of the chemical system, creating a more robust understanding of the chemical mechanisms.
- Measured chemical composition of gases (NO_3- and I- CIMS) emitted from vehicle brake wear generated from a home-built brake dynamometer system.
- Measured the chemical composition of urban gases and ultrafine particles at a field site near Houston, TX from early July to late August of 2022.
- Operated and maintenanced instruments, including mass spectrometers that measured gas and particle composition (NO_3-CIMS, TDCIMS) and aerosol particle counters located inside a rented mobile office trailer.
- Measurements implicated sulfuric acid and oxidized organics as major precursors to nanoparticle formation in the Houston atmosphere. Project was part of a larger field campaign funded by the US Department of Energy, in collaboration with Prof. Don Collins (UC Riverside).

Undergraduate Research Assistant **2016–2018**
San Jose State University *San Jose, California*

Principal Investigator: Annalise Van Wyngarden

- Designed experiments for the measurement of optical properties (absorbance, refractive index) of sulfuric acid/organic solutions, representative of aerosol found in the upper stratosphere/lower troposphere, using UV/vis spectroscopy and other analytical techniques to evaluate their radiative effects.
- Sulfuric acid/organic solutions were found to be significantly more absorbing than pure sulfuric acid in atmospherically relevant wavelengths, showing the importance of understanding the impact of aerosol composition on climate.
- Performed computational modeling of muon-bonding sites in magnesium tetrahedron using Python in order to assess the physical feasibility of earthquake-precursor (MgO-) detection by muon bombardment.
- The muon was found to localize approximately one angstrom away from the oxygen atom in our computational model, allowing us to approximate and predict the measurable observation in an analogous physical system.

TEACHING EXPERIENCE

Chemistry Teaching Assistant
University of California, Irvine *Irvine, CA*

Majors Quantitative Analytical Chemistry, M2C (remote) **Spring 2021**

- Facilitated two weekly discussion sections; developed new midterm projects and corresponding rubrics to replace traditional exams; graded projects using Gradescope.

Majors Quantitative Analytical Chemistry Lab, M3LC (in-person) **Spring 2019**

- Led two four hour laboratory sections weekly; taught analytical lab skills; graded lab reports using Electronic Lab notebook (ELN), exams, and weekly experiment presentations; held weekly office hours; beta-tested experiments before classes.

General Chemistry Lab for Engineers, 1LE (in person) **Winter 2019**

- Taught chemical lab skills to engineering students; graded lab reports using Electronic Lab notebook (ELN), exams, and weekly experiment presentations; held weekly office hours

General Chemistry for Non-majors, 1A (in person) **Fall 2018**

- Taught a 1 hour lecture for a class of 400 students on introductory quantum mechanics, facilitated four discussion sections per week; held weekly office hours; drafted exam practice material; graded exams.

LEADERSHIP EXPERIENCE

President for the UCI AAAR Student Chapter **2021–2022**

- Initiated and facilitated monthly officer meetings. Executed professional development, social, technical, and diversity focused events geared for students and post-docs. Submitted annual reports to secure funding for events.

Internal AirUCI Symposium Organizer **2021–2022**

- Sole coordinator of this seminar series until Fall 2022; co-coordinator onwards. Secured funding for seminars. Solicited and hosted research seminar talks from graduate students, post-doctoral researchers and project scientists from various departments (chemistry, earth systems science, toxicology, engineering, etc.).

ACS Mentor for Undergraduate Transfer Students **2021**

- Guided community college students through the transfer process to a four-year university
- Reviewed application materials and advised an individual student from the initial application process through to transfer

Social Event Coordinator for the UCI AAAR Student Chapter **2019-2020**

- Led the development of professional events for graduate students and post-doctoral researchers. Composed professional communications (emails, letters, flyers) to the community for student chapter events.

Mentor for UCI Chemistry Peer Mentor Program **2019-2020**

- Guided incoming first year PhD students in the Chemistry department at UCI by advising and providing resources for first year activities, such as group rotations, teaching, classes and research.

Member of Student Affiliated American Chemical Society **2016-2018**

- Participated in STEM outreach programs in the community (science fairs, informational gatherings, etc.), specifically working with elementary school children in public school.

AWARDS

NSF Graduate Research Fellowship Honorable Mention **2019**
ACS Undergraduate Research Award **2018**

SKILLS

High Resolution Mass Spectrometry (MS): TOF analyzers, TDCIMS, nitrate-CIMS, iodide-CIMS, LC-MS

Other Instrumentation: Particle sizing and counting (APS, SMPS, DMA, CPC), collection (S3, MOUDI), and analysis (GC-FID, FTIR, UV-vis spectroscopy)

Maintenance Skills: high-vacuum pumps, ionization inlet characterization, electrical troubleshooting

Hardware: electrical repair (soldering), rack design and mounting for instrument transport

Software: Igor Pro, Labview, Tofware (Igor Pro), Tern (Igor Pro), ChemDraw, LaTeX, Microsoft Office

PUBLICATIONS

1. Dam, M.; Thomas, A. E.; Smith, J. N. "Formation of Highly Oxidized Organic Compounds and Secondary Organic Aerosol from a-Thujene Ozonolysis" *JPCA* Accepted. 2023.
2. Dam, M.; Draper, D. C.; Marsavin, A.; Fry, J; Smith, J. N.; "Observations of gas-phase products from the nitrate-radical-initiated oxidation of four monoterpenes" *Atmos. Chem. Phys.* 2022.
3. Smith, J.N.; Draper, D.C.; Chee, S.; Dam, M.; Glicker, H.; Myers, D.; Thomas, A.; Lawler, M.J.; Myllys, N. "Atmospheric clusters to nanoparticles: Recent progress and challenges in closing the gap in chemical composition." *Journal of Aerosol Science.* 2020. 153.

PRESENTATIONS * indicates presenter

1. *Dam, M.; Draper, D. C.; Lawler, M.; Smith, J. N. "Questions about NO3- and I- reagent ion sensitivity to nitrate radical-initiated monoterpene oxidation products and TDCIMS mysteries regarding thermal desorption and decomposition." Aerodyne CIMS Users Meeting, 2020.

POSTERS * indicates presenter, ⋆ indicates award

1. *Dam, M.; Thomas, A. E.; Smith, J. N. "Observations of Gas and Particle Phase Composition of a-Thujene Ozonolysis Products." American Association for Aerosol Research Conference, 2022.
2. ⋆Thomas, A. E; Lee, M.; Perraud, V.; Bauer, P.; Dam, M.; Finlayson-Pitts, B. J.; Smith, J.N. "Organic Composition of Ultrafine Aerosol Particles Generated from the Wear of Automotive Brake Pads." American Association for Aerosol Research Conference, 2022.
3. Thomas, A. E; Perraud, V.; Dam, M.; Smith, J.N. "Molecular Structure Characterization of Nanoparticles Formed from the Ozonolysis of a-Pinene" American Association for Aerosol Research Conference, 2021.
4. *Dam, M.; Draper, D. C.; Marsavin, A.; Fry, J; Smith, J. N. "Comparison of Nitrate Radical Initiated Oxidation of Four Monoterpenes in a Laboratory Chamber Study to Gain Mechanistic Insight." American Association for Aerosol Research Conference, 2021.
5. *Dam, M.; Van Wyngarden, A.; et al. "Optical Properties of Mixed Sulfuric Acid/Organic Aerosols in the Upper Troposphere and Lower Stratosphere: Implications for Climate." American Chemical Society Northern California Undergraduate Research Symposium, May 2017.
6. *Dam, M.; Boekema, C.; et al. "Muon-bonding site search in MgO: Possible implications for earthquake-precursor detection." American Physical Society Far West Meeting, November 2017.
7. *Dam, M.; Van Wyngarden, A.; et al. "Optical Properties of Organic/Sulfuric Acid Solutions at Upper Troposphere/Lower Stratosphere Aerosol Acidites: Implications for Climate." American Geophysical Union Meeting, December 2017.

ABSTRACT OF THE DISSERTATION

Chemical Investigations of Sources and Formation Processes of Ultrafine Aerosol Precursors

By

Michelia Dam

Doctor of Philosophy in Chemistry

University of California, Irvine, 2023

Professor James N. Smith, Chair

Accurately representing the sources of important precursor gases for new particle formation and their chemical reactions in the atmosphere are critical for developing a robust understanding of the impacts of ultrafine particles on climate and health. Many types of compounds contribute to these nucleation and growth processes, including inorganic acids, bases and low-volatility organic compounds. Both formation of these compounds in the atmosphere and the processes by which they are converted to ultrafine particles depend greatly on their composition. Therefore, in this dissertation, these sources and processes were investigated using measurements of chemical composition, specifically chemical ionization mass spectrometry (CIMS). CIMS was used to measure important precursor gases for ultrafine particle formation and growth in controlled laboratory chamber studies for three separate chemical systems.

In Chapter 2, the chemical composition of gasses emitted from vehicle brake wear were measured using both nitrate reagent ion (nitrate-CIMS) and iodide reagent ion (iodide-CIMS). Gases, coarse-mode particles and ultrafine particles were generated from a home-built brake dynamometer system, which simulated moderate and heavy braking conditions. The brake pad formulation (ceramic vs semi-metallic), degree of wear (new, gently worn, heavily worn), and temperature of the brake rotor influenced measured gaseous emissions. A critical temperature range was observed for ultrafine particle formation. These critical temperatures were found to be lower for ceramic brake pads (100-140 °C) than semi-metallic brake pads (140-200 °C), and increase as the brake pads became worn. High

concentrations of sulfuric acid and sulfur trioxide were generated during heavy braking conditions at high temperatures, and were more abundantly emitted by the semi-metallic pads than the ceramic. Moderate braking conditions produced NOx, CO, inorganic nitrogen compounds (HONO, N_2O_5), oxidized organics and organic acids. Emissions from different brake pad formulations and degrees of wear were highly variable, emphasizing the importance of representing brake-wear emissions over the lifetime of a brake pad for future control strategies.

In Chapter 3, the effects of monoterpene structure on nitrate radical-induced oxidation mechanism of four monoterpenes (α-pinene, β-pinene, Δ-carene, α-thujene) was investigated by conducting laboratory chamber experiments. Oxidized reaction products were measured with nitrate-CIMS. The major gas-phase species produced in each system were distinctly different, showing the effect of monoterpene structure on the oxidation mechanism and further elucidated the contributions of these species to particle formation and growth. Measured effective O:C ratio of reaction products were anti-correlated to new particle formation intensity and number concentration for each system; however, monomer:dimer ratio of products had a small positive trend. Gas phase yields of oxidation products correlated with particle number concentrations for each monoterpene system, with the exception of α-thujene, which produced a considerable amount of low volatility products but no particles. The lack of measurable new particle formation in spite of the presence of these dimers indicates a more complex relationship between highly oxidized organic compounds and new particle formation.

In Chapter 4, the formation of low-volatility gasses and new particle formation from ozonolysis of α-thujene was observed in laboratory chamber studies. This system was found to produce lower yields of particles at all mass loadings compared to α-pinene ozonolysis systems. The unique structure of α-thujene led to the competitive production of semi-volatile fragment compounds that reduced the overall volatility of the oxidized products. Theoretical growth rates (on the order of nm min^{-1}) calculated from volatility-parameterized organics underpredicted measured growth rates. However, the simple condensational growth model that was used did not account for the irreversible partitioning of semi-volatile organics, which were abundantly produced by this system.

Chapter 1

Introduction

1.1 List of Research Articles

This thesis consists of an introduction and three research articles. These papers are outlined below.

I. **Dam, M.**; Perraud, V.; Thomas, A.E.; Wingen, L.; Finlayson-Pitts, B.J.; Smith, J.N. "Brake-wear emissions of sulfuric acid, sulfur trioxide, inorganic nitrogen species and organic acids." Manuscript in preparation.

II. **Dam, M.**; Draper, D.C.; Marsavin, A.; Fry, J.; Smith, J.N. "Observations of gas-phase products from the nitrate-radical-initiated oxidation of four monoterpenes." *Atmos. Chem. Phys.* **2022**. 22, 9017–9031. DOI: https://doi.org/10.5194/acp-22-9017-2022.

III. **Dam, M.**; Thomas, A.E.; Smith, J.N. "Formation of Highly Oxidized Organic Compounds and Secondary Organic Aerosol from a-Thujene Ozonolysis" *J. Phys. Chem. A.* Accepted for publication. **2023**. https://doi.org/10.1021/acs.jpca.3c02584.

1.2 Background

1.2.1 Impacts of atmospheric aerosols on health and climate

Atmospheric aerosols are suspensions of particles and gases which have been measured globally, in almost any environment. The term, "aerosol" was first included in the Oxford English Dictionary one hundred years ago, and the original source of this term was attributed to a manuscript published in the Proceedings of the Royal Society in 1923 (Whytlaw-Gray et al., 1923). This manuscript reported on early measurements of aerosol particles from various systems, known during that time as "smokes," and detailed three key challenges in understanding aerosol processes: 1. generation of aerosol particles, 2. measurement of particle concentration, 3. measurement of particle size. Since the 1920s, many advancements have been made by the aerosol science community in all of these areas of study, but the fundamental implications of these questions still remain: formation processes directly impact concentration and size of aerosol particles, which govern their atmospheric interactions. Understanding these extremely complex atmospheric interactions is essential for assessing the broader impacts of aerosol on climate and health. Many of these impacts have been elucidated in modern times, yet large uncertainties remain, especially for particles in the ultrafine diameter range.

Ultrafine particles are smaller than 100 nm in diameter, which can make up a significant portion of the measured number concentrations of particles in the troposphere (Kulmala et al., 2004; Finlayson-Pitts and Pitts, 2000). Their small size allows them to deposit more deeply in the lung upon inhalation than coarse-mode (2-10 micron) particles, which only make it to the upper respiratory tract. Once deposited, ultrafine particles can traverse membrane barriers into blood and translocate to almost all organs in the body (Schraufnagel, 2020; Allen et al., 2017; Oberdörster et al., 2004). Therefore, respiratory exposure to ultrafine particles can lead to increased inflammation and respiratory disease. In addition to adverse health effects, ultrafine particles also significantly impact Earth's climate through various atmospheric interactions. With diameters smaller than emitted solar wavelengths, ultrafine particles do not directly interact with incoming radiation. However,

ultrafine particles are significant precursors for larger particles, which can absorb or scatter solar radiation, depending on their size and composition (Kulmala et al., 2014). Scattering radiation leads to overall cooling effects on climate, while absorbing radiation leads to overall warming. Additionally, ultrafine particles are estimated to produce 50% of global cloud condensation nuclei, aerosol particles that can uptake water and form cloud droplets (Gordon et al., 2017; Merikanto et al., 2009; Pierce and Adams, 2009; Westervelt et al., 2013). The complexities of aerosol-cloud interactions are responsible for the largest uncertainties in climate models that predict global radiative forcing in the Sixth Assessment Report from the Intergovernmental Panel on Climate Change in 2021 (Forster et al., 2023). Therefore, it is crucial to understand the formation processes of these ultrafine particles to narrow the uncertainty in our overall understanding of aerosol impacts on climate and health. Though elucidating these processes is an active area of research, many advances have been made in the past couple decades that have illuminated some key ultrafine particle formation pathways. Underlying the physical properties of these aerosol particles are chemically-driven processes, which require molecular level investigations.

1.2.2 Formation of atmospheric ultrafine particles

Aerosol particles can be directly emitted in the atmosphere, or formed from secondary processes (Finlayson-Pitts and Pitts, 2000). Coarse-mode particles are mostly primarily emitted by mechanical processes, though these particles can also coagulate with other particles and serve as condensation sinks for atmospheric gases. Conversely, the majority of tropospheric ultrafine particles are formed through secondary processes in the atmosphere (Baccarini et al., 2020; Lee et al., 2019). New particle formation is one such secondary process that begins with nucleation, the collision of gas species to form clusters, followed by the growth of those clusters into ultrafine particles. Atmospheric cluster formation has been observed to occur perpetually in most environments, with lifetimes on the order of minutes, but growth of these clusters must effectively outweigh cluster loss mechanisms in order for clusters to grow to particles (Kulmala et al., 2004). Atmospheric clusters are able to form and grow when the intermolecular forces holding the gas molecules together are stronger than evaporative forces (Kirkby et al., 2011; Pichelstorfer et al., 2018; Zhang et al., 2012;

Whitby, 1978). At small sizes, the surface curvature of the particles becomes significant, resulting in fewer molecular interactions on the surface and making evaporation of gas constituents easier for ultrafine particles than coarse mode particles and bulk solutions. This is known as the Kelvin effect. These growth processes also compete with coagulation as well as loss of ultrafine particles to larger-sized particles, the latter of which can occur rapidly given the large differences in Brownian motion that favor deposition by diffusion (Cai and Jiang, 2017; Kuang et al., 2010).

In order to overcome high evaporation rates, a supersaturation of precursor gases is required for vapor pressure-driven nucleation. The direct condensation of low-volatility organics and halogenated organics is thought to play a major role in nucleation, as these species have been frequently measured in atmospheric ultrafine particles (Figure 1.1, Ehn et al. (2014); Smith et al. (2021, 2008)). Additionally, another method in which nucleation can occur is through reactive uptake. Volatile gas species can react upon collision, forming new species with reduced volatility. A important system that undergoes reactive uptake is the stabilization of volatile bases by various inorganic acids (H_2SO_4, HNO_3, MSA) in the atmosphere (Smith et al., 2021; Berndt et al., 2010). Sulfuric acid is regarded as a dominant constituent for new particle formation in urban areas, as measurements of gaseous sulfuric acid often trend with observed new particle formation events in ambient air (Almeida et al., 2013; Kirkby et al., 2011; Sipilä et al., 2010; Weber et al., 1995). Observed ultrafine particle growth rates from ambient measurements are under-predicted when considering nucleation from only sulfuric acid condensation, indicating that the presence of other compounds is necessary to bridge the gap between observations and predictions.

Although new particle formation has been often observed in clean environments with low concentrations of ambient particles, such as the remote Boreal forest and the Arctic, it has also been observed and predicted to occur in polluted industrial and residential areas (Spracklen et al., 2008; Kulmala et al., 2014). In continental environments, nucleation produced concentrations of particles are of the order of 10^6 to 10^7 cm^3 when considering sulfuric acid and organic constituents (Kulmala et al., 2014). The diversity of gaseous precursor compounds that contribute to new particle formation and growth, their associated emission sources, and subsequent chemical reactions in the atmosphere make up a highly complex system that is difficult to comprehensively represent in models. This is

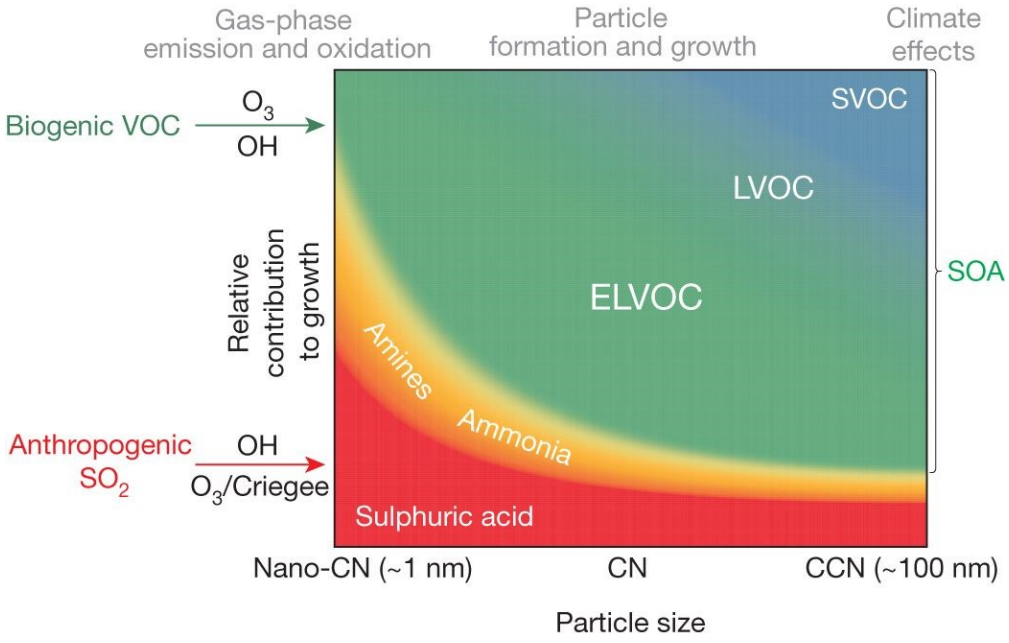

Figure 1.1: Schematic representation of size-dependent contributions of gas precursors to ultrafine particle growth and climate effects. Reproduced from Ehn et al. (2014).

especially challenging considering each of the various precursor gases are formed through secondary oxidation processes in the atmosphere, making characterization of these oxidant species and volatile gases necessary. Fundamentally, each of these areas need specific investigation before interactions between them can be understood. In this dissertation, a chemical composition perspective on these various aspects is presented. Controlled studies that simulate the chemical processes of interest were performed using laboratory chambers, and gaseous precursors for ultrafine particle formation were measured using a chemical ionization mass spectrometer (CIMS). In Chapters 3 and 4, the formation of low-volatility organics from structural isomers of volatile organic compounds (VOCs) was studied in detail. In Chapter 2, the gas emissions of one novel source of ultrafine particles, vehicle brake-wear, was characterized for the first time.

1.2.3 Sources of ultrafine aerosol precursors

Gaseous sulfuric acid is recognized as a major participant (Figure 1.1) in nucleation and cluster growth. Sulfuric acid is formed in the atmosphere from oxidation of SO_2, forming sulfur triox-

ide (SO_3), which can react with water or other acids to form sulfuric acid (Finlayson-Pitts and Pitts, 2000). This reaction scheme is shown below. During the daytime, hydroxyl radical (OH) is considered the most important gas-phase oxidant species. OH is predominantly generated from photolysis of ozone and is thus considered an important daytime oxidant. Nighttime sources of SO_2 oxidants are not well characterized, but can include stabilized Criegee intermediates formed from ozonolysis of alkenes (Sipilä et al., 2014). Tropospheric SO_2 is emitted in high concentrations from coal-fired power plants, diesel trucks and other industrial facilities, but can also come from biogenic sources, like marine emissions and downward mixing of stratospheric SO_2 from volcanic eruptions (Finlayson-Pitts and Pitts, 2000). In general, sulfuric acid is most concentrated in urban areas, but its formation can be affected by both anthropogenic and biogenic gaseous emissions from many different sources. Due to the diverse pathways of formation, understanding the various sources of the gaseous chemical constituents for sulfuric acid formation is crucial for predicting new particle formation events. As regulations continue to limit sulfur-containing fossil fuel combustion in many developed nations, new sources of atmospheric sulfur emissions are increasing in relevance.

$$OH + SO_2 + M \longrightarrow HOSO_2 + M \quad \text{(R1)}$$

$$HOSO_2 + O_2 \longrightarrow HO_2 + SO_3 \quad \text{(R2)}$$

$$SO_3 + H_2O \longrightarrow H_2SO_4 \quad \text{(R3.1)}$$

$$SO_3 + \text{acid} \longrightarrow H_2SO_4 \quad \text{(R3.2)}$$

1.2.4 Brake-wear: an significant source of unrepresented emissions

A source of emissions that is recently gaining attention from the aerosol science community and air quality regulation agencies is non-tailpipe vehicle emissions. This is an umbrella term that en-

compasses emissions from tire-wear, brake-wear and road dust re-suspension (Fussell et al., 2022; OECD, 2020). Non-tailpipe emissions are estimated to significantly contribute to traffic emissions of particulate matter and are predicted to become dominant sources of traffic emissions of PM 10 and PM2.5 in the near future (Figure 1.2) as the vehicle fleet transitions from combustion to electric engines (Piscitello et al., 2021). Traffic emissions are linked to toxicity and increase in childhood asthma, resulting in negative health impacts that disproportionately affect socioeconomically disadvantaged communities (Tessum et al., 2021; Gauderman et al., 2005; Malachova et al., 2016). Therefore, there is both an urgency and ethical motivation to characterize non-tailpipe emissions and quantify the extent to which they contribute to traffic emissions as a whole. In Chapter 2, we focused our investigations on emissions from vehicular brake wear. Formation of ultrafine particles has been reported from braking processes in laboratory studies (Namgung et al., 2016; Nosko et al., 2017; Park et al., 2021; Nosko and Olofsson, 2017), and ultrafine particles have been measured from roadways (Lv et al., 2020; zum Hagen et al., 2019), but interference from tailpipe and other urban sources makes source apportionment of roadway emissions challenging. Additionally, a lack of chemical composition characterization of emitted gasses from brake-wear leaves a knowledge gap that obscures understanding of their formation processes. To fill that gap and gain insight on how brake-wear produces ultrafine particles, we measured the chemical composition of gas emissions from braking processes simulated with a home-built brake dynamometer system. The details for those experiments are discussed in Chapter 2. Important precursor gases for both sulfuric acid formation and other constituents of ultrafine aerosol (low-volatility organics, inorganic nitrogen) were measured from simulated braking. The significance of organics in ultrafine particle formation and growth is discussed in the next section.

1.2.5 Formation of low-volatility organics from VOC oxidation

As clusters grow from the nucleation mode to cloud condensation nuclei, the role that low-volatility organic compounds play in growth increases (Ehn et al., 2014). Oxidation reactions of VOCs in the atmosphere form secondary organic aerosol (SOA), which make up a large fraction of ultrafine aerosol particles (Jimenez et al., 2009; Hallquist et al., 2009). An important process for decreasing

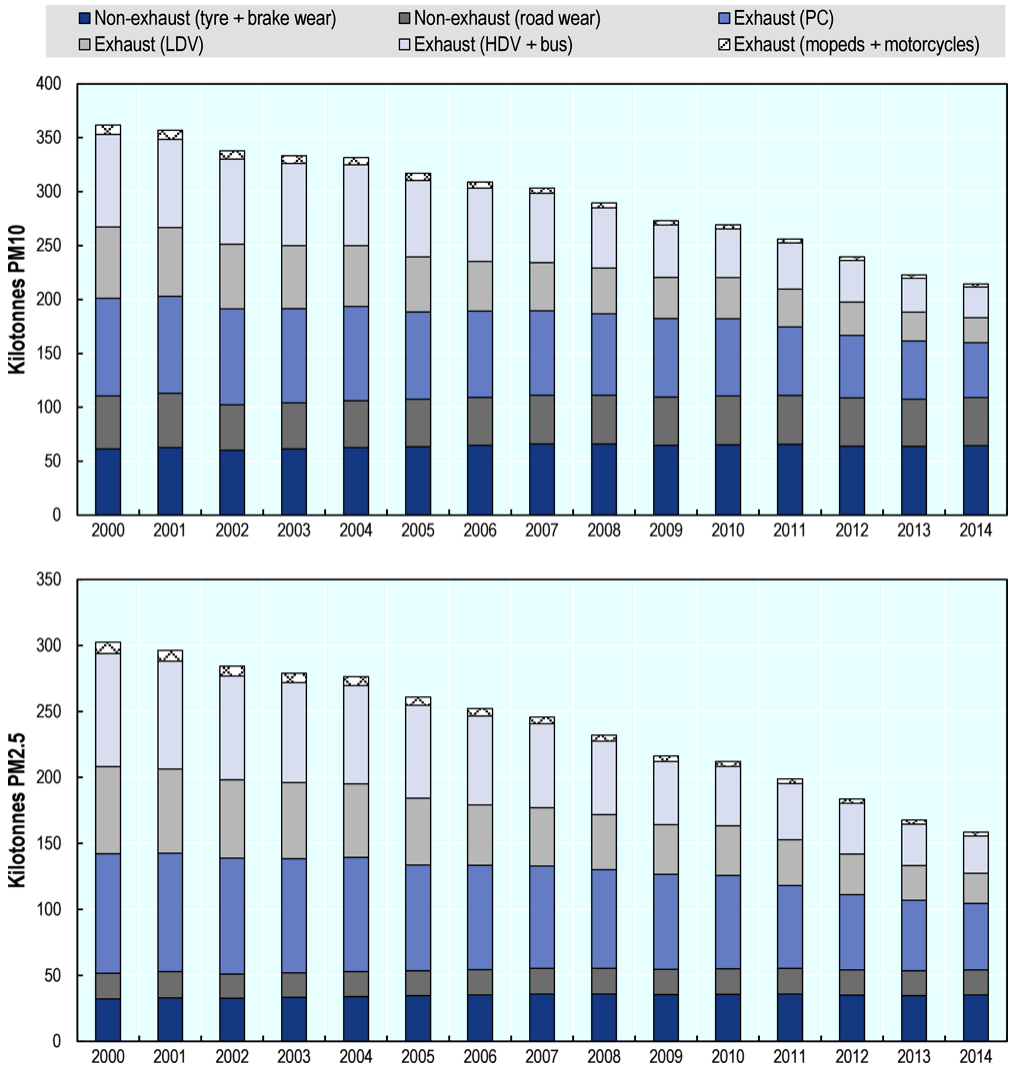

Figure 1.2: Projection of the contribution of non-tailpipe emissions to total traffic emissions in California from 2014 to 2035. Reproduced from OECD (2020).

volatility of organics in the troposphere is the oxidation of VOCs (Trostl et al., 2016; Barsanti et al., 2017; Bianchi et al., 2019; Kroll and Seinfeld, 2008). Since VOCs represent a broad class of compounds, the oxidation of these compounds is extremely complex and requires investigation using different approaches.

Several classes of organics are known to be major contributors to SOA formation in the troposphere. VOCs emitted from anthropogenic sources mainly consist of aliphatic alkanes and aromatic compounds and can contribute significantly to urban SOA (Srivastava et al., 2022). However, the focus of Chapter 3 and 4 of this dissertation is on SOA formation from biogenic VOCs, particu-

larly unsaturated compounds that are very efficiently oxidized in the atmosphere (Calvert et al., 2000). Isoprene is the most abundant biogenic VOC emitted globally (Table 1.1, Sindelarova et al. (2014)). With the chemical formula C_5H_8, isoprene is an unsaturated compound containing 2 double bonds, making it highly susceptible to oxidation. However, as it only contains 5 carbon atoms, the volatility of isoprene oxidation products can remain high under ambient conditions, and thus won't contribute to nucleation and growth of ultrafine particles as efficiently as larger VOCs (Zhao et al., 2013). Monoterpenes ($C_{10}H_{16}$) are higher in molecular weight and are the second most abundant biogenic VOC class by mass, globally. In regions containing large populations of coniferous trees, like boreal forests, monoterpene compounds can dominate VOC emissions.

Within this class of VOCs, many structural isomers exist and have been measured in the ambient atmosphere (Sindelarova et al., 2014; Guenther, 2000). Globally, the most abundant monoterpene is α-pinene, which is a bicyclic alkene compound. The oxidation of a-pinene has been widely studied, and shown to be a significant contributor to ultrafine SOA growth by producing high yields of low-volatility reaction products on atmospherically relevant time scales (Ehn et al., 2014; Zhang et al., 2018; Molteni et al., 2019). However, a range of reactivities has been observed from oxidation of structural isomers of monoterpenes, demonstrating the effect of individual structures on oxidation mechanisms (Lee et al., 2006; Ng et al., 2017; Zhao et al., 2015; Friedman and Farmer, 2018). Understanding these mechanisms are key to assessing the overall impact of monoterpene structure on SOA formation and will lead to more robust representations of these systems in regional and global models. These mechanistic processes are explored in Chapters 3 and 4 of this dissertation for different monoterpenes and different oxidants.

Several oxidant species have been identified as key reaction partners for these processes (Atkinson and Arey, 2003a; Vereecken and Francisco, 2012; Rissanen et al., 2015; Ziemann and Atkinson, 2012), three of which will be discussed in this dissertation. As mentioned previously, OH radical is one such oxidant which is prevalent in the daytime, as its formation is often photo-chemically driven. The OH radical very efficiently oxidizes organics with alkene functionality by attacking the unsaturated carbon atoms in the double bond, forming alkyl radicals that quickly react with atmospheric O_2 to form a peroxy radical group (RO_2). This OH addition reaction can have rate constants as high as cm^3

Table 1.1: Relative contributions of biogenic VOCs to the annual global biogenic VOC distribution estimated using The Model of Emissions of Gases and Aerosols from Nature (MEGANv2.1). Reproduced from Sindelarova et al. (2014).

Global totals Species	mean Tg (species) yr^{-1}	rel. contribution %	minimum Tg yr^{-1}	maximum Tg yr^{-1}
isoprene	594 ± 34	69.2	520	672
sum of monoterpenes	95 ± 3	10.9	89	103
α-pinene	*32 ± 1*	*3.7*	*30*	*34*
β-pinene	*16.7 ± 0.6*	*1.9*	*15.6*	*17.9*
sesquiterpenes	20 ± 1	2.4	18	23
methanol	130 ± 4	6.4	121	138
acetone	37 ± 1	3.0	35	40
ethanol	19 ± 1	1.3	17	21
acetaldehyde	19 ± 1	1.3	17	21
ethene	18.1 ± 0.5	2.0	17.1	19.2
propene	15.0 ± 0.4	1.7	14.1	15.9
formaldehyde	4.6 ± 0.2	0.2	4.3	5.1
formic acid	3.5 ± 0.2	0.1	3.2	3.8
acetic acid	3.5 ± 0.2	0.1	3.2	3.8
2-methyl-3-buten-2-ol	1.6 ± 0.1	0.1	1.4	1.8
toluene	1.5 ± 0.1	0.2	1.4	1.6
other VOC species	8.5 ± 0.3	0.8	7.9	9.0
CO	90 ± 4	–	82	97

s^{-1} for monoterpene systems. OH radical can also oxidize other organic compounds, such as alkanes, ketones and aldehydes, although less quickly than alkene compounds. In addition to OH, ozone (O_3) is an oxidant that is formed secondarily through reaction of NOx (NO_2 + NO) with VOCs. Because of this dependence, ozone concentrations can be high in polluted, urban areas. Ozone also efficiently oxidizes alkene compounds, but by forming a primary ozonide intermediate compound (Johnson and Marston, 2008). This primary ozonide contains a large amount of excess energy, and quickly decomposes into an excited Criegee intermediate. This excited Criegee intermediate can stabilize, or decompose further into vinoxy radical, which can react with O_2 to form an RO_2 group, or undergo additional reactions (Iyer et al., 2021). Although the rate constants for the formation of the primary ozonide from monoterpenes are significantly smaller than the OH attack rate constant, ozone concentrations ($\sim 10^{11}$ cm^{-3} daily average) can be much higher than OH ($\sim 10^6$ cm^{-3} daily average) during the night or in cloudy conditions, when photolysis reactions do not occur (Atkinson and Arey, 2003a). Finally, the role of nitrate radical (NO_3) as an oxidant is less well studied, but has been shown to be a large source of nighttime VOC oxidation (Ng et al., 2017). Nitrate radical is formed from the reaction of NO_2 and ozone, generating NO_3 radical and O_2 as

products. Analogously to the OH radical, the nitrate radical addition to carbon atoms in alkene groups form alkyl radicals which are rapidly oxidized to RO_2 groups in the presence of oxygen. The rate constants for nitrate radical attack ($\sim 10^{-12}$ cm^3 s^{-1}) on monoterpene compounds are slightly slower than the associated OH attack rates ($\sim 10^{-11}$ cm^3 s^{-1}), but faster than ozonolysis rates ($\sim 10^{-17}$ cm^3 s^{-1}) (Ng et al., 2017; Calvert et al., 2000). Additionally, the presence of nitrogen atoms can alter the volatility and reactivity of oxidized organics. If assuming oxidation of the same monoterpene compound, these three oxidation pathways lead to formation of slightly different RO_2 compounds, which has important implications for the autooxidation reactions that follow.

Autooxidation is an important mechanism by which volatile organics can quickly add oxygen atoms, thereby increasing their molecular weight and decreasing volatility thus allowing condensation to occur on atmospheric time scales. Although autooxidation was known to occur for other chemical systems, the feasibility of this mechanism for atmospheric organic gases was only recently suggested by Crounce et al. to provide an explanation for the highly oxidized organics measured in ambient environments, which were unexpected (Crounse et al., 2013). Since then, the relevance of these autooxidation reactions for atmospheric VOC systems been supported by many experimental observations and fundamental calculations (Bianchi et al., 2019; Mentel et al., 2015). Autooxidation is a unimolecular isomerization reaction that occurs when alkyl peroxy radicals (RO_2) can abstract hydrogen atoms from neighboring carbon atoms, creating new alkyl radicals that can react with atmospheric O_2 to form new peroxy radicals. These peroxy radicals can continue to propagate or otherwise terminate through bimolecular interactions. The proximity of the peroxy radical group to hydrogen atom sites and the unique chemical environments surrounding these sites govern the associated energy barriers for these intramolecular hydrogen shifts. Though our understanding of these RO_2 structure activity relationships is rapidly evolving (Otkjær et al., 2018; Xu et al., 2019; Vereecken and Nozière, 2020), the rate constants for these reactions are poorly constrained at present.

In addition to autoxidation, the formation of epoxides from RO_2 compounds is another unimolecular reaction that leads to alkyl radical generation. The structure-activity relationships for these cyclizations have been computationally investigated, and determined to have the fastest rate con-

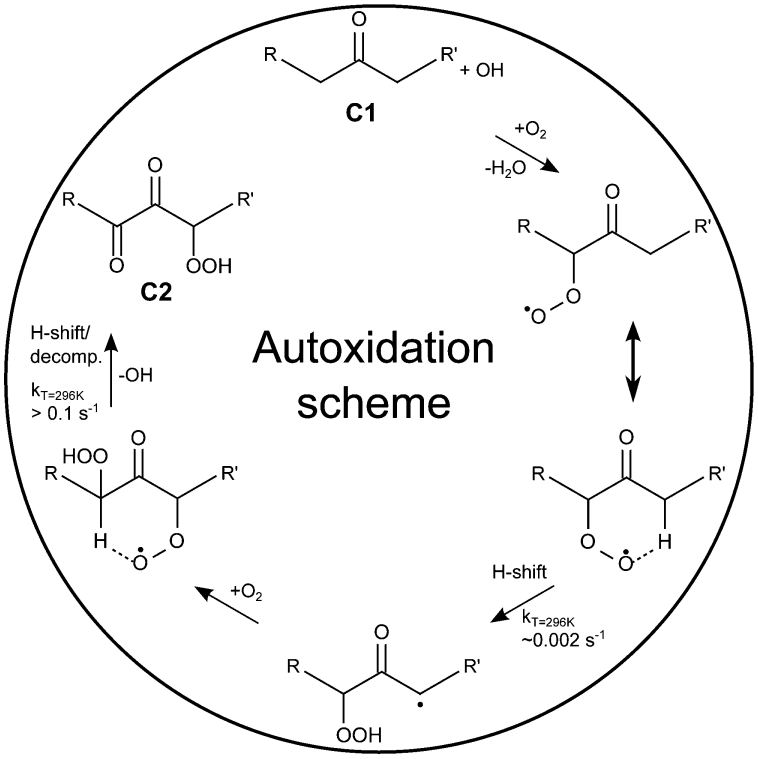

Figure 1.3: Example autoxidation scheme for a ketone oxidized by OH radical. Reproduced from Crounse et al. (2013).

stants when forming 5-7 membered rings for monoterpene compounds and are considered competitive with autoxidation for some systems (Vereecken et al., 2021). Finally, bimolecular reactions of RO_2 compounds can lead to the formation of alkoxy radicals (RO), which can undergo rapid internal hydrogen shifts to form new alkyl radicals, similarly to RO_2 compounds. However, carbon-carbon bond scission pathways leading to fragmentation and other bimolecular reactions leading to radical termination are competitive with isomerization reactions for alkoxy compounds (Vereecken and Peeters, 2012, 2010; Novelli et al., 2021; Zhao et al., 2018).

Vapor pressures of oxidized organics, as related to their volatilities, can be parameterized using various frameworks that rely on molecular formulas as inputs (Pankow and Asher, 2008; Donahue et al., 2012). The cutoff for saturation vapor concentrations of low-volatility organics that are expected to irreversibly partition to the condensed phase is broadly defined here as -0.5 μg m^{-3}. Parameterizations are limited in their ability to accurately predict volatility, but are constantly evolving to account for variable functionalities of organics, which can substantially alter vapor

pressures (Mohr et al., 2019; Schervish and Donahue, 2020). In order to experimentally probe the specific chemical reactions detailed in this section, it is necessary to simulate oxidation in controlled laboratory chamber studies by generating gas precursors and measuring the composition of oxidized products. These approaches are discussed next.

1.3 Measurements

1.3.1 Laboratory chambers for studying organic oxidation chemistry

The use of laboratory chambers, flow tubes and other similar reaction vessels is ubiquitous in the field of aerosol science for probing fundamental processes Chu et al. (2022), including ultrafine particle formation (Dunne et al., 2016). In addition to creating controlled chemical and physical environments that reduce the complexity of systems, the ability to overcome sensitivity limitations for instrumentation is an added benefit of chambers and flow tubes. However, the resulting knowledge gained from chamber studies is often not representative of ambient conditions and can be challenging to incorporate into atmospheric models. For example, high concentrations of reaction precursors lead to specific chemistry, producing reaction products that may provide valuable insight into chemical processes but may not be formed and observed in ambient environments. As the complexity of precursor species increases (mixtures of VOCs, taking into account relative humidity) the difficulty of analysis increases, although ambient conditions are more closely achieved.

Additionally, chambers and other vessels can introduce substantial wall interactions that would not otherwise exist in the atmosphere, making characterization of these interactions important for accurately representing chemical processes (Krechmer et al., 2020). The interactions of organic gases on chamber walls is dependent on the vapor pressure of the organics, with low-volatility species expected to irreversibly partition to walls, while semi-volatile species reach equilibrium partitioning conditions (Ye et al., 2016; Huang et al., 2018; Krechmer et al., 2016). Loss of these condensible

organics to walls can significantly impact observed new particle formation and SOA yield in chamber studies (Matsunaga and ‡, 2010). Additionally, the material of the chamber walls greatly impacts the losses of oxidized organics (Krechmer et al., 2020). Commonly, Teflon is an inert material used in flexible "bag" chambers, or to line rigid chambers. Oxidized organic compounds are expected to reach an equilibrium with Teflon walls and tubing surfaces, making continuous flow operation of chambers desirable to allow wall losses to reach steady conditions. During continuous flow operation, precursor gasses are constantly supplied to the chamber, while removal of gas happens simultaneously. This mode of operation is different from batch mode operation, in which precursors are added only at the beginning of the experiment and allowed to react for a time before measurement occurs. Batch mode operation is advantageous if characterization of a single population of compounds over time is the goal of the study. For the purposes of investigating structural effects on formation of early reaction products and quantifying yield, continuous flow operation was used for the work presented in Chapters 3 and 4 of this dissertation. It is important to note that instead of Teflon walls, our chamber consisted of aluminum and stainless steel walls. Oxidized organics are expected to adsorb to stainless steel, thereby replacing species with weak wall interactions with more strongly interacting species. Only a few reported chambers have metal walls. One such chamber is the CLOUD chamber at CERN in Switzerland (Dunne et al., 2016). This is one of the largest chambers in the world that can simulate new particle formation in ambient concentrations with negligible loss to walls. As our chamber is much smaller (560 L), extensive wall loss characterization has been performed and reported in De Haan et al and Chapter 3 of this dissertation (DeHaan et al., 1999). In addition to wall interactions, other physical aspects of chambers are important to characterize, including mixing time and temperature, as they affect the distribution of reaction products.

To aid representation of all these chamber processes and understand the chemical processes inside reaction chambers, kinetic box modeling can be used (Peng and Jimenez, 2019). In a one dimensional kinetic box model, initial concentrations of reaction precursors and their associated rate constants are defined, and they are allowed to react for a defined period of time. A home-built kinetic box model is detailed in Chapters 3 and 4 and used to determine the concentrations of chemical species that could not be measured with the suite of instruments available, which will be discussed next.

1.3.2 High resolution chemical ionization mass spectrometry

High resolution chemical ionization mass spectrometry (CIMS) is a selective technique for specifically measuring oxidized organics and other gaseous species relevant to nucleation and growth of ultrafine particles. In the past decade, CIMS has become an increasingly popular choice for measuring various atmospheric gas compounds (Aljawhary et al., 2013; Bianchi et al., 2019; Riva et al., 2019b). The chemical selectivity of this technique is dependent on the reagent ion, which reacts with the molecules of interest to form measurable ions. Several reagent ions (acetate, NO_3^-, CF_3O^-, and I^-) are commonly used. For the studies presented in this dissertation, I-CIMS was used to probe oxidized organics and inorganic nitrogen species, while NO_3^- selectively ionized and sulfuric acid and highly oxidized organics.

As permutations of reaction steps are numerous, VOC oxidation can lead to reaction product populations containing many different species with overlapping unit masses in complex mixtures. Analysis of these complex mixtures require high resolution mass spectrometry for adequate peak separation. Additionally, NO_3^- and I^- ions have small and large negative mass defects, respectively, which aid in molecular formula assignment. In negative ion mode, both reagent ions can cluster with molecules of interest upon collision, forming measurable negative ions. CIMS offers soft-ionization, which is advantageous because it minimizes fragmentation during adduct formation, allowing efficient detection of parent ions (Aljawhary et al., 2013).

With NO_3^- CIMS, adduct formation is possible for oxidized organic molecules with a greater binding energy with NO_3^- than nitric acid, thereby transferring the NO_3^- ion from the dimer species to the colliding molecule (Hyttinen et al., 2015). NO_3^- reagent ion efficiently ionizes highly oxygenated molecules (HOMs). Recently, HOMs have been measured in ambient air in the Southeast US using NO_3^- CIMS (Massoli et al., 2018), and many laboratory studies have probed HOM formation from different oxidants with NO_3^- CIMS (Mentel et al., 2015; Ehn et al., 2012, 2014; Draper et al., 2019; Dam et al., 2022; Li et al., 2019; Rissanen et al., 2014; Guo et al., 2022; Isaacman-VanWertz et al., 2018). Generally, two hydrogen bond donors need to be present on the carbon backbone for clustering to occur, but one hydrogen bond donor is sufficient in some cases, where additional

nitrate (-ONO_2) or epoxide functionalization is present (Draper et al., 2019). NO_3^- ion can also efficiently ionize RO_2 radicals (Jokinen et al., 2014; Mentel et al., 2015). In addition to oxidized organics, NO_3^- has been shown to react with sulfuric acid at the collision limit, producing bisulfate (HSO_4^-) as a measurable ion (Kürten et al., 2012). This is attributed to the high acidity of the sulfuric acid molecule. The first ambient measurement of sulfuric acid with NO_3^- CIMS was at the Cheeka Peak Observatory in Washington State in 1993 (Eisele and Tanner, 1993). Since then, these ambient measurements have been made in Southern Finland (Jokinen et al., 2012; Beck et al., 2022) and in aircraft measurements over most of Europe (Zauner-Wieczorek et al., 2022).

I^- CIMS has been used extensively to measure oxidized organics and inorganic nitrogen species in both laboratory studies and in ambient air, especially in the Southeast US (Lee et al., 2014; Mohr et al., 2019; Lopez-Hilfiker et al., 2016b; Lee et al., 2016; Brophy and Farmer, 2015; Kercher et al., 2009; Isaacman-VanWertz et al., 2018). Similarly to NO_3^-, I^- ionizes molecules of interest by forming negative adducts. I^- strongly clusters with inorganic nitrogen species, organic-nitrates, and highly polar molecules with hydrogen bond donor sites (Lee et al., 2016; Bi et al., 2021). The sensitivity of this technique is dependent on the presence of water, as the water cluster can increase sensitivity to oxidized organics by stabilizing adducts, or compete with those organics during adduct formation as humidity increases (Lee et al., 2014). Additionally, steric effects can impact I- adduct formation, as bonding sites need to be accessible to the I^- ion. Therefore, sensitivity calibration for I^- CIMS is non-trivial. However, it has been shown that N_2O_5 forms clusters with I^- at the collision-limit (Lopez-Hilfiker et al., 2016b), so maximum sensitivities can be estimated by the transfer efficiency of the $IN_2O_5^-$ adduct.

$$(HNO_3)_nNO_3 + M \longrightarrow (M)NO_3^- + (HNO_3)n \qquad n=0-2$$

$$(H_2O)_nI + M \longrightarrow (M)I^- + (H_2O)n \qquad n=0-2$$

In addition to forming negative adducts, NO_3^- reagent ion can deprotonate neutral molecules if they are highly acidic, producing M^- ions (Hyttinen et al., 2015). These deprotonation reactions are likely not occurring significantly for I^- CIMS, even though M^- ions are commonly observed (Lopez-Hilfiker et al., 2016b). The ions generated from these alternative processes cannot be confidently assigned as parent ions (not fragments formed during ionization), and the ionization efficiencies and instrument sensitivity to these ions are not easily characterized. Therefore, these compounds are more difficult to quantify and often not considered for analysis.

1.3.3 Additional measurements

Although CIMS provided us with rich chemical composition information, other measurements were necessary to gain a more comprehensive understanding of the chemistry contributing to new particle formation inside our chambers. These included measurements of VOCs (GC-FID), oxidant species (O_3, NOx), CO, particle size distributions (SMPS) and particle composition (HPLC-HRMS) (Finlayson-Pitts and Pitts, 2000; Nizkorodov et al., 2011). Monoterpene compounds were measured in Chapters 3 and 4 using a gas chromatography (GC) system with a flame ionization detector (FID) and a custom-built inlet specially designed to trap monoterpenes on a cold Tenax substrate and thermally desorb them into the GC column. Oxidants and particles size distributions were measured in all of the studied discussed in this dissertation. Ozone and NOx were optically measured with a combination of commercial analyzers from 2B Technologies (Model 106-L, Model 405 nm) and Thermofisher (Thermo 42C NO-NO2-NOx). Particle size distributions were measured with standard SMPS systems that neutralized the charge distribution of incoming particles with alpha radiation from ^{210}Po radioactive sources before separating them in differential mobility analyzers (DMA, TSI Model 3081) by their electrical mobility and optically counting them after growth by supersaturation and condensation of a working fluid (butanol or water, for our systems) onto the particles. Condensation particle counters (CPCs) included a Brechtel Mixing CPC (model 1720), several CPCs manufactured by TSI (3020, 3025A) and a water CPC (Aerosol Devices, MAGIC). In Chapter 2, offline high performance liquid chromatography-high resolution mass spectrometry (HPLC-HRMS) was used to assess composition of secondary organic aerosol particles and specif-

ically investigate the presence of structural isomers by obtaining MS-MS fragmentation spectra. The implemented methods pertaining to this technique are discussed in detail in the experimental section of Chapter 2.

1.4 Dissertation Goals and Chapter Descriptions

This dissertation has multiple goals relating to understanding sources and processes forming important precursor gases for new particle formation and growth in the atmosphere. The questions being asked in this dissertation are detailed below, with their corresponding chapters shown:

Goals:

1. What precursor gases are emitted from brake-wear processes? [Chapter 2]
2. How does monoterpene structure impact formation of low-volatility organics from oxidation? [Chapters 3 and 4]
3. How accurately can we represent gas-to-particle closure with vapor pressure-driven condensation? [Chapter 4]

In Chapter 2, we measured several important precursor gases for ultrafine particle formation and growth from vehicular brake wear using both NO_3^- CIMS and I^- CIMS. Gases, ultrafine particles and coarse-mode particles were generated with a brake dynamometer system that simulated moderate and heavy braking conditions. Two common formulations of brake pads were tested (ceramic and semi-metallic), as composition of brake pads can vary widely. Additionally, emissions were measured from new, gently worn and heavily worn brake pads, as emissions profiles are affected by the degree of wear on the brake pads. The dependence of emissions on the temperature of the rotor was investigated as the rotor was heated by friction. The formation of ultrafine particles was observed for ceramic brake pads at lower temperatures (100-140 °C) for the ceramic brake than the semi-metallic brake (140-200 °C) and shifted to higher temperatures with increased wear. High concentrations of sulfur trioxide and sulfuric acid were formed at high temperatures and corresponded with formation

of ultrafine particles. The formation of inorganic nitrogen compounds, reservoirs for oxidants and NOx, corresponded with both NOx and CO formation. The starting temperature for CO formation was consistent for all brake formulations and wear, consistent with combustion-driven emission, but NOx formation was variable. Organic emissions were dominated by formic acid, though over 60 oxidized organic compounds were measured with I-CIMS.

Chapter 3 is a laboratory chamber investigation on mechanistic effects of monoterpene structure during nitrate-radical induced oxidation. Four monoterpenes (α-pinene, β-pinene, Δ-3-carene, α-thujene) were oxidized with nitrate-radical at high monoterpene-to-nitrate radical ratios (40:1). Under those conditions, new particle formation was observed for the β-pinene and Δ-3-carene systems, but not for the α-pinene and α-thujene systems, despite relatively abundant formation of highly oxidized reaction products for the α-thujene system. Relative yields of low-volatility species, organonitrate compounds and SOA between the four systems trended together in the following order: Δ-3-carene $>\beta$-pinene $>\alpha$-thujene $>\alpha$-pinene). As all first generation alkoxy products have structural differences, the Δ-3-carene and β-pinene products have competitively carbon-carbon scission pathways which will not terminate the radical sites. The initial α-thujene alkyl radical species was predicted to have a rapid internal radical rearrangement pathway, breaking the unstable three-membered ring and regenerating an alkyl radical, but this is not confirmed. The formation of HOM but lack of observed nucleation for the α-thujene system suggests complex gas to particle conversion processes, which require further elucidation.

In Chapter 4, these gas-particle conversion processes for oxidized organics were studied in detail for one monoterpene oxidation system, the ozonolysis of α-thujene. The same chamber system was used for this study as in Chapter 3. We predicted that ozonolysis of α-thujene may efficiently produce highly oxidized products and SOA through a similar rapid alkyl radical rearrangement mentioned in Chapter 3, which relies on the decomposition of the strained three-membered ring. The formation of oxidized reaction products and SOA from different chemical regimes were probed by varying the monoterpene-to-ozone ratio and measured with NO_3^- and I^- CIMS. Observed yield of low-volatility reaction products were comparable to other monoterpene ozonolysis systems (1-5%), but the α-thujene system produced lower SOA yields (2-4%) compared to those measured from

α-pinene ozonolysis (10-20%) at the same mass loading values. Additionally, measured growth rates (on the order of nm min^{-1}) were under-predicted using a simple condensational growth model, for all experimental conditions. This is consistent with the formation of a large fraction of semi-volatile fragment compounds, which are not considered in the model. These fragmentation pathways seem to compete with autoxidation pathways, resulting in product distributions with increased volatility.

Chapter 5 consists of concluding remarks on all the work presented in this dissertation and future directions for studying ultrafine particle formation.

Chapter 2

Brake-wear emissions of sulfuric acid, sulfur trioxide, inorganic nitrogen species and organic acids

2.1 Abstract

Ultrafine aerosol particles generated from brake-wear currently lack characterization, and the formation processes of these ultrafine particles have not been investigated. In this study, ultrafine particles were generated from a disc brake using a brake dynamometer. Important precursor gases for ultrafine particle formation and growth were measured using chemical ionization mass spectrometry. Measured compounds included sulfuric acid, sulfur trioxide, inorganic nitrogen compounds (HONO, $ClNO_2$, N_2O_5) and organic acids. The emission of these compounds from brake-wear has not been previously reported. Generally, these species formed at high temperatures preceding ultrafine particle formation, although some exceptions were observed. The formation of inorganic nitrogen compounds corresponded with both NOx and CO, suggesting different secondary processes contributing to their production. As commercial brake-pad formulations vary greatly, emissions from

two common formulations (ceramic, semi-metallic) were assessed. Additionally, observed emission profiles from brake-pads changed with increasing wear and are reported for a range of wear.

2.2 Introduction

Investigations of brake-wear as a source of particulate matter from motor vehicles is an emerging area of study. This source of non-tailpipe emissions is relevant for all types of vehicles, but is projected to become a major emission source in the near future, after electrification of the vehicle fleet. While brake-wear emissions of coarse-mode particles have gained significant attention in recent studies (Alves et al., 2021; Hagino et al., 2016; Fussell et al., 2022; Piscitello et al., 2021; OECD, 2020), braking processes have also been shown to produce ultrafine particles (sub-100 nm in diameter), which are not currently well characterized.

Because of their size, ultrafine particles have unique properties that impact climate and human health. Ultrafine particles comprise a large fraction of total particle number concentration globally and contribute substantially to cloud formation when they grow beyond ∼100 nm in diameter (Kulmala et al., 2014). Additionally, ultrafine particles substantially impact human health by depositing deeply in the lung and traversing the blood-brain barrier, leading to inflammation and respiratory disease (Gauderman et al., 2005; Malachova et al., 2016; Schraufnagel, 2020). Because of these impacts, studying ultrafine particle formation from brake–wear is especially important from an environmental justice perspective, as traffic pollution has been shown to disproportionately affect socioeconomically disadvantaged communities, which are often located near highways and other transportation infrastructure (Tessum et al., 2021).

The formation of these ultrafine particles from vehicular braking processes has been demonstrated in laboratory studies which simulated braking (Nosko et al., 2017; Nosko and Olofsson, 2017; Park et al., 2021; Namgung et al., 2016), and ultrafine particles have been measured in field studies near roadways (zum Hagen et al., 2019; Lv et al., 2020). However, it is currently unclear whether ultrafine particles produced from brakes are primarily emitted or secondarily formed from co-emitted reactive

gases. Air masses from roadways are well-mixed, making source apportionment and elucidation of particle formation processes challenging. Thus, controlled laboratory studies are necessary to isolate these processes, which are relatively unexplored at present. Fundamental understanding of the sources and mechanisms of brake-wear emissions will allow regulatory agencies to more effectively produce controls for traffic emissions.

In previous studies, emission of ultrafine particles has been observed from dynamometer and pin-on-disc braking apparatuses at temperatures exceeding ∼160 °C) as frictional force heats the brake surfaces (Nosko et al., 2017; Nosko and Olofsson, 2017; Park et al., 2021; Namgung et al., 2016). At these high temperatures, the emission of volatile gases has also been observed (Plachá et al., 2017). Although commercial brake formulations are often proprietary, brake pads are known to contain a broad range of compounds, including metal oxides, phenolic resins, fillers (Bofanti, 2016). Therefore, a variety of species from a diverse chemical element pool would likely be emitted during frictional heating, including those which are known precursor gases for nucleation and growth of ultrafine particles (i.e., low-volatility organics and strong acids and bases) (Ehn et al., 2014; Kulmala et al., 2014).

To observe if, in fact, these precursor vapors are formed from braking processes, we generated brake emissions with a home-built dynamometer system. We tested two common formulations of brake pads (ceramic and semi-metallic), under two different types of braking conditions (moderate and heavy). To selectively measure compounds of interest from the brake emissions, we used chemical ionization mass spectrometry (CIMS) with two reagent ions. This combination allowed us to probe formation of sulfuric acid (H_2SO_4), sulfur trioxide (SO_3), oxidized organics and various inorganic nitrogen species (HONO, $ClNO_2$, N_2O_5), which are known reservoirs of important atmospheric oxidants (OH radical) and NOx (NO_2 + NO) (Aljawhary et al., 2013; Finlayson-Pitts and Pitts, 2000). Both sulfuric acid and low-volatility organics are formed from secondary oxidation processes in the atmosphere, therefore, predicting the formation of these gases is complex and dependent on quantification of source emissions of many different compounds that may participate in tropospheric NOx, ozone (O_3) and OH cycles.

Atmospheric H_2SO_4 is formed from oxidation of SO_2 to SO_3, and conversion of SO_3 to H_2SO_4 (Finlayson-Pitts and Pitts, 2000). Currently, sources of urban inorganic sulfate are attributed primarily to industrial combustion of fossil fuels. OH radical is considered the major daytime oxidant for SO_2 (Crutzen and Zimmermann, 1991), measurements of high concentrations of sulfuric acid at night allude to either nighttime sources of OH or the presence of alternate oxidants, both of which are ongoing research topics. The inorganic nitrogen compounds, $ClNO_2$ and HONO, are nighttime oxidant reservoirs that photolyze during the day. HONO undergoes photolysis at wavelengths between 300 nm to 400 nm, releasing NO and OH radicals, which oxidize volatile organics very efficiently (Alicke, 2003). Therefore, the presence of HONO will affect formation of both sulfuric acid and HOMs.

Heterogeneous uptake of N_2O_5 onto chloride-containing aerosol particles can produce gaseous $ClNO_2$ (Riedel et al., 2013), which is a major source of a highly reactive atmospheric oxidant, Cl radical (Wang et al., 2019). Atmospheric N_2O_5 is formed from oxidation of NO_2 with O_3, producing nitrate radical and O_2 (Atkinson et al., 1986). Nitrate radical reacts with NO_2, forming N_2O_5 under equilibrium conditions. Photolysis of $ClNO_2$ releases Cl radical and NO_2 gas in the atmosphere. Cl radicals can participate in many tropospheric reactions, some of which affect the production of oxidized organics, ozone (O_3) and OH radical (Wang et al., 2019; Finlayson-Pitts and Pitts, 2000). In the past, the presence of $ClNO_2$ in urban areas has been attributed to air masses transported from marine sources, with smaller emissions from combustion in power plants (Riedel et al., 2013), but robust investigations of urban $ClNO_2$ emission sources still need to be elucidated. To date, no prior work has reported the presence of the numerous, important precursor species discussed in this manuscript from brake-wear emissions.

2.3 Methods

2.3.1 Brake Dynamometer System

Figure 2.1 shows the home-built brake dynamometer used in these experiments. It is comprised of a disc brake system consisting of a pneumatically-actuated brake caliper (Kodiak model 225) pressing either ceramic (Kodiak model DBC-225) or semi-metallic (BrakeBest model MKD289) brake pads against a G3000 rotor (BrakeBest model 96211RGS). The rotor is rotated at a constant rotational speed using a large metal-working lathe (Lodge and Shipley). Braking force was applied using an electric over hydraulic brake actuator (Hydrastar model HBA-12) and a brake controller (Tekonsha model PowerTrac), the latter of which was modified to allow computer control of pneumatic pressure and braking time. The rotor and caliper fitted with brake pads were enclosed in an 87 L anodized aluminum chamber with clean air (30 lpm) from a purge gas generator (Parker-Balston; model 75-62) constantly flowing into the box to maintain a positive pressure. Sensors included a relative humidity (RH) and temperature sensor (Vaisala, HMP-44), an infrared non-contact temperature sensor for measuring the temperature the rotor surface (Omega model OS301-HT), a pressure sensor for monitoring the brake system pneumatic fluid pressure (AiM, MC-327), and a torque sensor for monitoring the torque applied to the brake caliper (Ato model ATO-TQS-S01). Synthetic DOT 3 brake fluid (O'Reilly model 72120) was used to actuate brake.

For these experiments, the independent variables that span the braking operation space are the rotor rotational speed and brake fluid pneumatic pressure. State variables of note are braking torque and the surface temperature of the brake rotor, the latter of which has been found to strongly influence the production of gases and ultrafine particles during heavy braking (Piscitello et al., 2021; Kuk). Braking was simulated by rotating the rotor at constant speed and applying step-function patterns of braking pneumatic pressure to the caliper. This brake testing methodology, proposed by Neimann et al. (Niemann et al., 2018), allows one to achieve characteristic operating points in a consistent manner that can be successfully reproduced over time. The severity (moderate or heavy) of braking was determined by the intensity and duty cycle of the applied brake fluid pressure cycle. Moderate

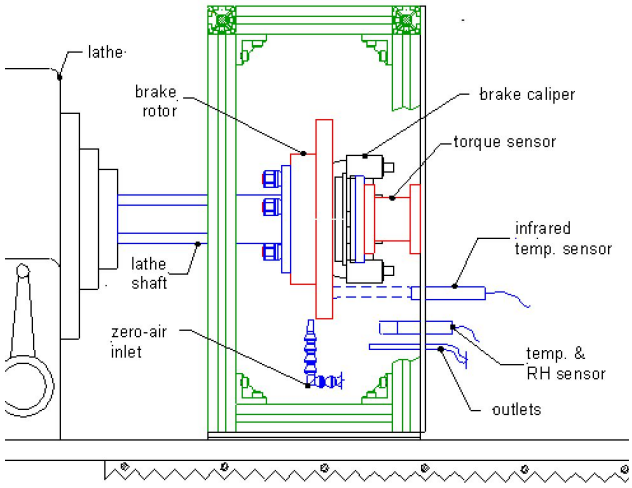

Figure 2.1: Schematic of brake test dynamometer used in these experiments.

braking was achieved with a pneumatic pressure of ∼160 kPa applied for 8 s followed by an idle time of 45 s. Heavy braking, characterized by a dramatic increase in emissions of gases and ultrafine particles, was achieved with a pneumatic pressure of ∼200 kPa applied for 10 s followed by a idle time of 30 s.

Figure 2.2 shows a typical testing sequence. (1) The chamber is first flushed with clean air to characterize any background contaminants. (2) The rotor is spun at 173 revolutions min^{-1} to characterize emissions from drag braking (zero pneumatic pressure). The measured braking torque during this spinning phase ranged from 4-6 N·m and the rotor temperature remained at ambient laboratory temperature. (3) Next, we applied the sequence corresponding to moderate braking. Maximum torque and brake rotor temperature achieved during moderate braking were 120 N·m and 100 °C, respectively. This period persisted until measured state variables achieved steady state. (4) The final step was the application of the heavy braking sequence. Maximum torque and brake rotor temperature achieved during heavy braking were 250 N·m and 200 °C, respectively. Figure 2.2 shows one important characteristic of heavy braking, in which the buildup of heat in the braking surfaces causes a reduction in applied torque commonly referred to as ”brake fade.”

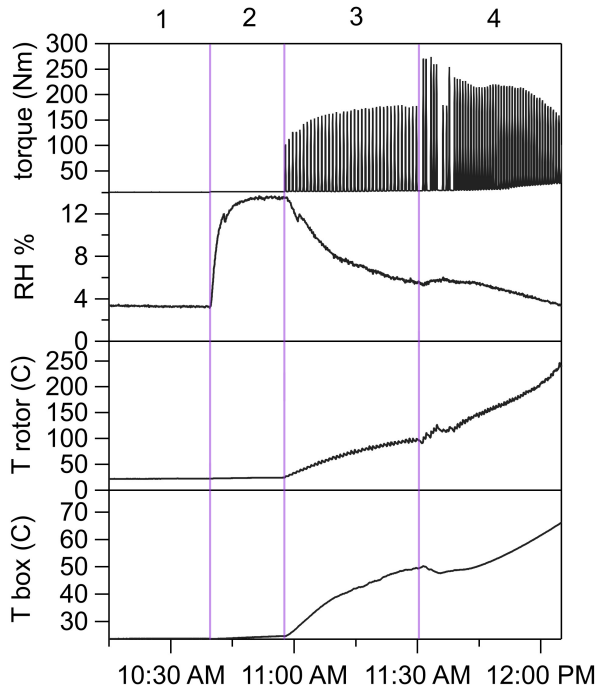

Figure 2.2: Chamber temperature (T box), rotor temperature (T rotor), relative humidity inside the chamber and torque on the brake pad are plotted against time to show an example of an experiment sequence. The numbers above the plot denote the steps in the sequence detailed in the text above.

2.3.2 Gas and Particle Measurements

All instruments recording gas and particle emissions were connected along a single axis across the bottom section of the chamber front panel as seen in Figure 2.1. Sampling lines were $\frac{1}{4}$ inch stainless steel or copper tubing and penetrated ∼5 cm into the chamber. Particle size distributions were measured with a scanning mobility particle sizer (SMPS, TSI long DMA model 3081, Brechtel Mixing CPC model 1720) for sub 400-nm particles, and an aerodynamic particle sizer (APS, TSI model 3321) for particles with diameters between 500-10000 nm (0.5 to 10 micron). The mixing ratios of NOx and CO were measured with optical analyzers (Thermo 42C NO-NO2-NOx, Thermo 48i CO analyzer).

A high resolution time of flight chemical ionization mass spectrometer was used to measure gas composition. This instrument was equipped with a home-built transverse ionization inlet described

in Li et al (Li et al., 2019). NO_3^- reagent ions were introduced to the inlet by flowing ultrapure N_2 over liquid nitric acid (HNO_3). I^- reagent ions were generated by flowing ultrapure N_2 over Teflon permeation cells containing methyl iodide (ICH_3). The sensitivity response of our NO_3^- CIMS to H_2SO_4 was directly calibrated by producing known concentrations of gaseous H_2SO_4, following the procedure described by Kurten et al. (Kürten et al., 2012). For I^- CIMS, the collision-limit sensitivity was characterized by generating gaseous N_2O_5 through reaction of ozone with NO_2 (Lopez-Hilfiker et al., 2016b; Kercher et al., 2009). This sensitivity is assumed for all measured species, thus representing an upper limit for the concentration for all compounds measured with I^- CIMS (Ehn et al., 2014; Mohr et al., 2019). High resolution mass spectra were processed using Tofware postprocessing software written implemented in the Igor Pro programming environment (version 2.5.13, Aerodyne Research Inc.). Calibration of the m/z axis was performed using known reagent ion peaks as well as those of their associated oligomers.

2.4 Results

It is important to note that the amount of physical wear on brake pads can greatly change their emission profiles. In most reported laboratory studies of brake emissions, brake pads are subjected to a bedding, or breaking-in, process before emissions are measured. This process varies widely between studies, from gentler processes (grating or running cycles) to harsher ones (machining down the brake pads) (Alves et al., 2021; Nosko et al., 2017; Park et al., 2021; Mathissen et al., 2018). Additionally, brake pads can reach very high temperatures during heavy braking, which can potentially alter the chemical composition and physical properties of the surface material through annealing or pyrolysis (Borawski, 2022). For this reason, we chose to study brake-wear emissions over the lifetime of brake pads: new, gently worn, and heavily worn. Particle size distributions and gas species of interest are plotted against rotor temperature in Figure 2.3 for both ceramic and semi-metallic formulations, and all degrees of wear (new, gently worn and heavily worn). New brake pads were tested straight out of the box. After going through one testing cycle, the brake pad is considered "gently worn." After roughly 20 uses, the brake pad is considered "heavily worn."

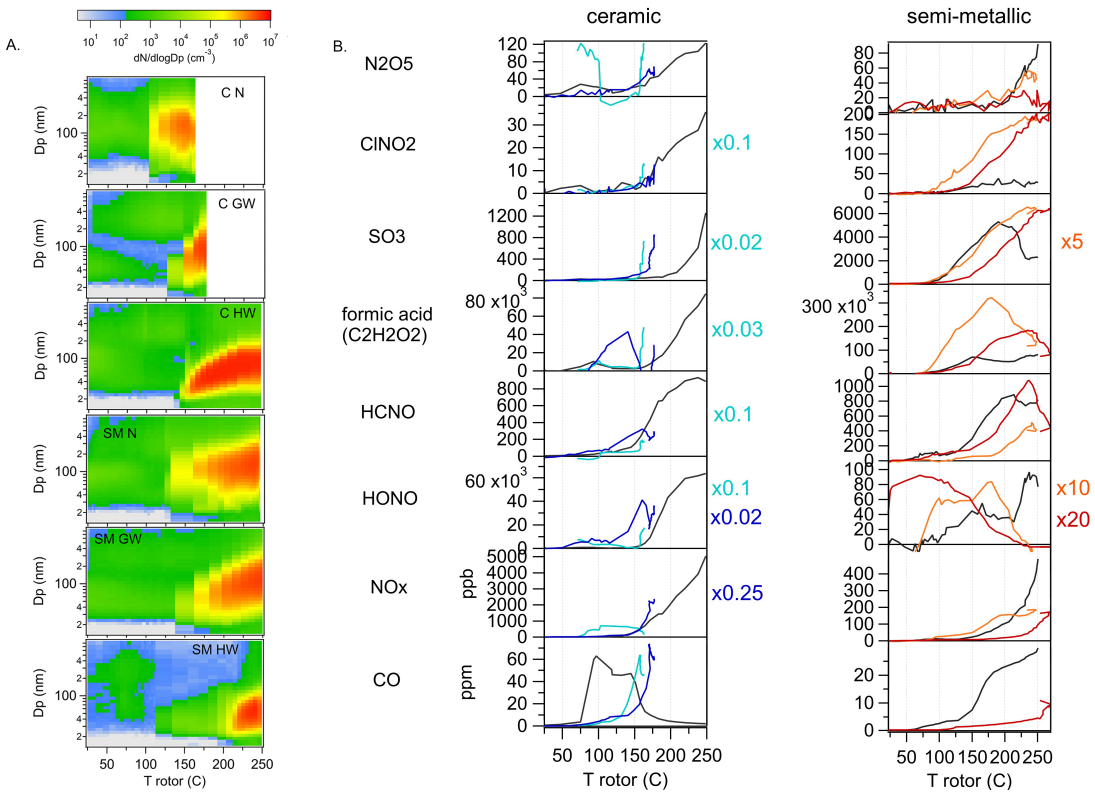

Figure 2.3: A. Size distributions measured with SMPS for each experiment plotted against rotor temperature for ceramic (C) and semi-metallic (SM) brake pads. Also plotted are degrees of wear: new (N), gently worn (GW) and heavily worn (HW). B. Measured gaseous species plotted against rotor temperature for ceramic and semi-metallic brake pads. Light traces are from new brakes, medium traces are from gently worn brakes and dark traces are from heavily worn brakes. All traces are scaled by the concentrations measured for the heavily worn brakes (left axis). N_2O_5, $ClNO_2$, SO_3, formic acid, HNCO, and HONO were measured with I^- CIMS, normalized by dividing the signal intensity by the reagent intensity and converted to mixing ratio (ppt per 10 s) by multiplying by the collision-limit calibration factor as described in the text. NOx and CO were measured with optical analyzers.

2.4.1 Ultrafine Particle Formation

We observed particle production from spinning, light braking and heavy braking for both brake pad types (Figure 2.3A). An ultrafine mode was observed during the spinning phase, which reproduces frictional drag processes. This mode did not grow in size, and is therefore attributed to a combination of re-entrainment of particles deposited on the brake surface or chamber walls and primary emissions from the brake pads. The emission of large diameter particles (0.7 to 8 micron) was measured during

moderate and heavy braking phases with an APS. Observed concentrations these particles were on the order of 10^3 cm^{-3}.

Formation of high concentrations of ultrafine particles was observed at rotor surface temperatures starting at ∼160 °C) in the same range reported for previous laboratory studies of brake-wear (Nosko et al., 2017; Nosko and Olofsson, 2017; Mathissen et al., 2018; zum Hagen et al., 2019). The critical temperature for ultrafine particle formation was, in general, lower for the ceramic brake (100-140 °C) than the semi-metallic brake. This observation is consistent with the ceramic brake formulation containing a higher fraction of organics than the semi-metallic brake formulation. Additionally, this critical temperature increased as brake pads became worn for both formulations, indicating physical and/or chemical changes on the brake pad surfaces (Borawski, 2022). These changes may be induced by the braking process through thermal processes, or by wearing down the brake pads and exposing new layers of material.

2.4.2 Formation of Sulfur Trioxide and Sulfuric Acid

SO_3 is formed at high temperatures during heavy braking, coinciding with ultrafine particle formation. For the ceramic brake pad, the temperature at which SO_3 emission started increased as the brake pad became more worn (75 °C for brand new, 100 °C for slightly worn and 150 °C for heavily worn). For the semi-metallic brake pad, such a trend was not observed, but SO_3 was generated during moderate braking conditions for several experiments. This may be due to the fact that, for semi-metallic brake pads, moderate braking conditions can produce the same rotor temperatures as those produced under heavy braking for the ceramic brake pads. Generally, the semi-metallic brake pads emitted much more SO_3 than the ceramic brake pads. The maximum concentration of SO_3 measured for the ceramic brake pads increased as the pads became worn (0.1 to 1.2 ppb), but the opposite was observed for the semi-metallic brake pads (30 ppb to 8 ppb). It is possible that SO_2 reacted with OH to form SO_3, which is a reaction commonly considered for atmospheric SO_2. Preliminary measurements of reactive oxygen species in particles generated from brake wear, performed by the Shiraiwa Lab during these experiments, have found the presence of OH radical

(Shiraiwa, M., personal communication). A recent study, which reported measurements of high concentrations of SO_3 near roadways, suggested that SO_2 can react with epoxide compounds on soot particle surfaces to form SO_3 (Yao et al., 2020). Additionally, SO_3 can also be formed from SO_2 reactions with stabilized Criegee Intermediates (sCI). Although the formation of oxidized organics was observed, measurements of ozone would be necessary to help inform the likelihood of the sCI pathway.

Sulfuric acid is formed at high temperatures during heavy braking, coinciding with both SO_3 and ultrafine particle formation. With NO_3^- CIMS, the bisulfate ion (HSO_4^-) is measured as a proxy for sulfuric acid (Kurtén et al., 2016). The maximum concentration inside the chamber is 1 x 10^6 cm^{-3} for the ceramic brake pad and 25 x 10^6 cm^{-3} for the semi-metallic brake pad. Only measurements of worn brake pads were available for sulfuric acid measurements, and thus are plotted separately from species measured with I^- CIMS (Figure 2.4. It's possible that SO_3 is being converted to H_2SO_4. The higher concentration of H_2SO_4 measured for the semi-metallic brake compared to the ceramic brake is consistent with measured SO_3 concentrations. Atmospheric conversion of SO_3 to H_2SO_4 is possible through reactions with water or organic acids. However, during heavy braking conditions, the relative humidity inside the chamber decreased from about 10% to 4%. This decrease is also reflected by the decrease in the IH_2O^- adduct signal measured by CIMS. Conversely, formic acid increased dramatically during heavy braking and was measured at high concentrations (1.6 to 300 ppb). Therefore, it is likely that organic acid-driven oxidation is playing a large role in converting SO_3 to H_2SO_4 under these experimental conditions.

The extent to which sulfuric acid is contributing to the observed ultrafine particle mode needs further investigation. Sulfuric acid can condense onto particles at diameters approaching 100 nm because its volatility is sufficiently low, but low-volatility organics may contribute more to growth in this size range if concentrations of organics are higher (Ehn et al., 2014). However, the impact of sulfuric acid is greater for cluster formation and nucleation because it reacts with atmospheric base compounds, such as amines, and with water to form stable clusters (Xie et al., 2017). Future measurements assessing the presence of gas-phase bases are necessary to predict the potential for acid-base driven nucleation from our braking system. Additionally, chemical composition measurements of ultrafine

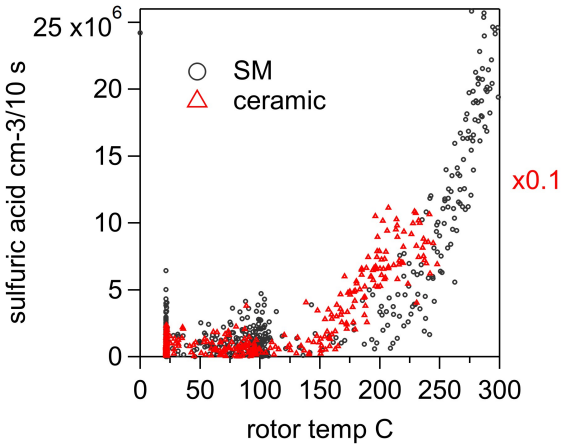

Figure 2.4: Concentration of sulfuric acid measured with NO_3^- CIMS for heavily worn ceramic and semi-metallic brake pads, plotted against rotor temperature (C). Sulfuric acid concentration from ceramic brake pads was scaled according to the concentration measured from the semi-metallic brake pads (left axis).

particles are important for confirming the presence of sulfate, especially for particles of smaller diameters. These measurements were made by the Finlayson-Pitts group and the Smith group using proton transfer reaction-mass spectrometery (PTR-MS) and thermal desorption chemical ionization mass spectrometery (TDCIMS) during these experiments, but are currently in the process of analysis and will be considered for future work (Perraud, V., Thomas, A.E., personal communications).

2.4.3 Formation of NOx and Carbon Monoxide

The formation of NOx was observed at 110-120 °C during heavy braking conditions for both brake pad types of gently worn and heavily worn condition. For new ceramic and semi-metallic brake pads, NOx was emitted during moderate braking conditions at low temperatures (75 °C). Generally, 4-10 times more NOx was emitted by the ceramic brake pad (0.6 to 5 ppm) than the semi-metallic brake pad (0.15 to 0.4 ppm), and heavily worn pads emitted more NOx than new pads.

The production of CO was also observed, with formation starting at around 75 °C during moderate braking conditions for all brake types and all degrees of wear. The formation of CO is considered an indicator of smoldering or combustion-like processes, and is supported by the observation of CO

formation at the same temperature for each brake pad type. For the ceramic pads, the maximum concentration of CO (60 ppm) did not change between new and worn condition, but the temperature at which this maximum was reached decreased with wear (90 °C for the heavily worn pads vs. 150-160 °C for the new and slightly worn pads). For the semi-metallic brake pads, the maximum concentrations of CO increased with increasing wear (10 to 30 ppm), and were overall less than the ceramic pads.

2.4.4 Formation of Inorganic Nitrogen Species

The formation of HONO corresponded with the formation of both NOx and CO for different experiments. For the new ceramic brake pads, HONO production increased as NOx decreased and CO increased, but for the heavily worn ceramic pads, the opposite relationship was observed. For the gently used ceramic pads, HONO production increased with both NOx and CO. For the semi-metallic pads, HONO production was increased with NOx and CO for the new and heavily worn pads, but decreased with increasing NOx and CO for the gently worn pads. The variability of correlation between HONO, NOx and CO emissions implicates the simultaneous production of HONO from different chemical processes within our system. In the atmosphere, HONO can be formed from several reactions that depend on NOx. The reaction of gaseous OH and NO radicals are a dominant source of daytime HONO, while heterogeneous reaction of NO_2 on surfaces in the presence of water is an additional pathway for secondary HONO formation (Song et al., 2023). Primary emissions of HONO have been attributed to combustion engines and biomass burning sources that produce CO (Nie et al., 2015; Liao et al., 2021; Nakashima and Kondo, 2022; Finlayson-Pitts and Pitts, 2000). In our system, it is possible for all of these processes to occur, although the presence of water is greatly reduced during heavy braking conditions. Quantification of HONO production from specific pathways would require additional experimental investigations, which are planned for future studies. Maximum HONO mixing ratios were higher for the ceramic brake pads (0.8 to 60 ppb) than the semi-metallic (0.08 to 0.8 ppb), with heavily worn pads producing the most HONO for both brake pad types.

Additional observed inorganic nitrogen species include nitryl chloride ($ClNO_2$) and dinitrogen pentoxide (N_2O_5), which are both reservoirs for NOx and therefore constituents of the NOx cycle. It is not surprising that the formation of these species corresponds mainly with NOx, except in the case of the new ceramic brake pads. During that experiment, NOx was lost more quickly than it was produced, while every other measured species was produced more quickly than lost. The maximum ratios of $ClNO_2$ were overall higher for the semi-metallic brake pads (30 to 200 ppt) than the ceramic pads (1.5 to 35 ppt). However, both NOx and N_2O_5 mixing ratios were higher for the ceramic pads (1 to 120 ppt) than the semi-metallic (50 to 90 ppt). This indicates a more efficient conversion from NOx to $ClNO_2$ for the semi-metallic pads, implying a higher concentration of condensed-phase chlorine in the aerosol produced from these pads. Future measurements of particle composition are necessary for confirmation.

2.4.5 Formation of Organic Acids

Isocyanic acid (HNCO) is another compound that was observed to form with both NOx and CO. In recent studies, HNCO has been measured in ambient air near roadways (Leslie et al., 2019). Like HONO, HNCO formation is similarly attributed to combustion sources. Photochemical production of HNCO from amines and amides is an additional formation pathway, but is not relevant to our study, given the dark conditions insdie the chamber. HNCO is known to exhibit toxicity in humans and is, therefore, an important species to identify. The maximum HNCO mixing ratios measured were 0.5 to 1 ppb for the semi-metallic brake pads and 0.02 to 0.9 ppb for the ceramic pads. HNCO mixing ratios of up to 10s of ppb have been measured in various environments.

The molecular formulas of over 60 oxidized organic compounds were identified with I^- CIMS, as I-adducts. The dominant species measured for both brake types is formic acid (CH_2O_2), which is an order of magnitude more intense than any of the next most abundant compounds. These second most abundant compound has the formula $C_7H_6O_2$ (semi-metallic) and C_7H_5NO (ceramic) and are likely aromatic substituted benzene compounds. After these compounds, the majority of other measured compounds are at least two orders of magnitude less intense than formic acid. Globally, formic acid is

one of the most abundant atmospheric organic acids (Millet et al., 2015). The observed distribution of organics is influenced by the selectivity of the I- reagent ion, which is known to be highly sensitive to formic acid and nitrogen-containing organics (Lee et al., 2014; Lopez-Hilfiker et al., 2016b). More formic acid was produced by the semi-metallic brake pads (190 and 300 ppb) than the ceramic pads (1.6 and 4 ppb) for the new and gently worn pads, but a similar amount of formic acid (80 ppb) was measured for both formulations of heavily worn pads. The formation of formic acid started at low temperatures (75 to 80 °C) during moderate braking conditions in most cases, and was enhanced when brake pressure was increased to represent heavy braking conditions. The observed ratio of production over loss of formic acid changed during moderate braking conditions, resulting in the slope of the measured ion signal becoming less steep. This change in slope is attributed to an increase in formic acid loss which can be driven by thermal or condensational loss. These shifts do not occur at the same temperature for every system, indicating that condensational loss may be significant. The time correspondence of formic acid loss with formation of ultrafine particles is another supporting observation for condensation-driven loss.

2.4.6 Discussion

Our measurements of emissions from simulated braking processes have limitations that prevent direct comparison of emissions to ambient observations. Although the dynamometer system does contain the same physical constituents as a vehicle (brake pads, caliper and rotor), and the parameter space of brake pneumetic pressure and rotational speed is representative of actual driving, the process by which we simulated braking is more similar to drag braking than to the process by which vehicles are stopped. Therefore, quantifying emission factors, which are conventionally calculated as a function of driving distance, is beyond the scope of this study and will be important for future work. The modeling approach of Riva et al., which employed finite element analysis to the prediction of brake particle emissions based on braking pressure and rotational speed, is one example of a future direction for this research (Riva et al., 2019a). Additionally, most of the maximum concentrations of gas species reported in this manuscript are very high relative to observations from ambient air (Table 2.1), even after considering that species measured with I^- CIMS were calibrated assuming

the collision-limit, which produced an upper limit to the mixing ratios for all reported compounds except N_2O_5. These high concentration are not uncommon for laboratory chamber studies, as species can accumulate within the enclosed spaces and real-world ventilation cannot easily be replicated. However, the presence of these precursor gases in such high concentrations from the our simulated braking facility indicates that brake-wear emissions cannot be ruled out as a significant source of traffic emissions and warrants further investigation.

Table 2.1: Summary of ambient concentrations and mixing ratios of gas species reported in literature with associate citations. Full citations can be found in the reference section of this manuscript.

Gas Species	Ambient Quantity	Citation
N_2O_5	100 ppt - 25 ppb	Atkinson (1986), Kercher (2009)
$ClNO_2$	65-4700 ppt	Riedel (2013), Wang (2019)
SO_3	10^4-10^6 cm-3	Yao (2020)
formic acid	1-12 ppb	Millet (2015)
HNCO	1 ppt - 10 ppb	Leslie (2018)
HONO	1 ppt - 15 ppb	Kramer (2020), Li (2020)

2.5 Conclusions

Important precursor gases for ultrafine particle formation and growth were generated by braking processes simulated with a brake dynamometer system and measured using I^- CIMS. These compounds were previously unreported and included sulfuric acid, sulfur trioxide, inorganic nitrogen compounds and organic acids. Emissions from different brake pad formulations (ceramic, semi-metallic) and degrees of wear (new, gently worn and highly worn), were extremely variable, thus emphasizing the importance of representing brake-wear emissions over the lifetime of a brake pad for future control strategies. It is perhaps not surprising to observe these precursor gases from brake-wear, as brake pad formulations include a broad range of chemical compounds. However, such observations are still necessary for providing insight to this source of non-tailpipe traffic emissions and for bridging the gap between laboratory-generated braking and real-world braking emissions. Apportionment of traffic emissions measured from roadways to tailpipe and non-tailpipe sources is necessary for producing effective emission controls in the near future.

Chapter 3

Observations of gas-phase products from the nitrate radical-initiated oxidation of four monoterpenes

3.1 Abstract

Chemical ionization mass spectrometry with nitrate reagent ion (NO_3^- CIMS) was used to investigate the products of nitrate radical (NO_3) initiated oxidation of four monoterpenes in laboratory chamber experiments. α-Pinene, β-pinene, Δ-3-carene, and α-thujene were studied. The major gas-phase species produced in each system were distinctly different, showing the effect of monoterpene structure on the oxidation mechanism and further elucidated the contributions of these species to

Chapter 3 of this dissertation is a reprint of the material as it appears in: "Observations of gas-phase products from the nitrate-radical-initiated oxidation of four monoterpenes." *Atmos. Chem. Phys.* **2022**. 22, 9017–9031. DOI: https://doi.org/10.5194/acp-22-9017-2022., used with permission from Coppurnicus Publications. The co-authors listed in this publication are Danielle Draper, Andrey Marsavin, Juliane Fry, and James N. Smith.

particle formation and growth. By comparing groupings of products based on ratios of elements in the general formula $C_wH_xN_yO_z$, the relative importance of specific mechanistic pathways (fragmentation, termination, radical rearrangement) can be assessed for each system. Additionally, the measured time series of the highly oxidized reaction products provide insights into the ratio of relative production and loss rates of the high molecular weight products of the Δ-3-carene system. Measured effective O:C ratio of reaction products were anti-correlated to new particle formation intensity and number concentration for each system; however, monomer:dimer ratio of products had a small positive trend. Gas phase yields of oxidation products measured by NO_3^- CIMS correlated with particle number concentrations for each monoterpene system, with the exception of α-thujene, which produced a considerable amount of low volatility products but no particles. Species-resolved wall loss was measured with NO_3^- CIMS and found to be highly variable among oxidized reaction products in our stainless steel chamber.

3.2 Introduction

The largest uncertainty in modern climate models is attributed to the radiative effect of aerosols (Stocker et al., 2013b). Their chemical complexity makes it challenging to predict their formation as well as properties that determine their direct and indirect impacts on climate. A significant fraction of total global aerosol is secondary organic aerosol (SOA), which are formed from the oxidation of gas-phase volatile organic compounds (VOCs) to form highly oxidized species that may partition into particles or small clusters (Kroll and Seinfeld, 2008; Ehn et al., 2014; Bianchi et al., 2019). Many SOA formation pathways have been widely studied, such as the ozone (O_3) and hydroxyl radical (OH) initiated oxidation of biogenic volatile organic compounds (BVOCs) (Berndt et al., 2016; Lee et al., 2006; Atkinson and Arey, 2003b). One such system that has been shown to contribute significantly to SOA formation, but has not been as comprehensively studied, is nitrate radical-initiated (NO_3) oxidation of BVOCs (Ng et al., 2017). NO_3 radical, produced by the oxidation of nitrogen dioxide (NO_2) with O_3, is mainly anthropogenic in origin and is most abundant at night when photolysis does not occur (Brown and Stutz, 2012). BVOCs are emitted naturally by plants

and comprise a large fraction of global VOCs, but BVOC concentrations are highest in forested regions (Acosta Navarro et al., 2014). Therefore, NO_3-initiated oxidation of BVOCs is an SOA-generating system that couples anthropogenic oxidants with biogenic precursors. This chemistry has also been shown to be important in areas like the southeastern United States (Ayres et al., 2015) and the Colorado Rocky Mountains (Fry et al., 2013).

Monoterpenes (MT), unsaturated $C_{10}H_{16}$ compounds, comprise a large fraction of global BVOCs and have been shown to have a high SOA production potential from nitrate radical-initiated oxidation (Ng et al., 2017; Sindelarova et al., 2014; Ayres et al., 2015). However, the large range in SOA yield in laboratory studies of the most abundant monoterpenes, α-pinene (0-16%), β-pinene (27-104%), Δ-3-carene (68-77%) (Ng et al., 2017; Fry et al., 2014; Boyd et al., 2015; Hallquist et al., 1999), indicates that the oxidation mechanisms of these MTs have key differences. As α-pinene is often used as the representative MT in regional and global models, these oxidation mechanisms need further investigation to improve model predictions of SOA yield from MT + NO_3 systems and concomitant impacts on climate.

Recently, computational and experimental studies have shed light on the initial steps of NO_3-initiated oxidation of α-pinene, β-pinene and Δ-3-carene, all of which are bicyclic monoterpenes with a single double bond (Kurtén et al., 2017; Draper et al., 2019). These studies concluded that, following NO_3 addition onto the carbon-carbon double bond and rapid O_2 addition to the alkyl radical, first generation peroxy radical isomerization reactions are too slow to contribute to overall oxidation product distributions and instead rapidly reduce to alkoxy groups through bimolecular reactions with NO_3, HO_2 or RO_2 in the nighttime atmosphere. In the oxygen-rich atmosphere (O_2 concentration $> 10^{15}$ cm^{-3}), O_2 addition to nitroxy-alkyl radical compounds is expected to be much faster than radical decomposition (Berndt and Böge, 1995). First-generation alkoxy scissions play an important role in determining potential for further radical propagation for these monoterpenes and may help explain why the α-pinene + NO_3 system produces much lower SOA yields than β-pinene + NO_3.

First generation alkoxy scissions are affected by the position of the endocyclic or exocyclic double bond with respect to the secondary ring in these bicyclic monoterpenes (Vereecken and Peeters, 2009). The most favorable, lowest energy, first generation alkoxy scission pathway for the α-pinene + NO_3 system leads to the formation of pinonaldehyde, a closed shell species that is not very highly oxidized and thus not expected to contribute to the formation of new SOA. This contrasts the Δ-3-carene and β-pinene systems, which form alkyl radicals that allow for further radical propagation, oxidation, and internal isomerization. These processes can lead to the formation of highly oxidized gas-phase products that can readily partition into small particles. Additionally, other unimolecular processes have been shown to be competitive on the time scale of these reactions, including internal hydrogen-shift isomerization and radical rearrangement by opening the secondary ring (Vereecken and Peeters, 2010). The size of the secondary ring strongly influences the energy barrier for ring opening: four-membered rings (α-pinene, β-pinene) are unlikely to open but strained three-membered rings (Δ-3-carene) are much more susceptible to ring opening (Kurtén et al., 2017). Understanding the prevalence of these early unimolecular processes is important in determining the potential for further radical propagation and oxidation.

For this experimental study, we investigate NO_3-initiated oxidation of four monoterpenes, α-pinene, β-pinene, Δ-3-carene, and α-thujene, in a reaction chamber. The first three monoterpenes are abundant in the atmosphere (Sindelarova et al., 2014) and their oxidation mechanisms have been previously studied in laboratory experiments and theoretical computational studies. α-Thujene, a key component of frankincense oil, is less naturally abundant, but studying the α-thujene system presents a unique opportunity to assess early unimolecular processes because of its structure. α-Thujene has a three-membered secondary ring, similar to Δ-3-carene, with an adjacent double bond position, similar to α-pinene. Following NO_3 addition to the double bond, oxidation of the alkyl radical to a peroxy radical and subsequent reduction to an alkoxy radical through a bimolecular reaction is expected to occur. The first generation alkoxy scission pathways available for α-thujene mirror those of α-pinene (Figure 3.1). Cleaving the C1-C2 bond, losing the top methyl group, or the left side C2-C7 bond leading to an unstable alkyl radical on a three-membered ring would be unfavorable. Cleaving the right side C2-C3 bond generates an alkyl radical on

the nitrate-substituted carbon, which would lead to rapid radical termination with loss of NO_2, forming thujenaldehyde. If, instead, NO_3 addition onto the double bond was followed by radical rearrangement by opening the three-membered ring (C5-C7 cleavage) and subsequent tertiary alkyl radical formation, radical propagation pathways become available and can potentially lead to further oxidation and condensable species (Vereecken and Peeters, 2009). By studying the oxidation of α-thujene in addition to the previously studied MT systems, we can assess the prevalence of this ring opening reaction in the early mechanism.

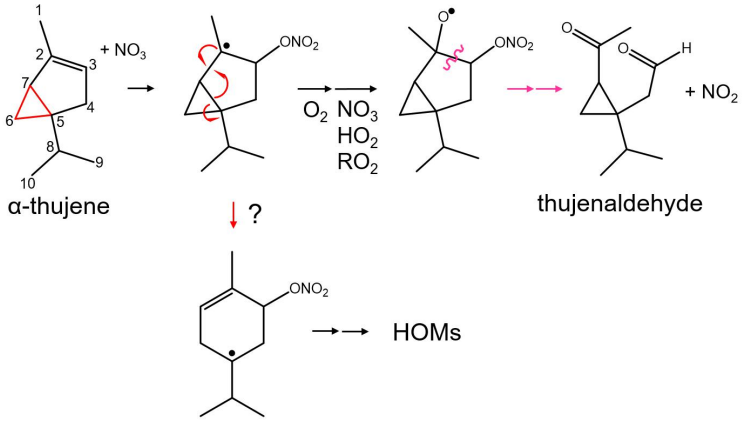

Figure 3.1: Scheme of proposed α-thujene + NO_3 oxidation mechanism. Orange arrows indicate formation of thujenaldehyde, a volatile product that is not expected to contribute to new particle formation. Downward arrow indicates a potential alkyl radical rearrangement that leads to a product that can undergo additional oxidation to form highly oxygenated molecules (HOMs).

This study is an observation of detailed compositional differences of observed gas phase oxidation products as they relate to the current understanding of oxidation mechanisms using high resolution time-of-flight chemical ionization mass spectromertry (HR-TOF CIMS) with NO_3^- reagent ion. NO_3^- CIMS has been used to measure composition of oxidized organics in laboratory studies (Berndt et al., 2015; Rissanen et al., 2014; Hyttinen et al., 2015; Mentel et al., 2015; Riva et al., 2019b) and in ambient air (Ehn et al., 2014) but has also been used specifically to probe nitrogen-containing oxidized monoterpenes (Draper et al., 2019). The NO_3^- reagent ion has been shown to cluster with highly oxidized compounds that contain at least two hydrogen bond donor sites. Therefore, we don't expect to be able to measure highly volatile aldehyde products (thujenaldehyde/pinonaldehyde) with NO_3^- CIMS, but we can probe formation of highly oxidized products and compare the differences

in composition among the four MT systems. NO_3 radical-initiated oxidation of α-thujene has not been previously studied and so the results of this particular system are unique observations. Iodide (I^-) has been used extensively in previous studies as a CIMS reagent ion, specifically to measure oxidized organics and inorganic nitrogen species (Brophy and Farmer, 2015; Aljawhary et al., 2013; Lee et al., 2014; Lopez-Hilfiker et al., 2016a). The use of both I^- and NO_3^- reagent ions could provide additional mechanistic information and is planned for future studies.

3.3 Experimental methods

We ran chamber experiments using a darkened 560 L stainless steel chamber in flow-through mode with a total flow of 17 lpm. Previously, we confirmed that operating in this manner results in conditions in which the chamber was well-mixed after ∼100 s with a residence time of ∼33 min (see SI Section 3.6.5). A schematic of our experimental set-up is shown in Figure 3.2. All experiments were performed under dry conditions. We generated NO_3 radical by oxidizing NO_2 with O_3 inside the chamber and allowing the oxidants to reach steady state (∼2 hours) before adding MT. O_3 was generated by UV photolysis of air scrubbed of NO_x ($NO+NO_2$) and VOCs by a zero air generator (Aadco Instruments, model 737-13) at 1.5 lpm. NO_2 was introduced directly from a commercially prepared cylinder (Praxair, Inc., 2.5 ppm in purified air) at 1.5 lpm. Before addition of MT, the mixing ratios of oxidants and nitrogen compounds in the chamber were as follows: $[O_3] \approx 240$ ppb, $[NO_2] \approx 240$ ppb, $[NO_3] \approx 0.2$ ppb, $[N_2O_5] \approx 25$ ppb. O_3 was measured using an absorption gas analyzer (2B Technologies, model 106-L). NO_2 was measured with both an absorption gas analyzer (2B Technologies, model 405nm) and with a home-built thermal-dissociation–cavity ring-down spectrometer (TD-CRDS, (Keehan et al., 2020)). NO_3 radical and N_2O_5 concentrations were modeled using the kinetic box model, KinSim (Peng and Jimenez, 2019), which was run on the Igor Pro computing platform (Wavemetrics, Inc., version 7). N_2O_5 was also measured by I^- CIMS and the TD-CRDS, but those measurements were performed primarily to estimate wall losses and were thus not calibrated. We introduced MT into the chamber from gas cylinders that were prepared by injecting liquid MT (supplementary information Sect. 3.6.2) into the cylinders and then pressurizing

with ultra-pure nitrogen. The mixing ratio inside the cylinders (11-20 ppb) was estimated using the mass of injected liquid and confirmed using a gas chromatograph with flame ionization detector and a home-built cryogenic preconcentrator (GC-FID). The small MT flow (25 ccm) was fed into the center of a larger zero air flow (1 lpm) with tee fitting to more effectively carry it into the chamber. Monoterpene concentrations (∼41 ppb) inside the chamber were estimated from the flow dilution and concentrations, were confirmed using GC-FID, and were modeled with KinSim. The remainder of the flow, 12 lpm, was zero air that was introduced into the chamber with a Teflon "shower head" consisting of a capped tube with holes drilled perpendicularly along the length of the tube to facilitate mixing in the chamber. We ran experiments under continuous flow and measured precursor and product concentrations for 1-2 hours until the gas-phase products reached steady state, as detected with NO_3^- CIMS. The sample lines extended into the chamber ∼20 cm in order to minimize the possibility of sampling in a gradient caused by loss of low-volatility species to the chamber walls.

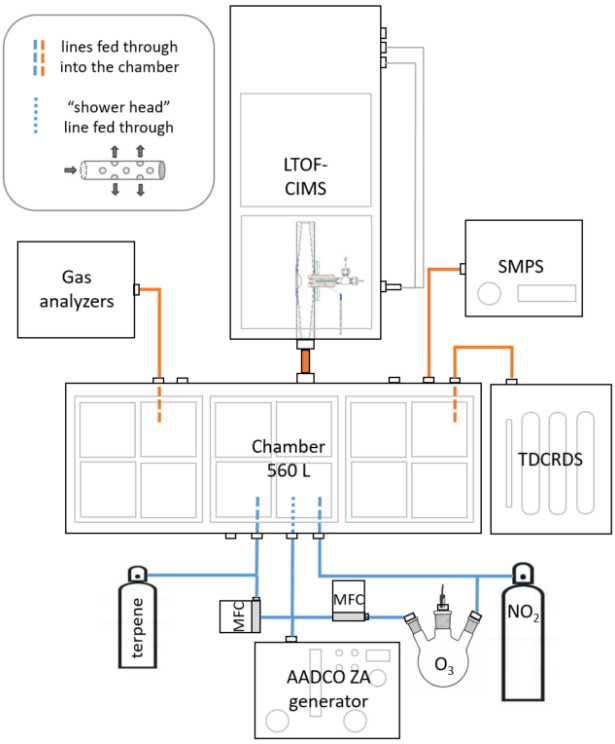

Figure 3.2: Experimental set up for chamber studies. Blue lines indicate flow going into the chamber and orange lines indicate where flow is being removed.

The TD-CRDS was used to measure nitrogen-containing species (nitric acid, alkyl nitrates (ANs), peroxy nitrates (PNs), NO_2) in both gas and particle phases (Keehan et al., 2020). The TD-CRDS measured total ANs + PNs during this experiment, and the NO_2 channel was used to parameterize the KinSim model. Additionally, a scanning mobility particle sizer (SMPS), which consisted of a differential mobility analyzer (TSI, Inc., model 3081), condensation particle counter (CPC) (TSI, Inc., model 3020), and a home-built flow and voltage controller, was used to measure the particle number-size distributions. We probed the formation of low volatility oxidation products using NO_3^- CIMS, consisting of a high resolution time-of-flight mass spectrometer (Tofwerk AG, model LTOF) operating in V-mode. We used a home-built transverse ionization CIMS inlet, in which the sample flow is perpendicular to the flow of reagent ions into the entrance orifice of the mass spectrometer (Li et al., 2019). The inlet minimizes wall losses of sampled gases and clustering with neutral compounds such as water vapor in the ion source, with an average ionization reaction time of ∼80 ms. NO_3^- reagent ion was generated by flowing ultrahigh purity N_2 gas over the head-space of a small glass vial filled with nitric acid (HNO_3). The reagent ion flow (8 ccm) was diluted with a larger flow (1 lpm) of pure N_2. Peaks in mass spectra were fitted and assigned using the Tofware software (Aerodyne Research, version 7). The reagent ion monomer (NO_3^-), dimer ($HNO_3NO_3^-$) and trimer ($HNO_3(NO_3)_2^-$) were used as calibration peaks for the low mass range. High mass calibrations were determined from the highest intensity single peaks in the monomer and dimer region clustered with NO_3 ion, and reasonable formulas were predicted from the base MT formula ($C_{10}H_{16}$). The total gas-phase product concentration was estimated using the sum of the abundance of all species detected by NO_3^- CIMS, integrated over the duration of the experiment. Integrated ion signal was converted to concentration using a calibration factor (6×10^{10} molecules cm^{-3}). This calibration factor was determined experimentally using, as a proxy, the reaction of sulfuric acid (H_2SO_4) and NO_3^- ion, which is estimated to be at the collision limit as detailed by Kürten et al. (2012). A calculation is shown in the SI in Sect. 3.6.3. We recognize that this calibration factor results is likely an upper limit for the actual concentration of organic nitrate compounds.

3.3.1 Kinetic modeling

KinSim was used to support our experiments by providing approximate concentrations of unmeasured oxidant species (NO_3/N_2O_5) and helping assess the dominant oxidant chemistry (NO_3 vs O_3) in the chamber. The rate constants for all reactions considered in the model are listed in SI Sect. 3.6.1. The chamber is assumed to be well-mixed in the model and dilution flow is also represented. Experimentally measured time series of oxidants agree well with the modeled concentrations (Figure 3.3). Experimentally measured wall loss of N_2O_5 (1.25×10^{-3} s^{-1}) was also considered in the model. This value was experimentally determined by stopping the flow of oxidants to the chamber and making up the lost flow with additional zero air, therefore "turning off" the chemistry, and using I^- CIMS to measure the decay of the N_2O_5I- cluster (SI Sect. 3.6.5). The raw $N_2O_5I^-$ decay was exponentially fitted to determine the wall loss rate. DeHaan et al. (1999) found the N_2O_5 wall loss rate of this chamber to be 9.2×10^{-5} which is somewhat lower, but the chamber was coated with parafin wax and was operated in static flow conditions for their measurements. Even though excess O_3 remains in the chamber from the generation of the NO_3, the model predicts that more than 98 % of oxidation products in all MT systems should be initiated by NO_3. This is expected, since the rate constant for the MT + NO_3 radical reaction is several orders of magnitude faster than for MT + O_3. The rate constants of NO_3 and O_3 oxidation for α-thujene are unknown and therefore cannot be modeled in the same way, so we estimated a "worst case scenario" by taking the slowest NO_3 + MT rate constant (β-pinene, 2.5×10^{-12} from Ng et al. (2017)) and the fastest O_3+MT rate constant (α-pinene, 6.0×10^{-12} from Atkinson and Arey (2003b)). This resulted in a ratio of O_3:NO_3 products of 0.1.

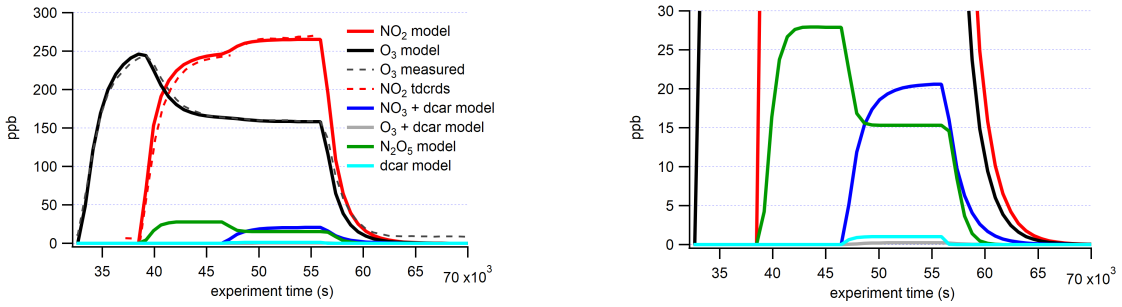

Figure 3.3: KinSim simulation of the Δ-3-carene + NO_3 experiment. Measured traces are shown with dashed lines and modeled results are shown with solid lines. Additional modeling of the other MT systems are shown in the supplemental information (Figure 3.9).

3.4 Results and Discussion

3.4.1 Oxidation product quantification

Mixing ratios of reaction products calculated from integrated concentrations were on the order of 0.1 to 0.001 ppt. Percent yield is reported for each MT system: Δ-3-carene (2.5×10^{-4}) > α-thujene (1.0×10^{-4}) > β-pinene (5.0×10^{-5}) > α-pinene (9.8×10^{-6}). Substantial wall losses were found for NO_3^- CIMS-measured species, importantly, with high variability observed among individual species and no clear trend with O:C or molecule weight (see SI Sect. 3.6.5). Therefore, individual wall loss corrections were applied for all species before calculating yield from NO_3^- CIMS measurements. Explicit wall effects were only measured for the Δ-3-carene system, so for the other MTs, average wall loss rates for monomers ($5.5 \times 10^{-3}\ s^{-1}$) and dimers ($3.4 \times 10^{-3}\ s^{-1}$) were calculated using observations from the Δ-3-carene system data and are thus subject to greater uncertainty. In contrast, wall losses of the total ANs+PNs measured by TDCRDS were observed to be negligible relative to the dilution timescale of the chamber, suggesting that the majority of this bulk organic nitrate signal is due to higher-volatility species not measured by the NO_3^- CIMS, not substantially lost to the walls, and likely not contributing substantially to SOA formation. The trend in observed molar yields of total ANs+PNs is consistent with previous measurements (Δ-3-carene > β-pinene > α-pinene), but the magnitudes (20%, 10%, 5%) are substantially lower than previous studies. This is puzzling, but may be due to the TDCRDS measurement measuring only the subset of high-volaility

nitrates in these experiments, while the lower-volatiliy nitrates have rapid wall losses that prevent the TDCRDS from measuring them. We note that the CIMS is essentially inlet-less in comparison to a 2 m inlet line for the TCRDS in these experiments.

The α-thujene system produced more highly oxidized products than the α-pinene system, and especially significant is the amount of highly oxidized dimers that were formed from α-thujene. The Δ-3-carene system generated the most particles, followed by the β-pinene system, and both the α-pinene and α-thujene systems did not generate any particles (Figure 3.9). Observed particle number trends agree with gas-phase product trends except for the α-thujene system, in which highly oxidized products formed but did not nucleate and/or grow effectively to form measurable particles.

3.4.2 Comparison of oxidation product composition

Definition of categories for elemental analysis

The experiment-averaged mass spectra for each MT system showed very different peak distributions (Figure 3.4). Here, we explore the relative ratios of experiment-averaged ion abundance from categories of products. For comparison, we normalized the integrated area of each peak by the total integrated area of all organic peaks in the mass spectrum. The general formula $C_wH_xN_yO_z$ was used to create categories of reaction products that correspond to specific predicted mechanistic pathways that are summarized in Table 3.1, with representative mechanisms for each pathway shown in Figure 3.5. Carbon number provides an indication of fragmentation caused by C-C bond cleavage for any carbon number that is not equal to 10 (for monomers) or 20 (for dimer formation from peroxy or alkoxy radical additions, e.g. RO_2 + RO_2). Hydrogen number informs us about the terminal functional group and associated bimolecular reactions leading to them. Nitrogen number can indicate secondary double bond generation or NO_2 + RO_2 chemistry from residual NO_2 in the chamber. Structure activity relationships and rate constants were found in literature for relevant pathways (Vereecken and Peeters, 2009, 2010; Novelli et al., 2021; Kurtén et al., 2017; Draper et al., 2019; Jenkin et al., 2019; Crounse et al., 2013), but proposed mechanisms were not explicitly modeled for

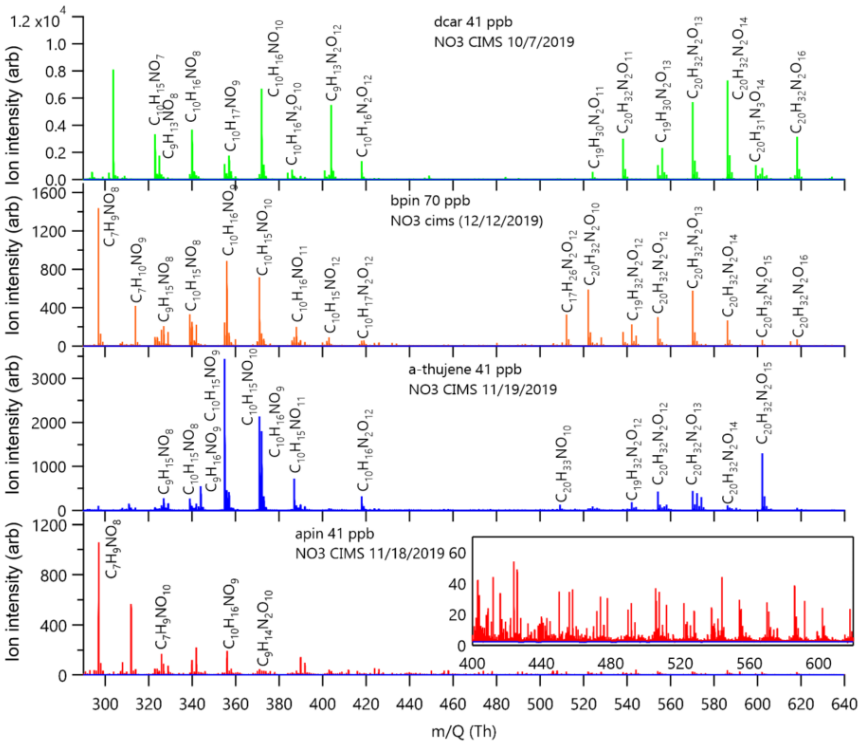

Figure 3.4: Stacked mass spectra from each MT + NO_3 system. NO_3^- reagent ion is not included in assigned formula. Left axes are raw ion counts and not normalized to the reagent ion.

this study. Oxygen number and O:C ratio provide insights into how much autoxidation chemistry occured, increasing the O:C ratio of the products. While we cannot completely explain the origin of every observed compound, the observed differences provide valuable information regarding the most important pathways that lead to these low volatility products. The ratio distributions for all the MT systems are summarized in Figure 3.6. Complete peak lists for each MT system can be found in the appendix of (Appendix A). Note that the β-pinene system ratios are an average of an 8 ppb experiment and a 70 ppb experiment (39 ppb average). The full comparison of results from both experiments can be found in the SI (Sect. 3.6.6).

Categorized monomer composition and mechanistic implications

The relative abundance of dimers compared to monomers (Figure 3.6) correlates with observed particle formation (SI Sect. 3.6.2) for each MT system, with the exception of α-thujene, for which

Table 3.1: Summary table of reaction product formulas grouped by mechanistic pathways shown in Figure 3.5. Group (a) details formation of $C_{10}H_XN_1O_Z$ reaction products, group (b) details formation of $C_9H_XN_1O_Z$ products, group (c) details formation of $C_7H_XN_1O_Z$ products and group (d) details various pathways for dimer formation.

Group	Formula	Functional groups	Pathway
A	$C_{10}H_{16}NO_z$	RO_2	MT + NO_3
	$C_{10}H_{17}NO_z$	ROOH	RO_2+H
	$C_{10}H_{15}NO_z$	R=O	RO-H
B	$C_9H_{13}NO_z$	CHO + R=O	MT - CH_3
	$C_9H_{14}NO_z$	CHO + RO_2	MT - CH_3
	$C_9H_{15}NO_z$	CHO + OOH	MT - CH_3
C	$C_7H_9NO_z$	R=O + R=O	MT - C_3H_6
	$C_7H_{10}NO_z$	R=O + RO_2	MT - C_3H_6
	$C_7H_{11}NO_z$	R=O + ROH,ROOH	MT - C_3H_6
D	$C_{20}H_{32}N_2O_z$	ROOR	$C_{10}H_{16}NO_z$ + $C_{10}H_{16}NO_z$
	$C_{20}H_{33}N_3Oz$	ROOR + ROH,ROOH	$C_{10}H_{16}NO_z$ + $C_{10}H_{17}N_2O_z$
	$C_{19}H_{30}N_2Oz$	ROOR	$C_{10}H_{16}NO_z$ + $C_9H_{14}NO_z$
	$C_{17}H_{26}N_2Oz$	ROOR	$C_{10}H_{16}NO_z$ + $C_7H_{10}NO_z$

we observed substantial dimer formation without significant particle formation. We predict that the first alkyl radical formed from NO_3 addition onto the α-thujene double bond can potentially rearrange to form a new double bond while opening the strained three-membered ring, forming a six-membered ring and new tertiary alkyl radical (Figure 3.1). That structure can then undergo further oxidation to form highly oxygenated, lower volatility compounds, including dimers. Our observations of highly oxygenated products for α-thujene shows that, under these experimental conditions, there is an additional pathway for the first generation alkoxy scission (Figure 3.1) that is competitive with the formation of thujenaldehyde.

Carbon number. Figure 3.6 summarizes the monomer carbon number distributions, which provide insights into fragmentation pathways. Detailed schemes for each MT system are shown in the SI Sect. 3.6.4. In general, alkoxy decomposition pathways (C_7, C_9) are predicted to be competitive with H migration when leaving groups become highly substituted (Novelli et al., 2021; Vereecken and Peeters, 2010). For three of the MT systems studied (Δ-3-carene, β-pinene, α-thujene), terminal sites that are available in the α position to alkoxy radicals become oxidized and lead to fast alkoxy decomposition (Figure 3.5B). For the α-pinene system, however, such a terminal site is not available. Another possible pathway for fragmentation is alkyl radical rearrangement that leads

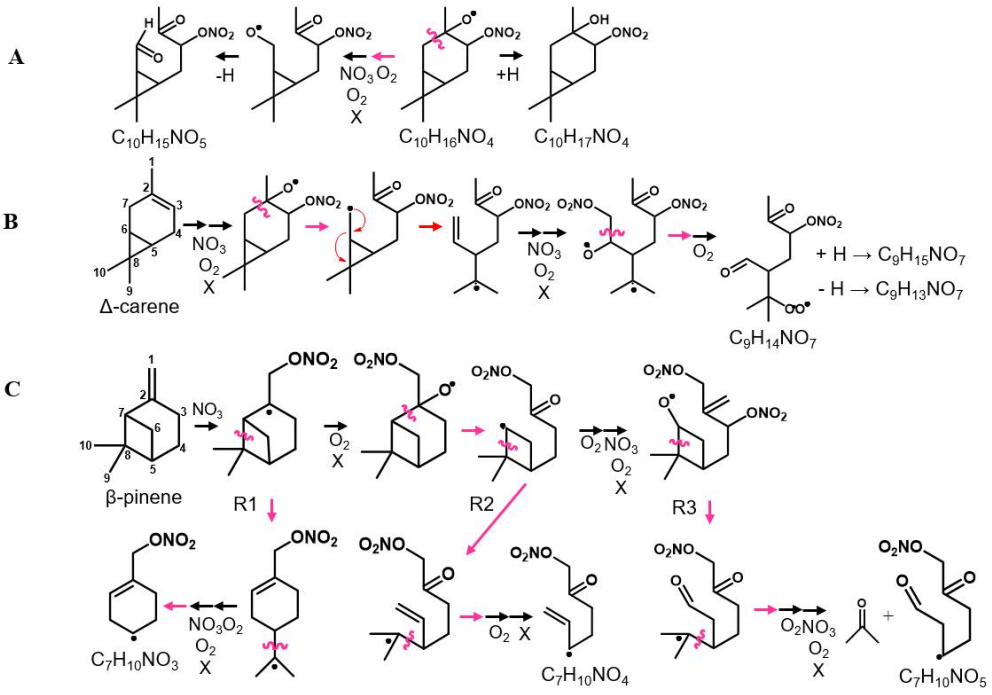

Figure 3.5: Scheme of mechanistic pathways listed in Table 3.1. Potential bimolecular reaction partners in a nighttime atmosphere (NO_3, RO_2, and HO_2) are abbreviated as X. Panel (a) shows Δ-3-carene oxidation as an example of how hydrogen number can indicate radical termination. Panel (b) shows a C_9 fragment formation pathways available to the Δ-3-carene and α-thujene systems. Panel (c) shows two potential C_7 fragment formation pathways available to the β-pinene and α-pinene systems. Note that if multiple bimolecular steps are shown under one arrow, no particular order is suggested.

to ring opening. For C_7 compounds, radical rearrangement creates new alkyl radicals in tertiary isopropyl sites (Figure 3.5C). Oxidation of the alkyl radical site to an RO_2 radical and bimolecular reaction to form an RO radical allows alkoxy decomposition to occur, generating a new alkyl radical (Kurtén et al., 2017). For C_9 compounds, ring opening and NO_3 radical addition creates a new alkyl radical in the α position to a CH_3ONO_2 group. If the alkyl radical is again oxidized (forming RO_2) and decomposed (forming RO), alkoxy scission with an ONO_2 group on the α carbon would not have a smaller energy barrier than a site with OH or OOH α substitution, but this barrier would still be smaller than an alkyl-substituted site.

Although Draper et al. (2019) observed a substantial C_7 contribution for a Δ-3-carene + NO_3 experiment with the same instrument, we observed a negligible C_7 contribution. The conditions of the two experiments were different in that the ratio of MT to oxidant was lower in our experiment

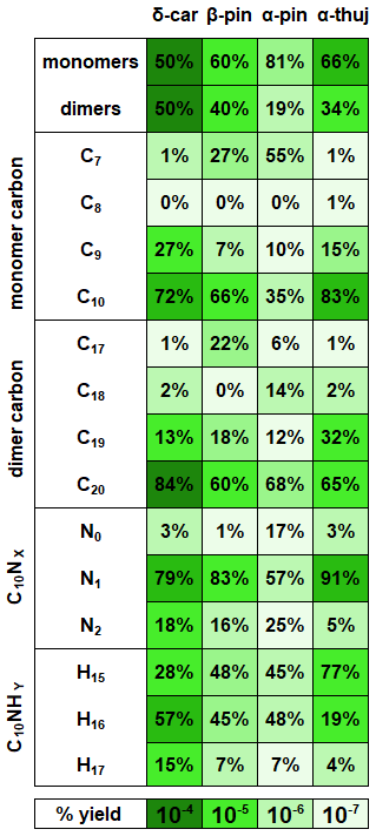

Figure 3.6: Ratios of reaction products separated into categories for each MT system. Each category for each MT system adds up to 100%. The color axis indicates magnitude of total % yield, which can be compared across the MT systems. β-pinene percentages are averaged from a high (70 ppb) and low (8 ppb) mixing ratio experiments, but the rest of the MT systems are at the same mixing ratio (41 ppb).

(0.004 vs 0.012) and the residence time for our experiment was longer (33 min vs 23 min). These differences can lead to different chemistry inside the chamber that could result in different observed reaction product distributions. We plan future studies to explore the source of these differences further. A large C_7 contribution was observed for both the α-pinene and β-pinene systems. One possible formation mechanism is shown by the R1 arrow in Figure 3.5C, in which the initial alkyl radical formed from NO_3 addition rearranges to open the four-membered ring (C7-C8 cleavage), forming a new tertiary alkyl radical. This early alkyl radical rearrangement was proposed by Boyd et al. (2015) for the β-pinene + NO_3 system. However, O_2 addition to the initial alkyl radical is expected to be fast in our experimental conditions and in the ambient atmosphere (Berndt and Böge, 1995; Kurtén et al., 2017), so we expect this alkyl radical rearrangement not to be significant. R2 in

Figure 3.5 shows an alkyl radical rearrangement that opens the four-membered ring and generates a new tertiary alkyl radical (C7-C8 cleavage). This specific ring opening reaction is not currently supported by quantum chemical modeling, so we cannot currently comment on its competitiveness. Another possibility is that this C_7 compound comes from the first-generation alkoxy scission of the C2-C7 bond (Figure 3.5C). While predicted to be a minor pathway for α-pinene, this C2-C7 scission is expected to be equally, if not more, competitive with the other two first generation alkoxy scissions (C2-C1 and C2-C3) for β-pinene (Claflin and Ziemann, 2018). This branching ratio may be somewhat reflected in the relative yields observed from the NO_3^- CIMS. The C_7 product yield from the α-pinene system is roughly half that of the β-pinene system. This early left-side C2-C7 scission makes a secondary radical on the four-membered ring, which is less stable than an acyclic analog because of ring strain (Kurtén et al., 2017). R3 in Figure 3.5C shows the proposed mechanism for this newly generated compound. In abundant O_2, this alkyl radical will be oxidized to an RO_2 radical. Because this new RO_2 radical is confined by the rigid structure of the ring, autoxidation could be slow, while in the presence of other radical species (NO_3, RO_2), bimolecular decomposition from a peroxy radical (RO_2) to an alkoxy radical (RO) could be faster. Few cyclic RO_2 H migration computational studies exist for relevant systems (Kurtén et al., 2015; Xu et al., 2019; Draper et al., 2019), but bimolecular rate constants with NO_3, NO_2 and HO_2 have recently become better defined for RO_2 radicals (Jenkin et al., 2019). Once the RO radical is formed, it is possible that decomposition of a C-C bond, thus opening the strained ring and leading to formation of a ketone and a tertiary alkyl radical, could be fast, with a predicted energy barrier of 0.6 kcal mol^{-1} from structure-activity relationships (SARs) (Vereecken and Peeters, 2009, 2010; Novelli et al., 2021). In this position, the tertiary radical resembles the structure predicted for Δ-3-carene in Kurtén et al. (2017) and could lead to the loss of the isopropyl group from C5-C8 cleavage and formation of a C_7 fragment. This pathway is only available for the β-pinene and α-pinene systems and significant contribution from C_7 compounds is only observed from these two systems.

Instead of abundant C_7 compounds, we observe a large contribution from C_9 compounds for the Δ-3-carene system and smaller C_9 signal for the rest of the MT systems. A possible pathway for C_9 formation is through the generation of a secondary double bond and subsequent NO_3 addition

(Figure 3.5B). The CH_3ONO_2 leaving group could quickly fragment into CH_3O and NO_2 (Novelli et al., 2021; Vereecken and Peeters, 2010), but is assumed to be more stable than a CH_3 radical formed from any other terminal site on the molecule in this case. The most abundant C_9 compound for the Δ-3-carene system contains two nitrogen atoms ($C_9H_{14}N_2O_{12}$). From our predicted pathway, the resulting product may contain one or two nitrogen atoms because even if the second 2 group is expected to be part of the leaving group, a radical site remains on the molecule, making the RO_2 + NO_2 pathway possible via reaction with residual 2 in the chamber. For the α-thujene system, a C_9 compound is predicted to be formed in an analogous pathway to the Δ-3-carene system, as terminal double bonds may be generated. For the α-pinene system, C_9 formation would be possible if an alkyl radical rearrangement occurred on the four-membered ring, generating a terminal double bond. Finally, for the β-pinene system, a terminal site is available after the initial right-side alkoxy scission (C2-C3), but alkyl radical ring opening could also be possible if a left-side scission (C2-C7) were to occur.

Hydrogen number. As previously mentioned, hydrogen number is an indication of the bimolecular termination pathway and the presence of the subsequent terminal functional group for RO_2 and RO radicals. For C_{10} compounds with a single nitrogen atom (Figure 3.5A), H_{15} closed shell compounds indicate aldehyde groups created from hydrogen abstraction on a carbon atom in an α position to an alkoxy radical or by other RO_2+RO_2 pathways described by (Hasan et al., 2020). $C_{10}H_{16}NO_z$ compounds are radicals, and most likely peroxy-radical compounds, as the lifetimes of alkoxy and alkyl radicals are very short. $C_{10}H_{17}NO_z$ compounds are closed shell and contain hydroxy or hydroperoxy terminal groups formed from abstracting a hydrogen atom from a different molecule. $C_{10}H_{16}NO_z$ radical compounds were the most abundant for the Δ-3-carene, β-pinene and α-pinene systems. In contrast, $C_{10}H_{15}NO_z$ aldehyde/ketone containing compounds were the most abundant for the α-thujene system and and mainly distributed among two compounds ($C_{10}H_{15}NO_9$ and $C_{10}H_{15}NO_{10}$). If one assumes that the concentration of bimolecular reaction partners is similar for each MT system, it appears that the reaction products generated in the α-thujene system included structures with especially labile hydrogen atoms in an α position to possible alkoxy radical sites. In that case, this bimolecular hydrogen abstraction reaction would be fast and lead to a high ratio

of $C_{10}H_{15}NO_z$ compounds relative to the $C_{10}H_{16}NO_z$ and $C_{10}H_{17}NO_z$ compounds. Additionally, a moderate $C_{10}H_{15}NO_z$ contribution was observed for the β-pinene system from a species with the same formula ($C_{10}H_{12}NO_{10}$).

Analogously, C_9 radical compounds with a single nitrogen atom will contain 14 hydrogen atoms if they are formed from the loss of a methyl group, while closed shell C_9 compounds will contain 13 or 15 hydrogen atoms (Figure 3.5B). For the β-pinene system, hydroperoxy or hydroxy $C_9H_{15}NO_z$ compounds were most abundant. The dominant C_9 species in the α-thujene system was a $C_9H_{16}NO_z$ species; it is not currently clear how $C_9H_{16}NO_z$ products can be formed. Surprisingly, the most abundant C_9 compounds for the rest of the MT systems do not fall into this $C_9H_xNO_z$ category, although some of these types of compounds make up a fraction of the overall C_9 signal. C_9 dinitrogen compounds were the most abundant for the Δ-3-carene ($C_9H_{14}N_2O_{12}$) and α-pinene ($C_9H_{14}N_2O_{10}$) systems, with 14 hydrogen atoms indicative of the formation of peroxy radical intermediates or an RO_2NO_2 group. Finally, C_7 radical compounds with a single nitrogen atom are predicted to have 10 hydrogen atoms if formed by the loss of an isopropyl group, while closed shell C_7N_1 compounds will have 9 or 11 hydrogen atoms (Figure 3.1C). The most abundant C_7 compound ($C_7H_9NO_8$), observed for both the β-pinene and α-pinene system, was closed shell and its formula is consistent with the mechanism we present in Figure 3.5C, but a large radical contribution from $C_7H_{10}NO_9$ was also measured in the β-pinene system.

Nitrogen number. Monomer compounds with a single nitrogen dominate all MT systems, but with varying abundance. Initial addition of NO_3 radical leads to the formation of these single nitrogen-containing compounds. The α-pinene system had much higher contributions from N_0 and N_2 compounds compared to the other MT systems, but it is expected that the majority of products detected for the α-pinene system come from minor pathways, so unusual pathways that are normally considered to be slow can potentially be competitive and lead to the observed ratios of nitrogen-containing compounds. We are not currently certain what those pathways are. The α-thujene system had a 10% greater contribution from single nitrogen-containing compounds compared to the Δ-3-carene and β-pinene systems, and a corresponding 10% smaller contribution from dinitrogen compounds. α-Thujene and Δ-3-carene both contain strained three-membered rings that can make

a ring opening alkyl radical rearrangement reaction faster than the MTs with less strained four-membered rings (β-pinene, α-pinene) (Kurtén et al., 2017). Therefore, it is not possible to know for certain how many nitrogen atoms have been lost by a molecule in the process of oxidation. It is not possible to attribute a product containing a single nitrogen to the initial NO_3 radical addition to the parent α-thujene molecule. This pathway would be available early in the oxidation mechanism for α-thujene, but Δ-3-carene requires one generation of oxidation to pass before the secondary double bond can be generated (Sect. 3.1). Additionally, the Δ-3-carene system has other pathways that can lead to highly oxidized species whereas the α-thujene system is currently predicted to only have one pathway that leads to secondary double bond generation. Dinitrogen compounds can be formed via NO_2 + RO_2 (from excess 2 in the chamber) and this can also form a product with two nitrogen atoms. The rate constant for this NO_2 + RO_2 reaction is highly uncertain, making explicit kinetic modeling of the RO_2 fate challenging.

Categorized dimer composition and mechanistic implications

Carbon number. C_{20} compounds were the most abundant dimers across all MT systems. However, the β-pinene system had a large (22%) C_{17} contribution, whereas the other MT systems produced negligible (<6%) C_{17} dimers. Correspondingly, a large C_7 monomer contribution was observed for the β-pinene system and not for the Δ-3-carene or α-thujene systems. C_{19} dimers were produced in all MT systems, but the α-thujene system had $\sim$ 20% greater fractional C_{19} contribution than β-pinene (10%) and Δ-3-carene (18%), even though the Δ-3-carene system produced the highest percentage of C_9 monomers. Dimers with carbon numbers other than 20 imply that after alkoxy decomposition and fragmentation of a C_{10} monomer, the newly generated monomer fragment must contain an active radical site. This can occur through the generation of a secondary double bond within one of the monomer units through alkyl radical rearrangement. Another possibility is that the smaller leaving group is a closed shell species, leaving the larger fragment with an alkyl radical. A possible example of this rearrangement is shown in Figure3.1C, in which a C_7 radical is generated with acetone as the leaving group in the β-pinene system. That C_7 alkyl radical can be oxidized and possibly form an adduct with a C_{10} radical, making a C_{17} dimer that is uniquely observed for

the β-pinene system. C_{19} dimers can potentially be formed through a similar radical rearrangement pathway discussed above in Sect. 3.4.2. It is possible to create a C_{19} dimer from that C_9 fragment, as another active radical site could exist on the molecule after NO_3 radical addition to the newly generated double bond. An analogous C_9 and C_{19} dimer could be formed from the α-thujene and β-pinene systems.

Hydrogen number. Closed shell C_{20} compounds formed from two $C_{10}H_{16}$ compounds (RO_2 + RO_2) have 32 hydrogen atoms and were the most abundant type of dimers in all MT systems. If C_{20} compounds have an alternate hydrogen number, it is assumed that a second double bond was generated at some point during the oxidation process, forming a monomer species with both an active radical site and a terminated site (CHO, OOH, or OH). $C_{19}N_2H_{30}$ compounds make up ~80% of total observed C_{19} signal from the Δ-3-carene system and are predicted to form via the addition of a $C_{10}H_{16}NO_z$ radical and a $C_9H_{14}NO_z$ radical. In contrast, the β-pinene system produced $C_{19}H_{32}N_2O_z$ compounds with the highest abundance among C_{19} species, and the α-thujene system produced both $C_{19}H_{30}N_2O_z$ and $C_{19}H_{32}N_2O_z$ compounds with equal intensity. As with the C_9 monomer units, it is uncertain where the extra two hydrogen atoms are gained. For the β-pinene system, $C_{19}H_{26}N_2O_z$ molecules were the most abundant C_{19} species, which is consistent with a $C_7H_{10}NO_z$-RO_2 monomer fragment combining with a $C_{10}H_{16}NO_z$-RO_2 monomer.

Nitrogen number. For C_{20} dimers, a nitrogen number of two can correspond to addition of RO or RO_2 radicals with one substituent ONO_2 group each. It is expected that products without nitrogen atoms lose them in termination steps. Thus, dimers with two nitrogens cannot be formed by the addition of a dinitrogen monomer and a monomer with no nitrogen atoms unless two radical sites are available on the same molecule and one participates in RO_2+RO_2 adduct formation while the other leads to the loss of NO_2. This would create a monomer with no nitrogen atoms that is also bonded to another monomer unit. C_{20} dimers containing two nitrogen atoms are the most abundant across all MT systems. Very small contributions are observed from N_3 or N_4 C_{20} species. The α-thujene system has a considerable contribution (13%) from single nitrogen-containing dimer species. The single nitrogen-containing compounds can possibly be formed by the same combination of monomer units mentioned above for $C_{20}N_2$ compounds, except one of the monomers contains only a single

nitrogen atom instead of two. Additionally, it is possible that ozonolysis-RO_2 and nitrate-RO_2 intermediates engaging in cross reactions play a role, as the rate constant for α-thujene with ozone or NO_3 radical has not been measured.

3.4.3 Effective O:C ratio of oxidation products

The average, weighted O:C ratios for total detected organic reaction products are as follows: Δ-3-carene (0.71), β-pinene (0.62), α-thujene (0.45), and α-pinene (0.73). The reported effective O:C ratio for all molecules does not include the oxygen atoms from the nitrate group (two oxygen atoms subtracted for every NO_3 group). Even though the average O:C ratio correlates with observed particle formation for every system except α-pinene, the effective O:C ratio distribution is very different for all systems (Figure 3.7). Additionally, if products are grouped into monomer and dimer species, the effective O:C ratios do not necessarily correlate with observed particle formation. For monomer species, the average effective O:C ratios were found to have an opposite trend with the intensity of new particle formation events, with the Δ-3-carene reaction products having the lowest effective O:C (0.700) followed by β-pinene (0.724), α-thujene (0.771), and α-pinene (0.780). The dimer products do not show a trend with effective O:C ratios: Δ-3-carene (0.37), β-pinene (0.43), α-thujene (0.37), and α-pinene (0.50). In general, we observe lower O:C ratios for dimers compared to monomers. If the average O:C for the dimer compounds is around 0.4, they were possibly formed from monomers with an average O:C of 0.6. The average monomer O:C observed from all experiments was 0.7. For the α-thujene system, the majority of the monomer species and the dimer species are centered in a narrow effective O:C range. This is in contrast to the observations from the other MT systems. If the three-membered ring is opened early on in the oxidation mechanism, and the subsequently generated double bond is attacked by a NO_3 radical, the molecule will be symmetrical in one plane (Figure 3.1). It is possible that this symmetry leads to a lack of diversity of products, reducing the possibility of structurally unique products by half. It is important to note that NO_3^- CIMS is selective towards highly oxidized species, so the oxygen distribution reported here is within the limits of the sensitivity of the reagent ion. Every O:C bin is assumed to be ionized with the same efficiency.

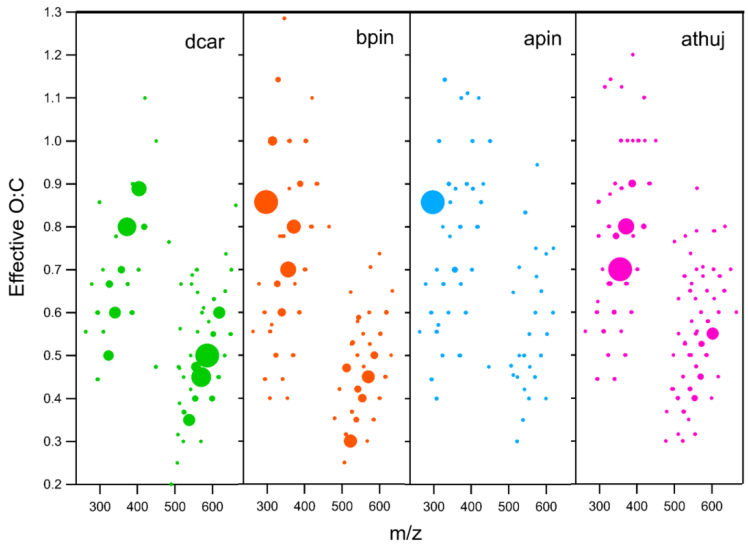

Figure 3.7: Effective O:C ratio plotted versus m/z for all measured oxidation products. Plots include oxygen atoms only on the carbon backbone. Each marker represents one compound, and marker area is proportional to signal intensity. Note that each MT system is scaled to its own maximum intensity, thus marker sizes cannot be compared across MT systems. The β-pinene plot shown is for the high mixing ratio (70 ppb) experiment, and all others are 41 ppb

Temporal analysis of oxidation products

When comparing the uncorrected (not corrected for wall losses) time series traces for each MT system, a decrease in product signal after the initial increase was observed for the two systems (Δ-3-carene, β-pinene) that exhibited new particle formation (Figure 3.8). These decreases roughly correspond to increasing particle number. More quantitative analysis of particle growth rates is beyond the scope of the current study, but is planned for future studies. The decrease in gas-phase products over the course of the experiment was not observed for the MT systems that did not produce particles (α-pinene and α-thujene).

Different reaction products have different time series because of different formation rates and sinks, as observed in the Δ-3-carene system. At this time, this analysis is only available for the Δ-3-carene system; however, we expect similar behavior for the products of the other MT systems. By grouping the individual species into the categories detailed in Sect. 3.4.1, insights can be gained into the net formation time ($x_{1/2}$), which takes into account wall loss but not loss due to condensation

sink on particles. The time series curves were fitted to sigmoidal curves to determine the time it took for the signal to reach one-half the maximum ($x_{1/2}$). In general, monomers were found to have faster net formation time $x_{1/2}$ than dimers (Figure 3.8). $C_{10}H_{16}NO_z$ compounds have the fastest $x_{1/2}$ and are the most abundant monomer species. Most of these species are also single nitrogen-containing compounds. Within the N_1 category, $C_{10}H_{16}NO_z$ compounds and $C_{10}H_{17}NO_z$ compounds have similar $x_{1/2}$ times, whereas the $C_{10}H_{15}NO_z$ species have a slower $x_{1/2}$ overall, falling into the same $x_{1/2}$ regime as the dimer compounds. If assuming these C_{10} compounds all have a similar condensation sink rate, it appears that H_{16} radicals and H_{17} hydroxy and hydroperoxy compounds form faster than the H_{15} carbonyl compounds. C_9 compounds have more variable $x_{1/2}$ times, but are, in general, slower than the fastest C_{10} monomers. Additionally, the most abundant C_9 species ($C_9H_{14}N_2O_{12}$) has an $x_{1/2}$ value in the dimer region (note that this compound contains two nitrogen atoms). Additionally, for C_{10} compounds with one nitrogen atom, there is an almost imperceptible increasing trend relating $x_{1/2}$ and effective O:C ratio (Figure 3.8b). A similar slight trend can be observed for C_{20} compounds. It is possible that, because the formation and sink times cannot be isolated, more highly oxidized molecules take longer to form but also condense more rapidly.

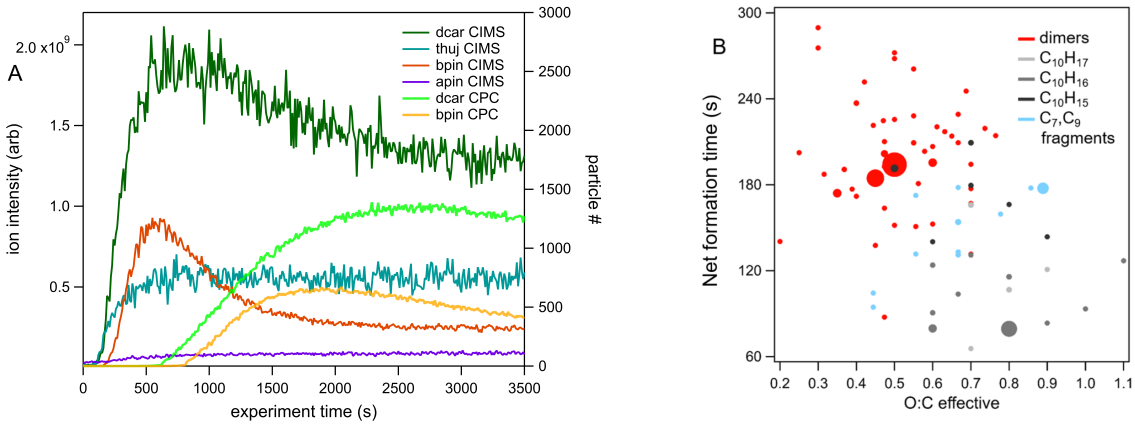

Figure 3.8: (a) Time series of total organic compounds for each MT system measured with NO_3^- CIMS plotted with associated particle number concentration. The β-pinene traces shown are from the high concentration (70 ppb) experiment. (b) Formation:sink ratio of reaction products of the Δ-3-carene system plotted against effective O:C ratio.

3.5 Conclusions and implications for atmospheric chemistry

NO_3^- CIMS has been used to probe the composition of NO_3-MT oxidation products in laboratory chamber experiments in order to gain mechanistic insights. The major detected species formed in each system were distinctly different, showing the effect of MT structure on the oxidation mechanism. We initially hypothesized that the structural similarities between α-thujene and α-pinene would lead to the dominance of relatively high-volatility oxidation products thujenealdehyde and pinonaldehyde, respectively. Our results, however, suggest that an alkyl radical rearrangement can lead to an intermediate that can undergo additional oxidation and form HOM monomers and dimers (Figure 3.1) in α-thujene oxidation. The lack of measurable new particle formation in spite of the presence of these dimers indicates a more complex relationship between HOMs and new particle formation. This should be studied in greater detail to provide insights into the ability of HOMs to participate in nanoparticle formation and growth.

For all systems, HOM carbon number, an indicator of fragmentation pathways, supports the notion that decomposition is more likely when leaving groups become highly substituted. The presence of substantial amounts of C_7 fragments for the β-pinene and α-pinene systems is consistent with the loss of an isopropyl group from those species and we have hypothesized the mechanism by which this occurs (Figure 3.5c). Hydrogen number for $C_{10}N_1$ compounds, an indicator of termination pathways and the presence of closed-shell or radical intermediates, show the dominance of peroxy radical H_{16} compounds for all but the α-thujene system, the latter of which was dominated by closed-shell H_{15} aldehydes or ketones. For C_9N products, closed shell H_{15} hydroperoxy or hydroxy compounds dominated the β-pinene system and H_{16} species dominate the α-thujene system by a mechanism that is unclear to us. For α-pinene and Δ-3-carene systems, the dominant C_9 compounds detected were species containing 2 nitrogen atoms and 14 hydrogen atoms. The dominant C_7 fragment observed for α-pinene and β-pinene was a closed-shell $C_7H_9NO_8$ compound with possible isomers, again consistent with the mechanism we propose in Figure 3.5C. Nitrogen number for all monomers was dominated by those containing a single nitrogen atom, which arises from the initial NO_3 radical

addition. Some later generation monomeric dinitrogen compounds were detected in all systems with the exception of α-thujene, the latter of which has fewer pathways for the formation of a second double bond. This limitation may be partly responsible for the lack of observed new particle formation forα-thujene despite the abundance of HOMs in that system.

The observed dimers included major peaks containing 20, 19, and 17 carbon atoms, which is consistent with the observed monomers containing 10, 9, and 7 carbon atoms. Hydrogen numbers for all systems indicate that C_{20} dimers form predominantly closed-shell compounds with 32 hydrogen atoms. In general, our observations of hydrogen and nitrogen number in detected dimers are consistent with the composition of detected monomers, which suggests dimer formation by cross reactions between nitrate-containing RO_2 species.

Detected O:C ratios of gas-phase products provide some insights into NPF mechanisms. In general, monomer O:C ratios share a very small trend with new particle formation intensity. It is possible that monomers with higher O:C ratios are preferentially partitioning into growing nanoparticles and, indeed, we observe a decrease in HOMs coincident with an increase in the concentration of newly formed particles as discussed in Sect. 3.4.3.

Finally, our temporal analysis of oxidation products from the Δ-3-carene system shows unique, species-dependent formation rates and provide insights into wall loss rates. In general, dimers formed more slowly than monomers. Since dimers had lower O:C ratios, there was a weak anti-correlation between O:C ratio and the net formation time. This correlation is not apparent for monomers, but C_{10} monomers did display some trends such as H_{16} radicals and H_{17} hydroxy and hydroperoxy compounds forming faster than H_{15} carbonyl compounds. Additional applications of this temporal analysis approach for the other MT systems would be an interesting extension of this work.

The information gained from this detailed comparison of gas-phase composition with currently established mechanisms provides new information on these oxidation processes and further elucidates the effect of these species on particle formation and growth. A wider range of oxidation products (SVOCs) need to be measured to observe the compounds not detected by NO_3^- CIMS in order

to more comprehensively draw conclusions about particle formation potential. Further analysis of particle formation rate, particle composition and modeling of energy barriers for some of the proposed mechanistic pathways is needed. Additional spectroscopy can also be useful for confirming the presence of functional groups.

3.6 Supplemental Information

3.6.1 KinSim model rate constants and results

Summary of rate constants used for the model are shown in Table 3.2 and results for the a-pinene and b-pinene systems are shown in Figure 3.9. Most come from the JPL Kinetics Data Evaluation (JPL 2015) or the IUPAC Evaluated kinetic and photochemical data for atmospheric chemistry (IUPAC 2006). The rate constants for a-thujene have not been measured and therefore, the a-thujene system was not modeled.

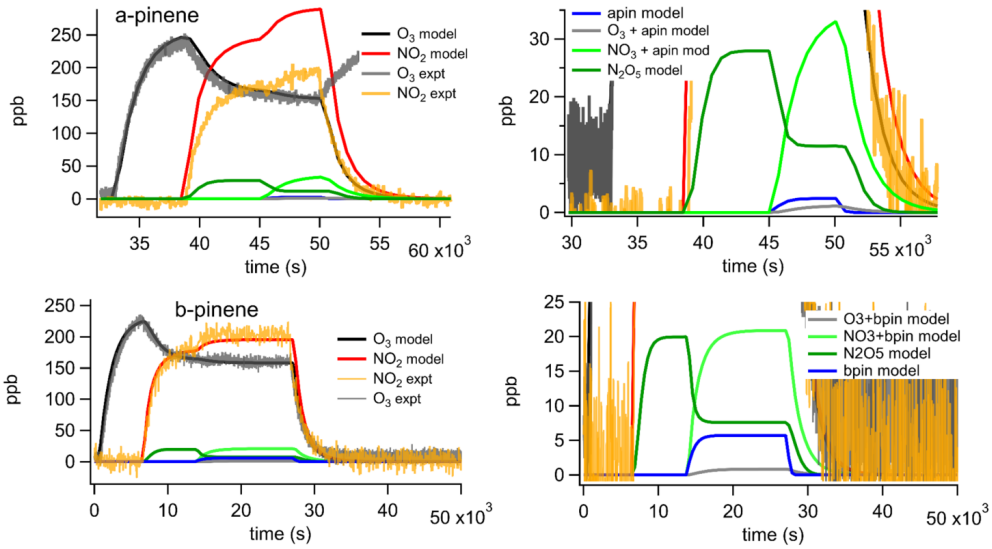

Figure 3.9: KinSim model results for the a-pinene and b-pinene systems. For the a-pinene system, initial modeled NO_2 concentration was made to match experimental NO_2, but magnitude was scaled to make modeled O_3 fit experimental O_3 because the magnitude of the O_3 measurement was more reliable.

Table 3.2: Table of rate constants used for modeling experiments.

Rate Constants Used for KinSim Modeling					
reactant	**reactant**	**product**	**product**	**k (s-1)**	**source**
NO	O3	NO2	O2	1.96E-14	JPL
NO2	O3	NO3	O2	5.70E-17	JPL
NO2	NO3	N2O5		1.24E-12	JPL
N2O5		NO3	NO2	0.0445	IUPAC
NO	NO3	NO2	NO2	2.60E-11	DeMore et al. 1994
NO3	MT	RO2		(dcar) 9.1E-12 (bpin) 2.5E-12 (apin) 6.2E-12	Ng et al. 2017 & Calvert et al. 2002
O3	MT	ProdO3MT		(dcar) 3.70E-17 (bpin) 2.25E-17 (apin) 8.00E-17	Khamaganov et al. 2001
N2O5	H2O	HNO3	HNO3	9.67E-05	
DILUTION1				0.0006	
O3source		O3		0.0006	
MTsource		MT		0.0006	
NO2source		NO2		0.0006	
N2O5		N2O5wall		0.00125	Measured
NO3		NO3wall		0.0104	
RO2	RO2	PRO2RO2		2.00E-15	Ziemann and Atkinson 2012
RO2	NO3	PRO2NO3		2.00E-12	Orlando and Tyndall 2012
RO2	NO2	RO2NO2		2.00E-12	JPL
RO2NO2		RO2	NO2	3.60	
RO2NO2		RO2NO2wall		0.00125	

3.6.2 Monoterpene chemical information

(-)-beta-pinene >94.0% purity, TCI Chemicals, CAS 18172-67-3.

(+)-3-carene >90.0% purity, TCI Chemicals, CAS 13466-78-9.

(+)-alpha-pinene 98% purity, Sigma Aldrich, LOT SHBH5409V.

alpha-thujene: We isolated alpha-thujene by fractional distillation of commercially-available Boswelia serrata (frankincense) essential oil. We kept the temperature of the distilling flask at 175 C and collected 5 mL of the vapors that were first to condense. We then repeated the process 2 more times to get a small sample of triple-distilled oil. We estimated the composition of the sample by running GC-MS. The sample was 93% a-thujene in July 2019 and 91% in November 2019, so we are assuming the sample was >90% pure when we ran the chamber experiments. The most significant impurity is a-pinene. The frankincense oil we used was about 65% a-thujene prior to distillation.

For GC analysis, we used a Varian Saturn GCMS with a Restek dimethyl polysiloxane 30 m column and ether as the solvent. Initial oven temperature was 50 C, then ramp to 200 C at 10 C/min for 15 minutes.

3.6.3 Particle size distributions

Size distributions of each MT system were measured using an SMPS system. New particle formation was observed for the d-carene and b-pinene systems and no particle formation was observed for the a-thujene and a-pinene systems.

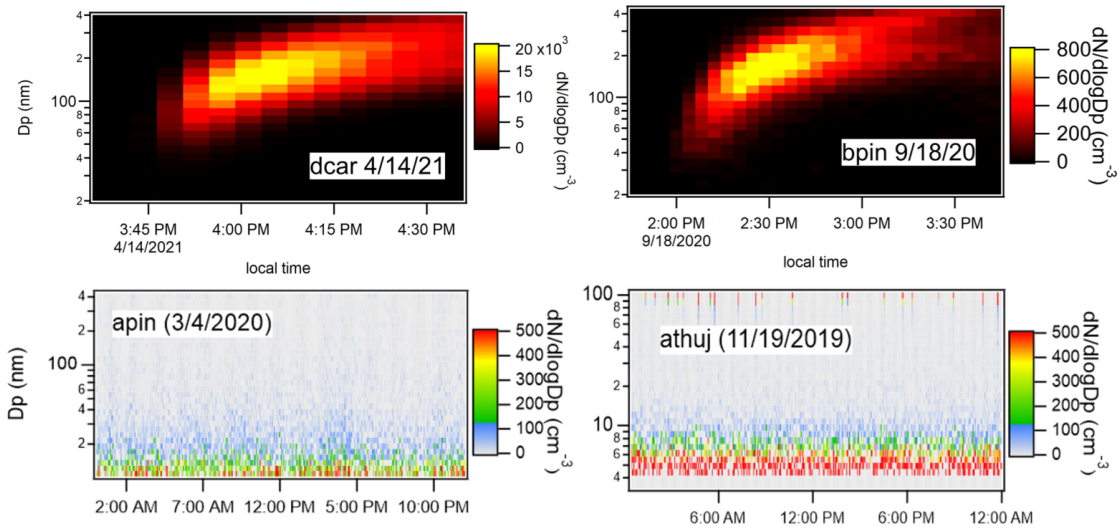

Figure 3.10: Particle size distributions of each MT system.

3.6.4 CIMS yield processing

Peaks were fit and integrated using Tofware. Equation (1) details the yield calculation. The integrated signals for every peak were summed, divided by the reagent ion (NO_3, multiplied by the calibration factor (Fcal = 6×10^{10}), averaged over the duration of the experiment to find the raw number of molecules generated. That number was multiplied by the wall loss correction factor

(Fcor) for monomers (1.29) and dimers (1.49) separately, then multiplied by the flow rate going into the inlet of the mass spec to find molecules cm^{-3}.

$$\frac{\frac{\sum int}{NO_3^-} \times Fcal}{time} \times Fcor \times flow^{-1} = cm^{-3} \tag{3.1}$$

3.6.5 Detailed mechanisms for each MT system

Mechanisms for each MT system are shown in this section. "X" corresponds to bimolecular reactions with nighttime radicals ($NO_{3H}O_{2R}O_2$). Blue arrows indicated alkoxy scission pathways and red arrows indicate aklyl radical rearrangement ring opening reactions. ROOR indicate dimerization reactions and EP indicate RO_2 epoxide forming reactions.

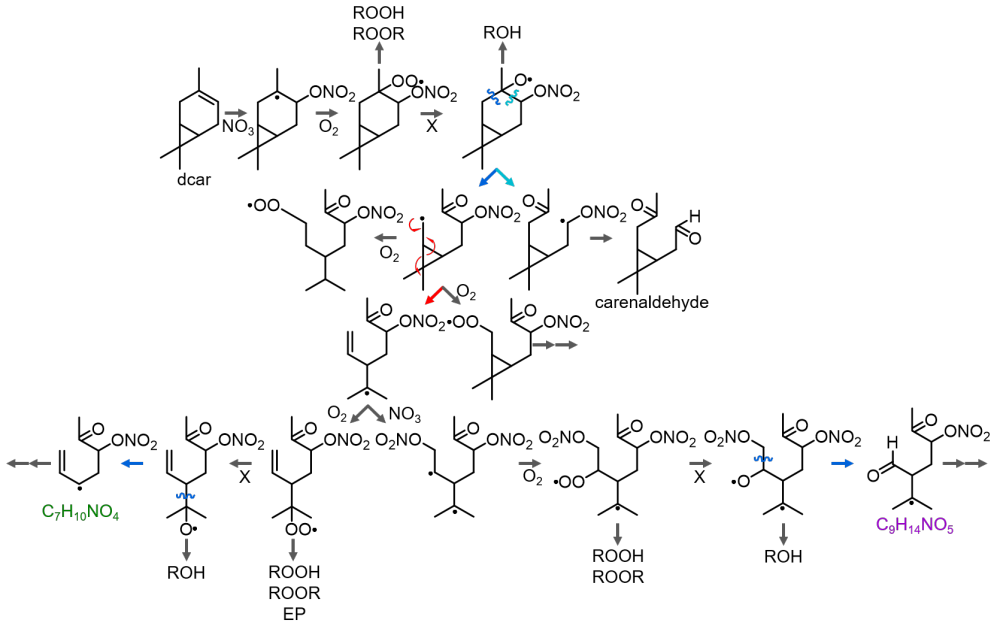

Figure 3.11: Detailed NO_3 + d-carene mechanism scheme.

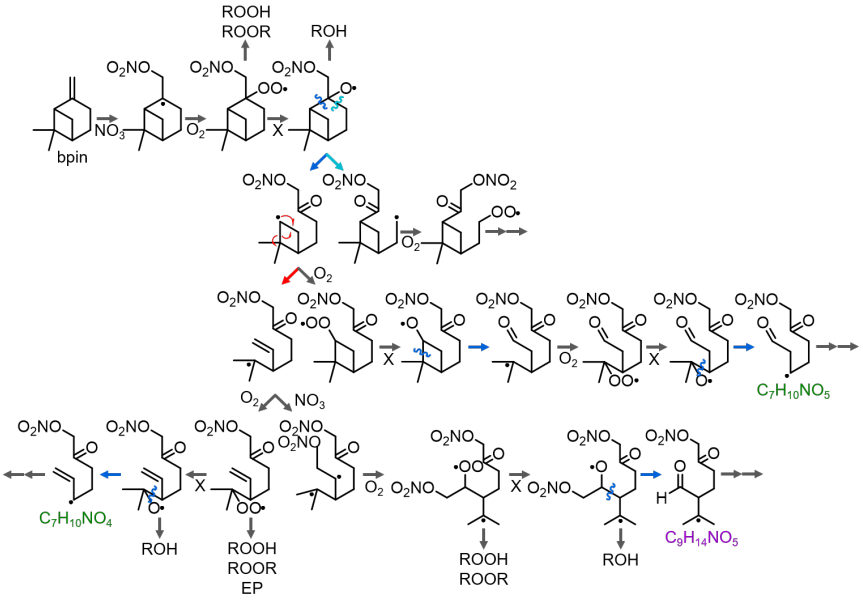

Figure 3.12: Detailed NO_3 b-pinene mechanism scheme.

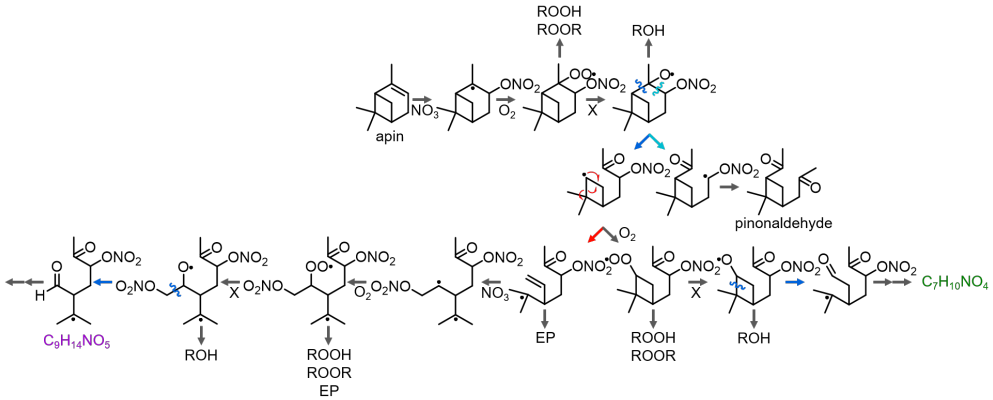

Figure 3.13: Detailed NO_3 a-pinene mechanism scheme.

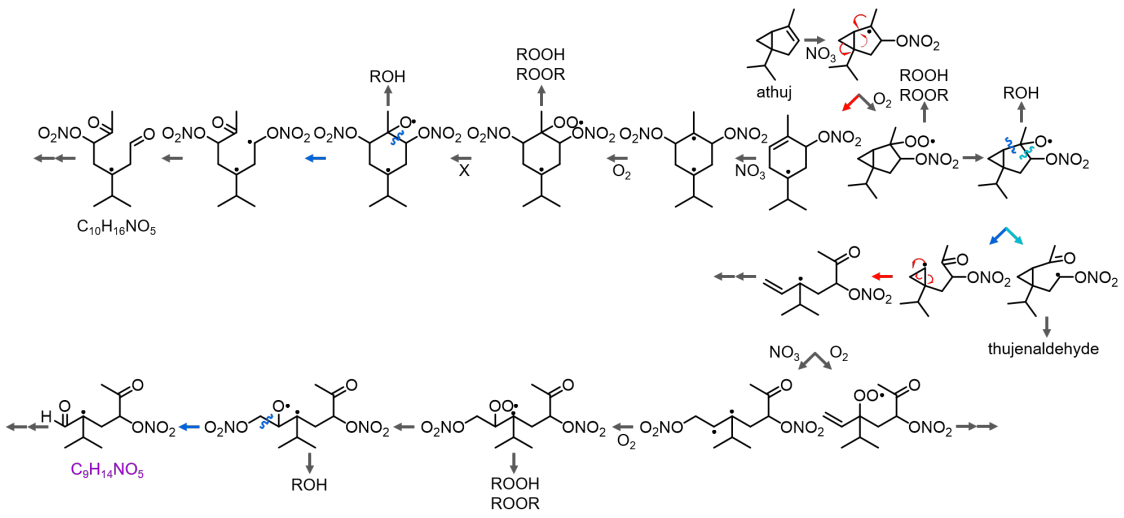

Figure 3.14: Detailed NO_3 a-thujene mechanism scheme.

3.6.6 Wall loss of N_2O_5 and dcar + NO_3 products

N_2O_5 was measured using I-CIMS with the same inlet configuration (TI) used for NO3-CIMS. I-ion was produced by filling a Teflon permeation cell with liquid methyl iodide and flowing ultrahigh purity N_2 over a sealed stainless steel canister containing the permeation cell. I^-,I_2^-, IN_2O_5, and $IHNO_3$ were used as calibration ions. Peaks were analyzed using Tofware in Igor Pro (version 7). The decay of N_2O_5 was fitted to an exponential function and the k value was found to be 1.25×10^{-3} s^{-1}.

Wall losses for individual species were measured for the dcar system by observing the time traces of ion abundance when the ion production term is zero and therefore the concentration of species A normalized by the initial concentration is determined by first order loss rates due to dilution (k_{dil}) and wall deposition (k_{dep}) as follows:

$$[A]/[A]_o = exp\,[-(k_{dil} + k_{dep})t].$$

These conditions were created by allowing the gas phase species to reach steady state, then shutting off the oxidant and dcar flow into the chamber. The missing flow was made up with zero air in order to maintain a constant dilution rate. We used NO_2 to determine k_{dil}, since prior experiments using the same chamber reported a wall loss rate of this compound of 10^{-6} s^{-1}, about 3-4 orders of magnitude higher than wall loss rates observed for oxidation products in this study (DeHaan et al., 1999). The value of k_{dil} can thereby be taken from an exponential fit of the NO_2 data according to:

$$[NO_2]/[NO_2]_o = exp(-k_{dil}t).$$

The wall loss rate for each species, A, can be calculated directly from the measurements by dividing the normalized NO_2 concentration by the normalized concentration of species A:

$$\frac{[NO_2]/[NO_2]_o}{[A]/[A]_o} = \frac{1}{exp(-k_{dep}t)} = exp(k_{dep}t).$$

Since the values of k_{dil} and k_{dep} are small compared to the time scales of these experiments, we can make the simplifying assumption that the exponential terms can be replaced by their Taylor

expansion, i.e., $e^{-x} \approx 1 - x$. With this simplification, the ratio shown above can be replaced by linear terms as follows:

$$[NO_2]/[NO_2]_o - [A]/[A]_o = exp(-k_{dil}t) - exp(-k_{dil}t)exp(-k_{dep})$$

$$[NO_2]/[NO_2]_o - [A]/[A]_o = (1 - k_{dil}t) - exp(-k_{dep}t) + k_{dil}t * exp(-k_{dep}t)$$

If we assume $k_{dil} << k_{dep}$, or zero:

$$[NO_2]/[NO_2]_o - [A]/[A]_o = 1 - exp(k_{dep}t).$$

Figure 3.15 shows an example of this analysis. The figure shows the normalized decay curves for NO_2 and a representative C_{20} compound. It also shows the difference curve, to which we fit an exponential function in order to calculate k_{dep}. These values of k_{dep} for each detected species were used to correct the measured ion abundance for wall losses, as show in the right plot of Figure 3.15. These traces were fitted to sigmoidal curves to find the net formation time of each individual compound, as shown in Figure 3.16. Overall, the net formation times were greatly affected by the wall correction. Shifts of up to one minute in the positive or negative direction were observed, but monomers tended to have positive shifts smaller in magnitude and dimers had larger shifts in both directions.

Chamber mixing was characterized by performing experiments measuring CO_2. Experiments were conducted at 20 LPM inlet flow with CO_2 added to the chamber. Following this we flushed the chamber with CO_2-scrubbed zero air. A Licor CO_2 analyzer measured CO_2 concentration. Figure 3.17 shows the results along with the best fit line for the decay of CO_2. We then fit the data to an exponential equation for dilution in a continuously stirred chamber in order to calculate the average residence time at this flow rate. The result at this flow rate, 1657 s, is to be compared to the theoretical residence time associated with a well-mixed chamber of 1680 s. This close correspondence is found at flow rates ranging from 10 - 60 lpm and confirms that our use of Teflon "shower heads" to introduce gasses into the chamber creates satisfactory mixing in the chamber.

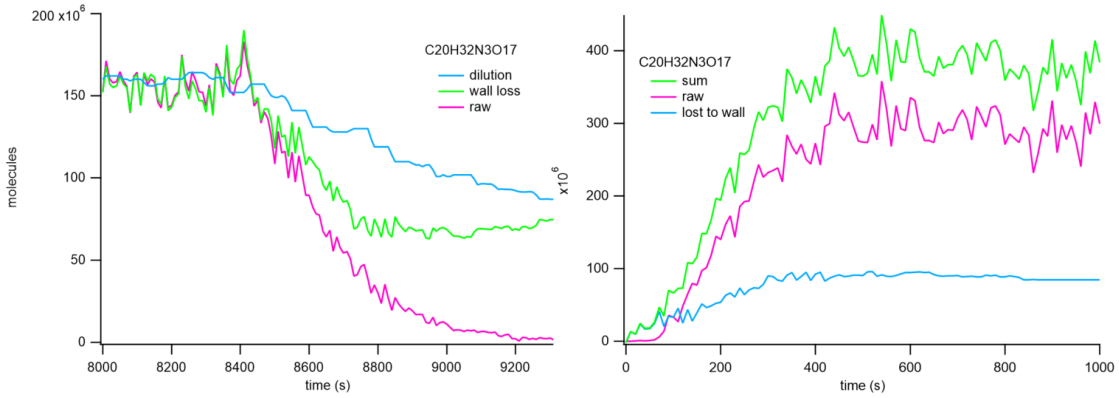

Figure 3.15: Manipulated time series trace of one species ($C_{20}H_{32}N_2O_{14}$ without reagent ion) as an example of how wall losses are calculated and formation times corrected. In the left plot, the pink trace shows the raw decay of $C_{20}H_{32}N_2O_{14}$, the blue trace shows decay of NO_2 which represents dilution in the chamber, and the initial intensity subtracted by the difference between the dilution trace and the raw trace. The right plot shows the raw formation of $C_{20}H_{32}N_2O_{14}$ (pink), the amount of this compound that is expected to be lost to the chamber walls (blue) and the sum of those two traces (green).

The mixing time for our experiments is approximately 100 s. This value arises from experiments performed in which a pulse of CO_2 was introduced into the chamber at t = 0 s, after which we observed the mixing process and decay of CO_2. Figure 3.18 shows that it takes ∼100 s for the CO_2 to reach its peak value, which is equal to the theoretically predicted value based on the concentration of CO_2 added and the dilution ratio.

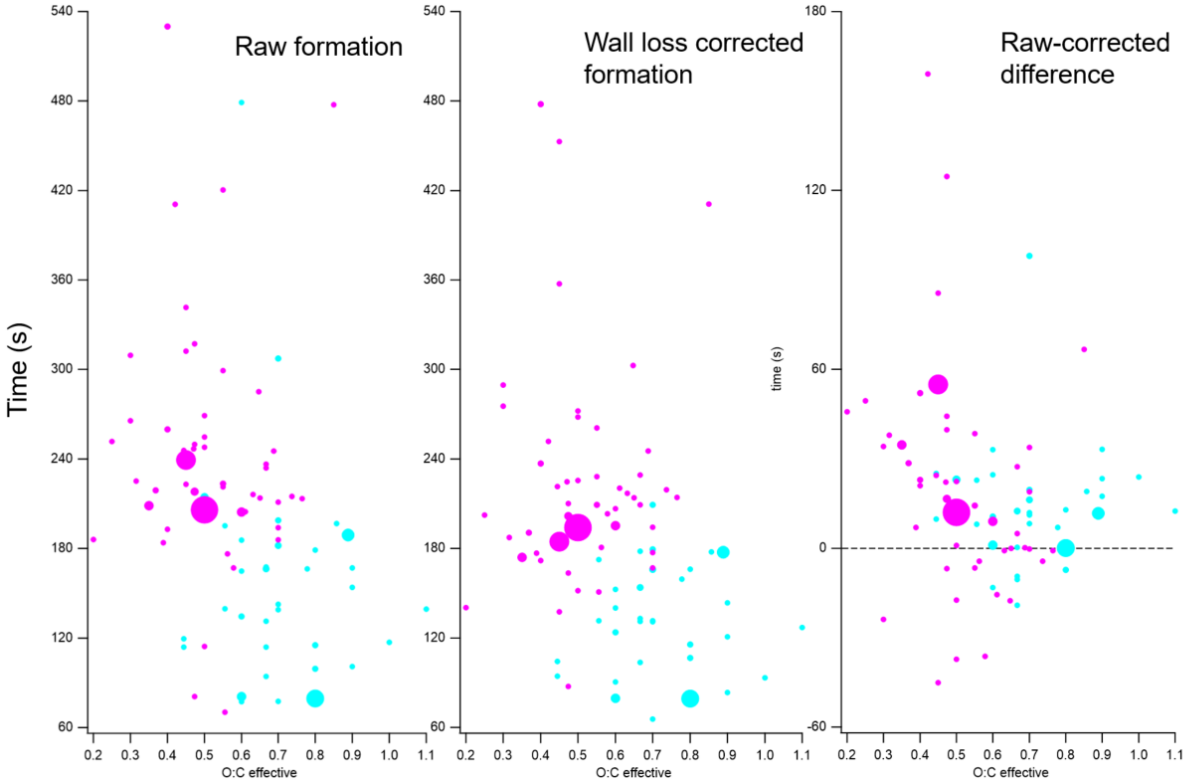

Figure 3.16: Speciated wall loss correction times for d-carene + NO_3 oxidation products plotted against O:C effective. Blue circles are monomer species and pink circles are dimer species. Note that the difference plot (right) has a different left axis than the other plots.

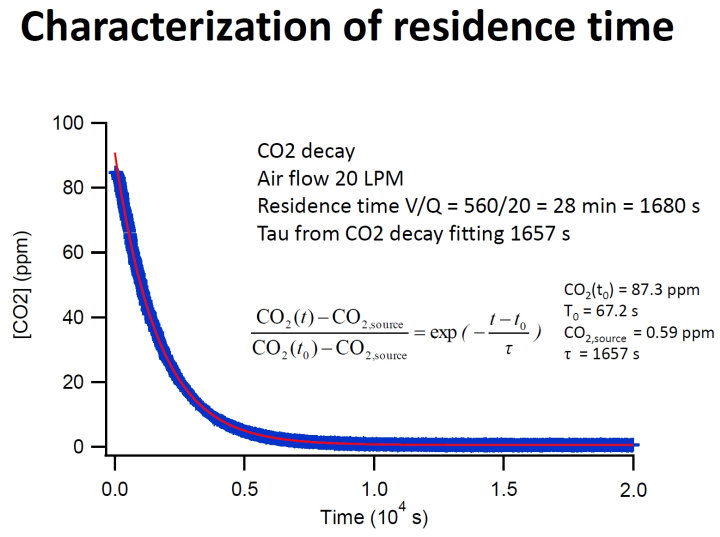

Figure 3.17: Comparison of experimentally determined residence time to that calculated assuming a well-mixed chamber.

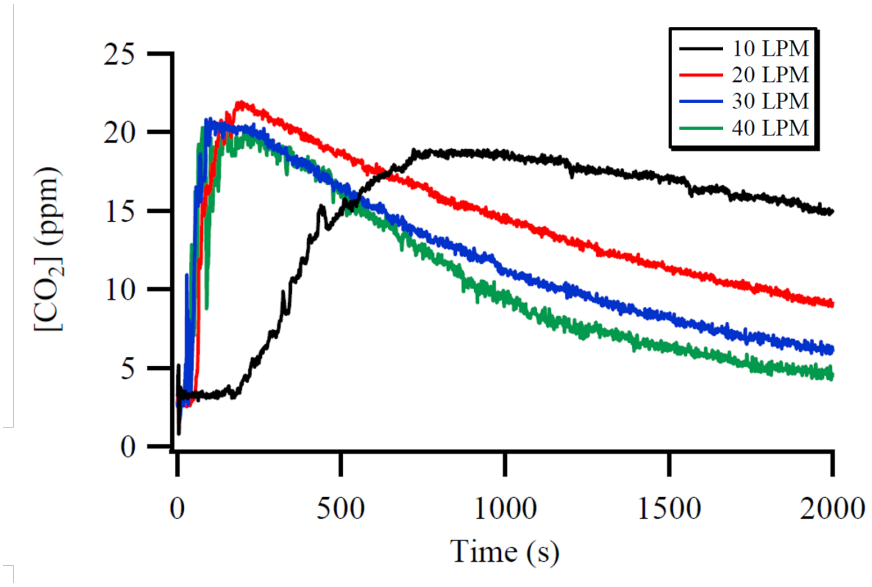

Figure 3.18: Measurements of $[CO_2]$ exiting chamber after a pulse of CO_2 was added at t=0.

3.6.7 β-pinene experiments comparison of results from high and low concentration

β-pinene + NO_3 experiments were done for two different concentrations of β-pinene, 8 and 80 ppb. Results from these experiments were averaged for comparison to the other MT systems, but raw results from each experiment are shown in this section (Figure 3.19). The mass spectra for these two experiments were very similar. Almost every major peak was present in both spectra. However, elemental ratios for each experiment show changes in every category, with major changes observed for fragmentation and oligomerization products (C number). About 10% more C_7 fragments and 10% less C_{10} species were observed for the high concentration experiments. Additionally, about 20% more C_{20} dimer products were observed for the high concentration experiments, while the low concentration dimer carbon number distribution was more spread out among the C_{17}, C_{19} and C_{20} peaks. Less drastic differences were observed for the other categories. Slightly more monomers (3%) than dimers and $C_{10}N_2$ than $C_{10}N_1$ products were formed in the low concentration experiment. Slightly more $C_{10}N_1H_{15}$ compounds than $C_{10}N_1H_{16}$ were measured for the high concentration experiment, as apposed to the low concentration experiment in which the H_{16} and H_{15} contributions are almost equal.

bpin products	low conc. (8 ppb)	high conc. (70 ppb)
monomers	62%	59%
dimers	38%	41%
C_7	22%	32%
C_9	8%	7%
C_{10}	70%	61%
C_{17}	27%	18%
C_{19}	24%	12%
C_{20}	49%	71%
N_0	1%	1%
N_1	80%	86%
N_2	19%	13%
H_{15}	46%	50%
H_{16}	47%	44%
H_{17}	7%	6%

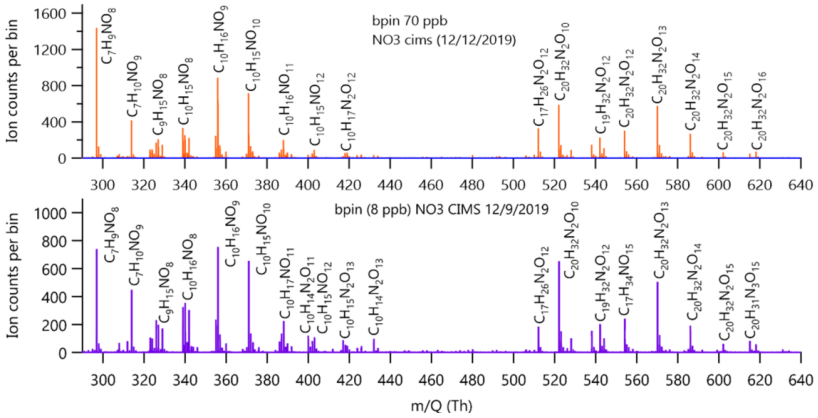

Figure 3.19: Comparison of elemental ratios and mass spectra for low concentration (8 ppb) and high concentration (70 ppb) bpin experiments.

Chapter 4

Formation of Highly Oxidized Organic Compounds and Secondary Organic Aerosol from a-Thujene Ozonolysis

4.1 Abstract

We conducted laboratory chamber experiments to probe the gas and particle phase composition of oxidized organics and secondary organic aerosol (SOA) formed from a-thujene ozonolysis under different chemical regimes. The formation of low-volatility compounds was observed using chemical ionization mass spectrometry with nitrate (NO_3^-) and iodide (I^-) reagent ions. The contribution of measured low-volatility compounds to particle growth was predicted using a simple condensational

Chapter 4 of this dissertation is a reprint of the material as it appears in: "Formation of Highly Oxidized Organic Compounds and Secondary Organic Aerosol from a-Thujene Ozonolysis" *J. Phys. Chem. A.* Accepted for publication. **2023**. https://doi.org/10.1021/acs.jpca.3c02584., used with permission from American Chemical Society Publications. The co-authors listed in this publication are Adam E. Thomas and James N. Smith.

growth model and found to underpredict the measured growth rates in our chamber (on the order of several nm min^{-1}). The yield of low-volatility compounds and SOA mass were similar to those of other monoterpene ozonolysis systems. While semi-volatile compounds $C_{10}H_{14\text{-}16}O_{3\text{-}7}$ were measured most abundantly with I^- reagent ion, a large fraction of products measured with NO_3^- were $C_{5\text{-}7}$ fragments with predicted intermediate volatility. Additionally, particle composition was measured with ultrahigh performance liquid chromatography with high resolution mass spectrometry and compared to particle composition from a-pinene ozonolysis. Structural isomers were identified from tandem mass spectrometry analysis of two abundant product ions ($C_8H_{13}O_5^-$,$C_{19}H_{27}O_7^-$). Our results indicate that although this system efficiently generates low-volatility organics and SOA under the conditions studied, fragmentation pathways that produce more highly volatile products effectively compete with these processes.

4.2 Introduction

Seconadary organic aerosol (SOA) is a major component of global aerosol particles in the atmosphere that can significantly influence climate and human health (Jimenez et al., 2009; Stocker et al., 2013a). Oxidized organics contributing to particle nucleation and growth are formed through oxidation of volatile organic compounds (VOCs) in the atmosphere to form oxidized organic products with reduced volatility that can partition to the particle phase (Ehn et al., 2014; Hallquist et al., 2009; Trostl et al., 2016; Barsanti et al., 2017; Bianchi et al., 2019; Kroll and Seinfeld, 2008). Monoterpenes are an important class of biogenic VOCs with the chemical formula $C_{10}H_{16}$. Monoterpenes are globally abundant (∼11% of global VOCs) (Sindelarova et al., 2014) and known to efficiently produce highly oxidized products from reactions with ozone (O_3), one of the major tropospheric oxidants. The gas-phase reaction products, SOA formation and composition from ozonolysis reactions for several monoterpenes have been well characterized in previous lab studies, particularly for cyclic monoterpenes, like α-pinene. Due to the effect of structure on the ozonolysis mechanism, cyclic monoterpenes are especially good precursors for SOA formation. Understanding the SOA formation

mechanism is an area of active study with a robust body of work (Molteni et al., 2019; Rissanen et al., 2015; Ziemann and Atkinson, 2012).

Figure 4.1 shows the initial steps in the ozonolysis of two monoterpenes: α-pinene and α-thujene. The primary ozonide that is formed from the initial addition of O_3 to the C=C double bond (R1) quickly decomposes to form an excited Criegee intermediate and a carbonyl group (R2), while cleaving the C-C bond. Cyclic compounds can preserve the size of the carbon backbone after fragmentation while allowing the addition of functional groups. This allows the overall volatility of the molecule to quickly decrease compared to acyclic compounds, for which the length of the carbon chain is not preserved after fragmentation. The Criegee intermediate can stabilize and go on to form aldehyde compounds, or undergo a hydrogen shift to form a vinyl hydroperoxide (R3), which then rapidly loses OH radical to form a vinoxy radical (R4). This vinoxy radical can then be oxidized by O_2, forming an RO_2 peroxy radical (R6) that can participate in many different reactions in the atmosphere (Zhao et al., 2018). It is suggested that autoxidation reactions are essential for the formation of low-volatility organics in the atmosphere (Crounse et al., 2013; Bianchi et al., 2019). These reactions are internal isomerization reactions in which peroxy radicals abstract hydrogen atoms from neighboring carbon atoms, creating new alkyl radical sites that can be oxidized by O_2 and continue propagation of radicals. For α-pinene, the steric strain caused by cyclobutyl ring greatly hinders the rate of autoxidation, therefore limiting subsequent functionalization and formation of low-volatility products (Vereecken and Peeters, 2012; Peeters et al., 2001; Kurtén et al., 2015). In a recent study, Iyer et al. found that radical rearrangement of the vinoxy alkyl radical, which opened the cyclobutal ring (R5), was competitive and allowed for rapid autoxidation reactions (Iyer et al., 2021).

In this study, we investigate the ozonolysis of α-thujene, a monoterpene with a 5-membered outer ring and a 3-membered inner ring. We predicted that the more strained 3-membered ring structure could more rapidly undergo ring opening reactions, allowing for increased efficiency in formation of unique low-volatility species in the gas phase and SOA compared to the ozonolysis of α-pinene (4-membered inner ring; ref. Figure 4.1). Similar ring-opening radical rearrangements from alkyl radicals in the alpha position to cyclopropyl rings have been shown to be competitive for other

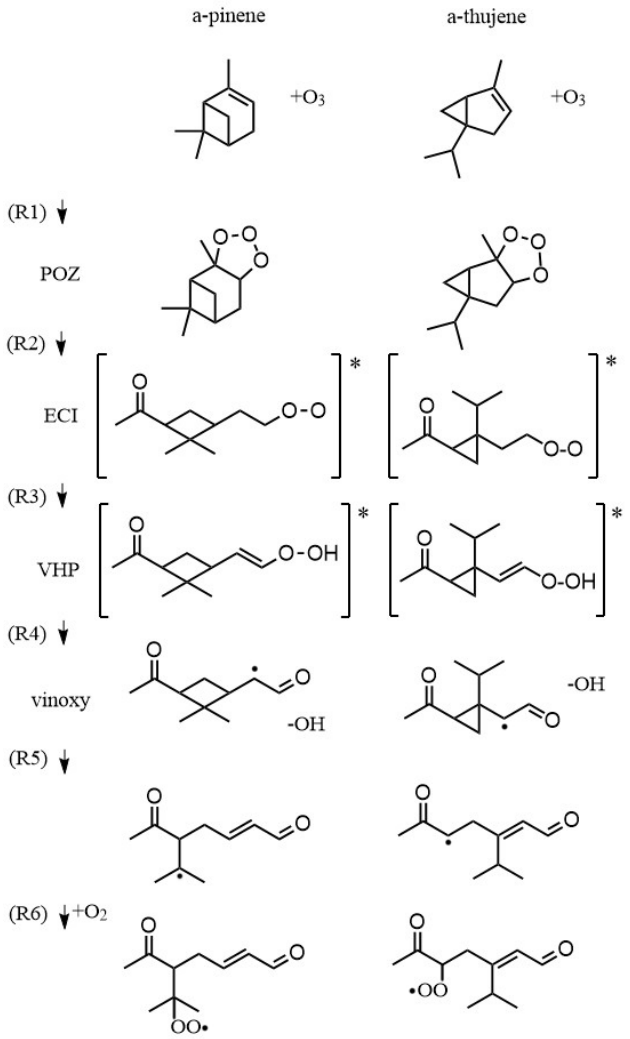

Figure 4.1: Simplified mechanism of α-pinene and α-thujene ozonolysis. Only one primary ozonide decomposition pathways is shown (R2). Additional alternative pathways for stabilized Criegee intermediates and vinoxy compounds are not shown.

monoterpene oxidation systems (Kurtén et al., 2017; Draper et al., 2019; Møller et al., 2020), and a recent study found enhanced SOA produced from ozonolysis of Δ-carene compared to α-pinene, two monoterpenes that are expected to undergo the same ozonolysis mechanism with the only difference being the size of the secondary ring (Thomsen et al., 2021). Additionally, following the mechanism suggested by Iyer et al., the resulting RO_2 molecules formed in step R6 (Figure 4.1) are structural isomers, which may lead to the availability of unique hydrogen shift pathways based on the location of the RO_2 functional groups on the carbon chains (Iyer et al., 2021). α-Thujene is emitted in small quantities by vegetation (Geron et al., 2000; Guenther, 2000), and is a major component of

essential oils used in perfumes, incense and other household products (de Almeida et al., 2014). One experimental study found that SOA was generated from ozonolysis of a mixture of monoterpenes containing α-thujene sampled from the head space of a cabbage under various MT:O_3 ratios (Pinto et al., 2007). To date, no studies exist that probe the detailed composition of gas-phase oxidized reaction products or SOA from α-thujene ozonolysis.

4.3 Methods

4.3.1 Experiment

The details of this experimental set up are similar to that described in Dam et al. (Dam et al., 2022) with a few key differences. For this experimental set up, we ran continuous flow experiments in a 560 L stainless steel chamber under dry conditions with a total flow of 20 lpm, resulting in a residence time of $\sim$28 min. Mixing inside the chamber was previously shown to be fast ($<$ 1 min) under these flow conditions (Dam et al., 2022). O_3 was generated by UV-photolysis of purified air and introduced to the chamber. After about 2 h, the concentration of O_3 stabilized (180 ppb) and α-thujene was added to the chamber from a prepared gas cylinder (18 ppm α-thujene in N_2). Commercial frankincense oil was fractionally distilled to obtain a high-purity liquid α-thujene (>90%), which was then injected into a gas cylinder and filled with ultra high purity nitrogen. The experimental details for purification of liquid α-thujene were previously discussed (Dam et al., 2022). The concentration of α-thujene added to the chamber was varied (13, 55, 113, 500 ppb) for each experiment. Hydroxyl radical (OH) scavengers (eg., CO) were not added for these experiments.

O_3 concentration was measured optically with a commercial absorption gas analyzer (2B Technologies, model 106-L). α-Thujene concentrations were monitored inside the chamber with gas chromatography (GC-FID, Agilent) coupled with a custom-built real-time thermal desorption inlet that employed a Tenax cartridge for efficiently trapping and desorbing monoterpenes. Particle number-size distributions were measured with a scanning mobility particle sizer (SMPS) using a differential

mobility analyzer (DMA, TSI model 3081) and condensation particle counter (CPC, TSI model 3020). The total scan time for one size distribution was 4 min and raw data were inverted using software written in the LabVIEW programming language (National Instruments Corp.).

Particle growth rates were calculated from measured size distributions by performing a linear fit on the maximum geometric mean diameters as the particles grew from 30 to 150 nm. Particle mass was calculated assuming an average density of 1.2 g cm^{-3}. This value is consistent with the range of densities reported for SOA formed from monoterpene oxidation (Nakao et al., 2013; Malloy et al., 2009). SOA mass yield was calculated by dividing the calculated particle mass by the α-thujene mass (ΔVOC) consumed during the experiments. GC-FID measurements of unreacted α-thujene in the chamber during the experiments were subtracted from modeled initial α-thujene concentrations calculated from the dilution of the known concentration of the α-thujene in the cylinder (Figure 4.7 in SI Sect. 4.6.2). For the 500 ppb experiment, GC-FID measurements were not available, so the calculated ratio of initial-to-unreacted α-thujene for the 113 ppb experiment was applied to the 500 ppb experiment. Therefore, this experiment is subject to greater uncertainty than the 55 ppb and 113 ppb experiments.

Gas phase composition was measured with a high resolution time-of-flight chemical ionization mass spectrometer (CIMS, Tofwerk AG, model LTOF) operated in negative ion mode with two reagent ions (NO_3^- and I^-). The inlet of the mass spectrometer consisted of a home-built transverse ionization source, which operated at atmospheric pressure as described previously (Li et al., 2019). NO_3^- ion was introduced by flowing high-purity N_2 gas (Airgas in Santa Ana, CA). over a glass reservoir containing nitric acid (HNO_3), and I^- ion was introduced by flowing N_2 gas through a stainless steel housing containing Teflon permeation tubes filled with liquid methyl iodide CH_3I. Mass spectra of gaseous products were processed with Tofware analysis software (Aerodyne Corp.) (Stark et al., 2015) using the reagent ions and associated oligomers for mass calibration (NO_3^-, $HNO_3NO_3^-$, $(HNO_3)_2NO_3^-$, I^-, I_2^-, I_3^-).

The composition of particles generated in these experiments was measured offline with ultra high performance liquid chromatography high resolution mass spectrometry (UHPLC-HRMS), employing

an Orbitrap mass analyzer (ThermoFisher model Q-Exactive Plus). Particles were collected at 3 lpm over the entirety of the experiments (∼2.5 hrs) onto PTFE membrane filters (0.5 um pore size, SKC), then extracted in acetonitrile. A shaker device (model 37600, Thermolyne) was used on the samples during the extraction process. This was done instead of sonication, as the latter has been shown to initiate chemical changes to organic species found in SOA (Miljevic et al., 2014). After extraction, the filters were removed and the filtrate liquid was reduced to ∼50 μL and reconstituted with water (∼50 μL) to reach a total sample volume of ∼100 μL. Samples were then injected into the UHPLC-HRMS system and analyzed in negative mode with heated electrospray ionization, producing hydrogen-abstracted (M^-) ions. Mass spectra were analyzed using FreeStyle version 1.8 (ThermoFisher) combined with home-built analysis programs for the analysis HRMS data, as reported previously (Baboomian et al., 2022; Smith et al., 2021; Nizkorodov et al., 2011). Additionally, tandem mass spectrometry (MS2) fragmentation spectra were obtained for several compounds to provide insights into molecular structure.

4.3.2 Modeling

We calculated the saturation concentrations (C*) of gas-phase reaction products measured with CIMS using the parameterization described in Mohr et al. (Mohr et al., 2019), which is a recent update building on the volatility basis set presented by Donahue et al. (Donahue et al., 2011). The contribution of the hydroperoxy functional group to volatility is considered by the Mohr parameterization, making it relevant for monoterpene oxidation systems, in which hydroperoxy compounds can be generated through various pathways (Jokinen et al., 2014; Iyer et al., 2017; Zhao et al., 2018).

A simple condensational growth model detailed in Ehn et al. was used to calculate the theoretical growth rates for each experiment (Ehn et al., 2014). Low, extremely low, and ultra-low volatility OC (LVOC, ELVOC and ULVOC, respectively) were treated as irreversibly condensing in the growth model, whereas semivolatile and intermediate-volatility VOC (SVOC and IVOC, respectively) were not considered. Additionally, we assumed a mass accommodation coefficient of 1 and made the same assumptions as in Ehn et al. (2014) for vapor mass (m_v) and density (ρv) (Ehn et al., 2014). For

the calculation of Knudsen number (Kn), the mean free path of air at 1 atm ($\lambda = 65$ nm) was used. The concentration of irreversibly condensing gases was calculated from NO_3^- CIMS measurements that were calibrated according to Kurten et al. and described in detail in Dam et al. (Kürten et al., 2012; Dam et al., 2022). Measured ion signals were converted to concentration and corrected for wall losses using the same wall loss rates (5.5 x 10^{-3} s^{-1} for monomers and 3.4 x 10^{-3} $s^{-}1$ for dimers) as in Dam et al. (2022), a study in which the same chamber with similar residence times was used. These loss rates are subject to uncertainty, as the compounds measured in that study were highly oxidized organonitrate compounds from monoterpene oxidation with NO_3 radical, not oxidized organics from monoterpene ozonolysis. Gas-phase species measured with I^- CIMS were not included in the growth model because the quantification of measured species is non-trivial and beyond the scope of this study (Lopez-Hilfiker et al., 2016b; Iyer et al., 2016; Bi et al., 2021). However, a rough estimation of product concentration measured with I-CIMS using a collision-limited ionization efficiency was performed and discussed in the context of the growth model in the Results section.

4.4 Results and Discussion

4.4.1 Gas Composition and Volatility Parameterization

A summary of the measurements performed in this study and associated results can be found in Table 4.1, with discussion to follow.

Figure 4.2A shows the percentage of parameterized reaction products in each volatility bin, for each experiment, over the course of the experiments. Table 4.2 shows a summary of the Log(C*) values for each volatility bin. The formation of LVOCs was measured with both I^- and NO_3^- CIMS for all experiments. Compounds with predicted Log(C*) values below -0.52 (LVOCs, ELVOCs and ULVOCs) are expected to partition irreversibly to the condensed phase, whereas SVOCs and IVOCs (Log(C*) values of -0.52 to 6.48 $\mu g/m^3$) are expected to reversibly partition.

Table 4.1: Summary of conducted experiments and results at one time point. The initial O_3 mixing ratios were 180 ppb for all experiments. Mixing ratios of α-thujene represent the value constantly being added to the chamber operated in continuous flow. Tabulated Δ-VOC concentrations were calculated before particle formation for experiments 2-4 and at 15 min for experiment 1, for which no nucleation was observed. Yields were calculated only for species measured with NO_3^- CIMS and include all LVOCs, ELVOCs and ULVOCs.

Expt	α-thujene (ppb)	Δ-VOC ($\mu g/m^3$)	L,EL,ULVOC yield %	SOA
1	13	72	0.3	no
2	55	84	5	yes
3	113	123	7	yes
4	500	390	0.8	yes

With NO_3^- CIMS, a larger contribution from ULVOCs (8-50%), ELVOCs (3-25%) was observed than with I^- CIMS (<3%). Additionally, the observed fractions of LVOCs (5-25%), SVOCs (10-45%) and IVOCs (10-62%) were also significant from species measured with NO_3^- CIMS. Figure 4.2B shows the time series of the total species within each volatility bin measured with NO_3^- CIMS for each MT:O_3 experimental condition. After parameterization, reaction products with specific chemical formulas fell into volatility bins that corresponded to their carbon chain lengths (Table 4.2). These chemical formulas can provide insight to the formation pathways represented in each case. IVOCs and SVOCs were found to be composed of C_5 and $C_{6\text{-}7}$ fragments, respectively. Fragment compounds can be formed from decomposition of a peroxy radical (RO_2) functional group to an alkoxy radical (RO) through bimolecular reactions with RO_2, HO_2, and NO. These alkoxy radicals can then form a carbonyl group by cleaving a carbon-carbon bond in the alpha position to the alkoxy carbon. This fragmentation mechanism produces one closed-shell product, and one product with an alkyl radical that likely bonds with molecular oxygen (O_2) in the atmosphere. The presence of these C_5 and C_6 fragments indicates that the double bond formed from the alkyl radical rearrangement shown in R6 (Figure 4.1) must have been oxidized in order to break those C-C bonds to form fragments with 5 or 6 carbon atoms. The dominant pathway for oxidizing this double bond is not currently elucidated, but Iyer et al., proposed that a 6-membered endoperoxide species forms quickly after the formation of the RO_2 radical (Iyer et al., 2021). This endoperoxide can add O_2 and continue to propagate. In addition to this, there is the potential for OH radical formed with the vinoxy radical (R4, Figure 4.1) to attack one of the carbon atoms in the double bond. ELVOCs and LVOCs were

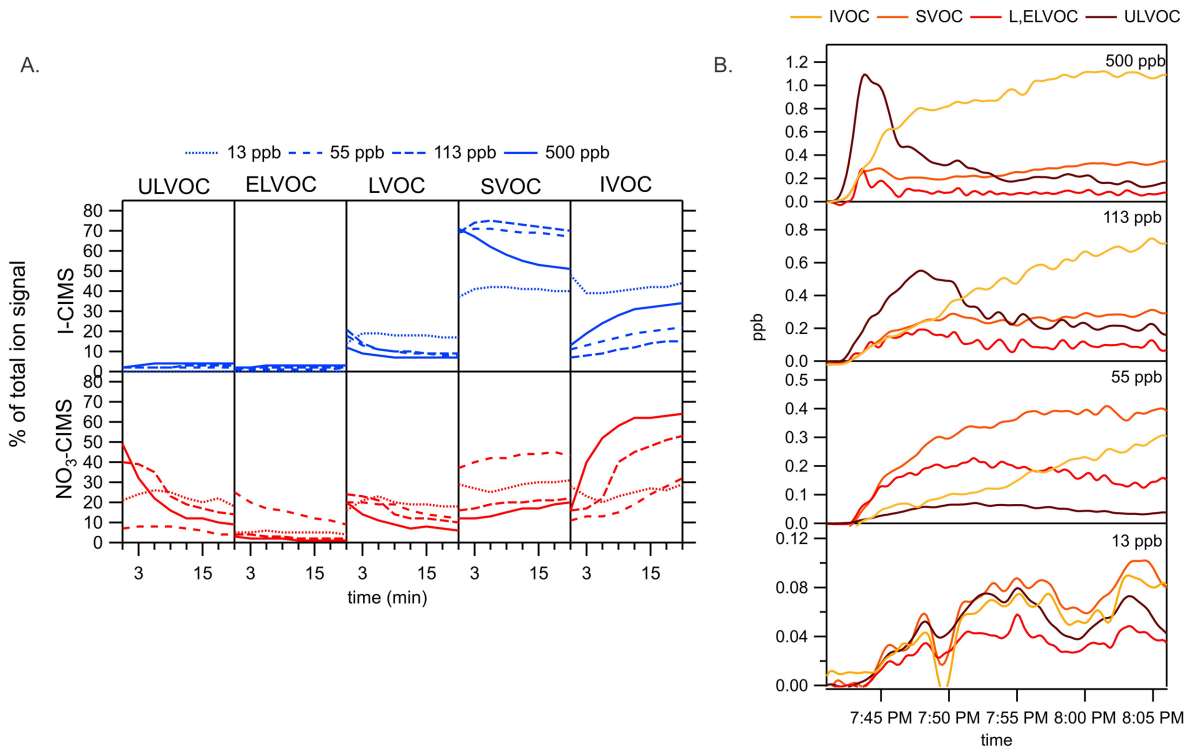

Figure 4.2: A. Time series of percentages of parameterized species measured with I^- CIMS (top) and NO_3^- CIMS (bottom) for all experiments. Percentages are taken over the total organic signal for both reagent ions. B. Concentrations of parameterized species measured with NO_3^- CIMS for each experiment.

primarily attributed to highly oxidized C_{10} species, with a small contribution from highly oxidized C_9 compounds. The formation of these species are attributed to autoxidation reactions, thus increasing the overall oxygen-to-carbon ratio of the parent molecules. Measured ULVOCs were composed of oligomer species ($C_{17\text{-}20}$) through RO_2+RO_2 reactions, producing organic peroxides (ROOR) and O_2. The reaction rates and mechanisms for these accretion reactions are not well understood and are an active area of current research.

Overall, highly oxidized compounds and a large number of oligomer compounds were measured with NO_3^- CIMS, whereas less highly oxidized compounds were measured with I^- CIMS (Figure 4.3A). These observations were consistent with the selectivity of each reagent ion reported in previous studies (Riva et al., 2019b; Hyttinen et al., 2021; Lee et al., 2014; Hyttinen et al., 2015; Krechmer et al., 2015; Isaacman-VanWertz et al., 2018; Iyer et al., 2017), although I^- CIMS has been used to measure oligomer compounds (Zhao et al., 2018).

Table 4.2: Log(C*) cut offs for each volatility bin, adapted from Donahue et al., with associated compound classes from this study. The most abundant compound measured with NO_3^- CIMS in each represented class is also shown with the reagent ion (NO_3^-) removed from the molecular formula.

Volatility Bin	Log(C*) ug/m^3	Represented Compounds	Most abundant compound
ULVOC	-8.52>	oligomers (C_{17-20})	$C_{20}H_{32}O_9$
ELVOC	-8.52 to -3.52	highly oxygenated ($C_{9,10}$)	$C_{10}H_{16}O_{10}$
LVOC	-3.52 to -0.52	highly oxygenated ($C_{9,10}$)	$C_{10}H_{14}O_6$
SVOC	-0.52 to 2.47	fragments ($C_{6,7}$)	$C_7H_8O_8$
IVOC	2.47 to 6.48	fragments ($C_{4,5}$)	$C_5H_6O_6$

The major peaks observed with NO_3 CIMS in the monomer region were dominated by fragment compounds, and the distribution of these compounds changed as the monoterpene-to-O_3 ratio (MT:O_3) was increased (Figure 4.3B). The compound with the molecular formula $C_5H_6O_6$ (m/z 162) became the dominant species when MT:O_3 was the highest, whereas the $C_7H_8O_8$ (m/z 220) compound was the most abundant at the lowest MT:O_3. C_5 compounds were predicted to be IVOCs, but the other fragments were predicted to be SVOC ($C_{6,7}$) and LVOC (C_8) compounds. Therefore, it is possible that we are observing condensation of the SVOC and LVOC fragments out-competing formation processes within the first 20 min of the experiment as MT:O_3 increases and observed particle surface area increases. To our knowledge, no other studies have reported the formation of these fragment compounds as the major products of monoterpene ozonolysis reactions. Most laboratory studies using NO_3^- CIMS to probe highly oxidized organics formed from monoterpene ozonolysis report oxidized C_{10} species and C_9 species as major products (Jokinen et al., 2014; Riva et al., 2019b; Ehn et al., 2014; Li et al., 2019; Mentel et al., 2015; Claflin and Ziemann, 2018; Ehn et al., 2012). One study (Li et al., 2019) measured $C_5H_6O_6$ as a minor product of α-pinene ozonolysis, but still found that oxidized C_{10} species were most abundantly produced.

Additionally, modulating MT:O_3 had several other effects on the measured distribution of reaction products (Figure 4.2). When the α-thujene mixing ratio was 13 ppb, the formation of products from every volatility bin was similarly fast, and thus all available formation pathways were competitive. An increase from 13 to 55 ppb seemed to drive the formation of ELVOCs, LVOCs and SVOCs, which correspond to an increase in autoxidation and fragmentation reactions. Further increasing

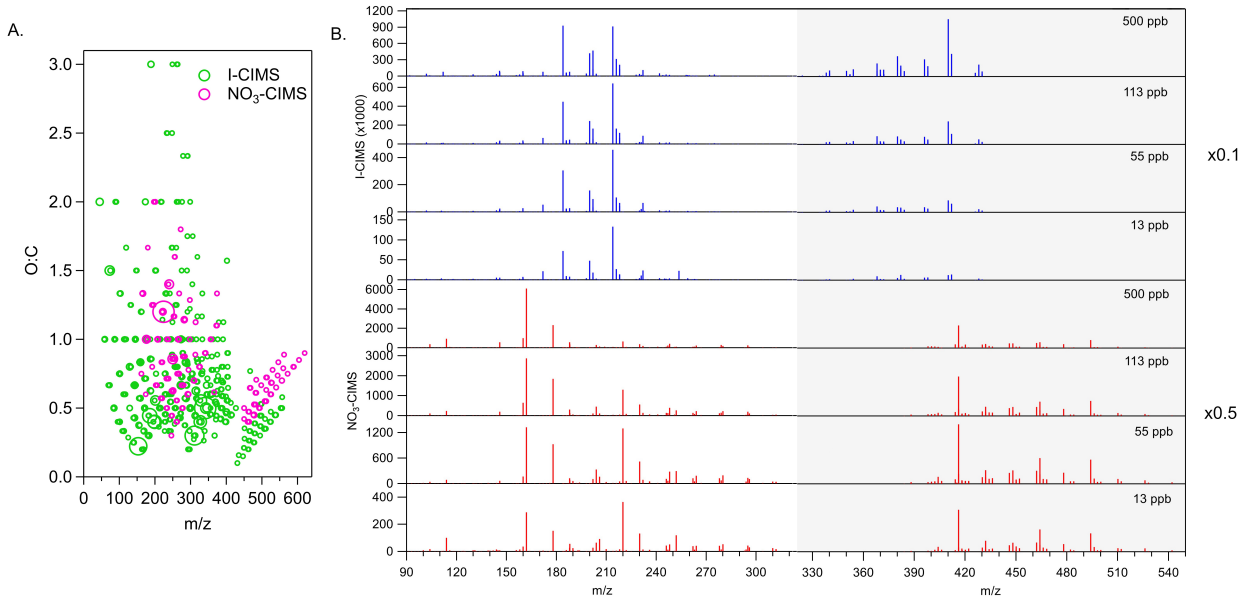

Figure 4.3: A. Oxygen-to-carbon ratios plotted against mass-to-charge ratio for compounds measured with I^- CIMS (green) and NO_3^- CIMS. Two oxygen atoms were subtracted for every nitrate group. Marker areas are weighted by intensity of compounds, but are not comparable between reagent ions. The right axes indicate the intensity for compounds within the shaded region and are scaled to the left axes. B. Mass spectra for species measured with I^- CIMS (top) and NO_3^- CIMS (bottom) for each experiment, averaged over the first 20 min of the experiment. Intensity is plotted against mass-to-charge ratio with reagent ion masses removed: NO_3^- (m/z 62), I^- (m/z 127). Monomers and dimers are plotted against the left axis, but dimer species (shaded region) were scaled up for plotting and need to be multiplied by the factor on the right to represent the original intensities.

the α-thujene concentration to 113 and 500 ppb dramatically increased the initial production of ULVOC oligomers relative to all other classes of compounds. However, these ULVOCs rapidly condense onto growing particles, so the ratio of observed dimers-to-monomers decreases as MT:O_3 increases over the course of the experiments (Figure 4.8 in SI Sect. 4.6.3). When the α-thujene concentration is 13 ppb, the dimer compounds make up roughly 25% of the overall signal after the experiment proceeded for 20 min. At 500 ppb, the dimer compounds make up less than 2%. In the dimer region, the product distribution is relatively stable between the various MT:O_3 experiments. However, the ratios of several compounds ($C_{20}H_{30}O_{9-11}$, m/z 414, 430, 446) relative to the total dimer concentration are shown to increase slightly with increasing MT:O_3. This indicates the formation of these C_{20} dimers is faster than loss to condensation in the chamber. The ratio of one

compound ($C_{19}H_{28}O_{13}$, m/z 464) seems to decrease slightly with increasing MT:O_3, indicating more rapid condensation than formation.

In comparison to measurements with NO_3^- CIMS, SVOCs were most abundantly measured with I^- CIMS (40-70%). Smaller contributions from IVOCs (10-40%) and LVOCs (10-20%) were also observed (Figure 4.2A). The fraction of SVOC compounds produced increased by increasing the α-thujene concentration from 13 to 113 ppb, but decreased at 500 ppb. This is likely due to a larger increase in condensation than SVOC production as particles rapidly formed and grew under the highest α-thujene concentration condition. Conversely, the fraction of IVOCs produced decreased with increasing α-thujene concentration from 13 to 113 ppb, but increased at 500 ppb.

Using I^- CIMS, the major peaks observed in the monomer region were mostly oxidized $C_{10}H_{14,16}O_{3\text{-}5}$ parent compounds with some smaller contributions from large fragments (C_8,C_9). The most notable difference in observed product distribution as MT:O_3 was increased was the increase of the $C_{10}H_{16}O_3$ (m/z 184) and $C_9H_{14}O_5$ (m/z 202) compounds. Both compounds were predicted to be SVOCs, and therefore, we believe the formation of these compounds is being driven faster than condensation as MT:O_3 increases. The dimer signal measured with I^- CIMS was about two orders of magnitude less than the monomer signal. Additionally, the ratio of dimers-to-monomers increases as MT:O_3 increases (Figure 4.8 in SI Sect. 4.6.3), indicating that formation of observed products was driven by the increase in MT:O_3 ratio. The increased ratio of the $C_{20}H_{26}O_9$ (m/z 410) compound was the major observed effect of increasing MT:O_3.

It is important to note that because OH scavengers were not used for these studies, the effect of modulating MT:O_3 on measured reaction products is likely initiated by OH radical oxidation in conjunction with ozonolysis. The relative contribution from each oxidant cannot be easily allocated, as oxidation rate constants have not been previously measured for this monoterpene system.

Additionally, the selectivity of the reagent ions is expressed in the measured mass spectra. Only ions suspected to be clustered with reagent ions (M + NO_3^- or M + I^-) were considered for analysis, although hydrogen abstracted (M^-) ions are known to be produced by ionization with both reagent ions. This allows quantification of species measured with NO_3^- CIMS to be valid, as we assume

the nitrate reagent ion forms clusters with oxidized organics with the same efficiency as it reacts with sulfuric acid (i.e., at the collision rate) (Kürten et al., 2012). This assumption inherently introduces uncertainty, but is a common method of estimating the upper limit of measured oxidized organics. The other advantage of analyzing only M-NO_3^- and M-I^- species is that we can have greater confidence that measured species were not fragmented by ionization (Ehn et al., 2012; Iyer et al., 2016). Additionally, an important limitation of using iodide as a reagent ion is the interference of secondary ion chemistry. In the presence of O_3, the I^- ion can undergo secondary ion chemistry, forming iodide oxyanions (IO^-, IO_2^-, IO_3^-) that can cluster with oxidized organic compounds (Zhang and Zhang, 2021; Dorich et al., 2021). This is a source of uncertainty in the molecular formula assignment of oxidized organics with I^- CIMS, but is not considered for our study, for which we assume all oxygen atoms measured with I^- CIMS are attributed to oxidized organic compounds.

4.4.2 Particle Composition

The mass spectrum measured with UHPLC-HRMS is shown in Figure 4.4A for the 500 ppb α-thujene experiment. No unique chemical formula were observed when MT:O_3 was changed, so only the most intense mass spectrum is shown. Fragment compounds ($C_{7\text{-}9}$) comprised over half of the overall signal measured from the particle phase, with C_9 compounds particularly abundant (∼30%). The $C_9H_{13}O_4^-$ compound was most abundant, making up 17% of the overall signal intensity. We assume this compound is the α-thujene analog to pinic acid. In the oligomer region, the majority of measured signal was from C_{17} and C_{19} dimers. It is important to note the degree to which our measurements are influenced by the sensitivity of the technique. Likely, the oligomer compounds are over-expressed with this method, as shown by previous work (Kenseth et al., 2020). Additionally electrospray ionization is generally selective towards compounds with acid functional groups. For monoterpene oxidation systems, we assume most of these to be carboxylic acid functional groups.

MS2 spectra are shown in Figure 4.4B for two species with assigned molecular formula ($C_8H_{13}O_5^-$, $C_{19}H_{27}O_7^-$) from SOA generated during separate α-thujene ozonolysis and α-pinene ozonolysis

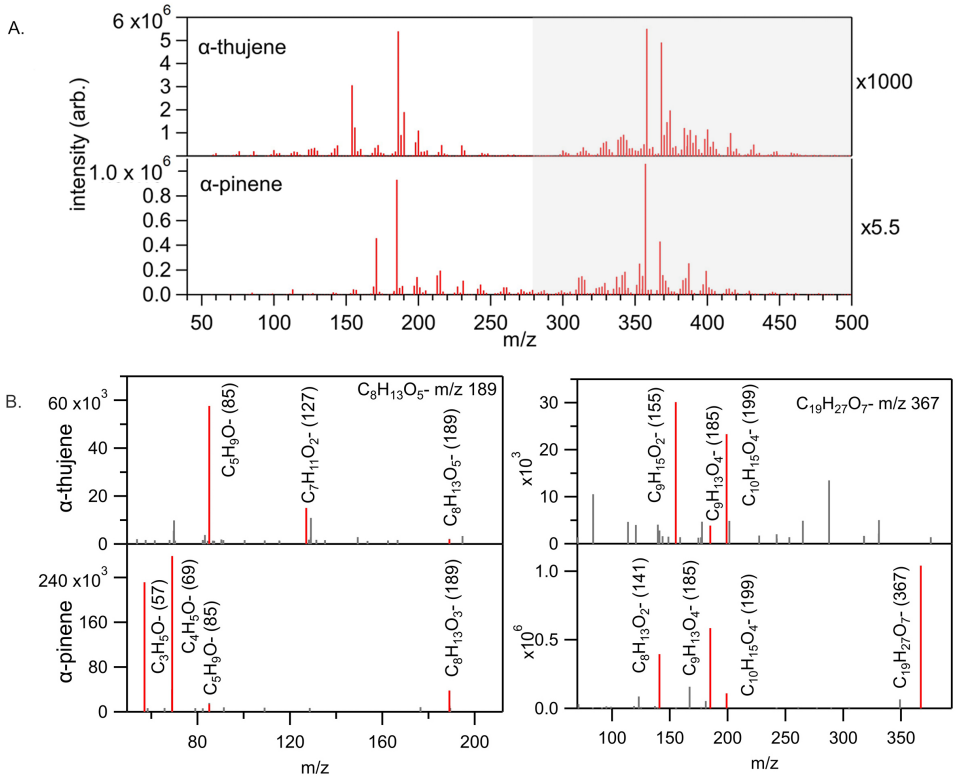

Figure 4.4: A. Mass spectrum of SOA from the 500 ppb α-thujene experiment and separate α-pinene experiment analyzed with UHPLC-HRMS. Both monomer and dimer compounds are plotted against the left axis, but the intensities of dimer compounds ($>$ m/z 270) were scaled down and should be multiplied by the factors on the right to represent the original intensities. Both left and right axes have arbitrary units of intensity with right axes scaled to left axes. B. MS2 spectra for two species with the same molecular formula identified in SOA from α-thujene ozonolysis (top) α-pinene ozonolysis (bottom). Assigned species in the MS2 spectra are red and labeled with the molecular formula and m/z, while unassigned species are grey and unlabeled.

experiments, but analyzed with the same method. These compounds comprised 4% and 2% of overall signal intensity for the α-thujene system, respectively, and 2% and 2% for the α-pinene system. The conditions under which α-pinene ozonolysis SOA was generated were comparable to the α-thujene ozonolysis experiments performed for this study (dry and without OH scavenger). Details of the α-pinene ozonolysis experiment and comparison of Van Krevelen plots can be found in the Supporting Information (Section 4.6.4). The observed MS2 spectra show different fragmentation patterns for measured compounds with the same assigned molecular formula for these different systems. For the $C_8H_{13}O_5^-$ compound, $C_7H_{11}O_2^-$ was a unique fragment peak observed for α-

thujene SOA that corresponds to a loss of a CH_2O_3 species, which could be attributed to carbonic acid or performic acid as leaving groups. Observed $C_3H_5O^-$ and $C_4H_5O^-$ fragments were unique to the α-pinene SOA. A shared compound was $C_5H_9O^-$, although its intensity was much higher relative to other peaks in the α-thujene MS2 spectrum. This fragment corresponds to a loss of $C_3H_4O_4$, which can likely be attributed to an C3 alkyl chain containing two carbonyl groups. Additionally, a small contribution from the parent peak was observed for both systems. For the $C_{19}H_{27}O_7^-$ compound, similar fragment peaks ($C_9H_{13}O_4^-$,$C_{10}H_{15}O_4^-$) were observed in the MS2 spectra, but with different ratios relative to other peaks. A $C_9H_{15}O_2^-$ fragment was observed for only the α-thujene system, whereas $C_8H_{13}O_2^-$ was observed only for the α-pinene system. Also, a large parent peak was measured for the α-pinene system, while no parent peak was measured for the α-thujene system. These differences in observed fragmentation species in the MS2 spectra indicate, generally, that structural isomers were found in the SOA composition of these two monoterpene ozonoylsis systems. The presence of these isomers imply that oxidation and other chemical processes these compounds undergo in the gas and/or particle phase are unique.

4.4.3 Particle Mass Yield and Growth Rate

Figure 4.5A shows the measured particle growth rates in our laboratory chamber. No nucleation and subsequent growth was observed when α-thujene mixing ratio was 13 ppb, even though LVOCs were generated in high abundance. It is likely that these low volatility compounds were lost to chamber walls and removed from the chamber faster than nucleation could occur. At 55, 113 and 500 ppb, nucleation was observed and the measured growth rates increased from 2.0 nm min^{-1} to 3.4 nm min^{-1} as α-thujene mixing ratio increased. These growth rates are very fast relative to those observed in the ambient atmosphere (nm min^{-1} vs. nm h^{-1}), but consistent with other reported laboratory studies of monoterpene oxidation systems (Zhao et al., 2015).

Our modeled growth rates under-predict the experimentally measured growth rates by a a factor of 1.5 to 5. Only the contribution of LVOCs, ELVOCs and ULVOCs were considered for the theoretical growth rate calculation, therefore, the reversible partitioning of SVOCs and IVOCs is not taken into

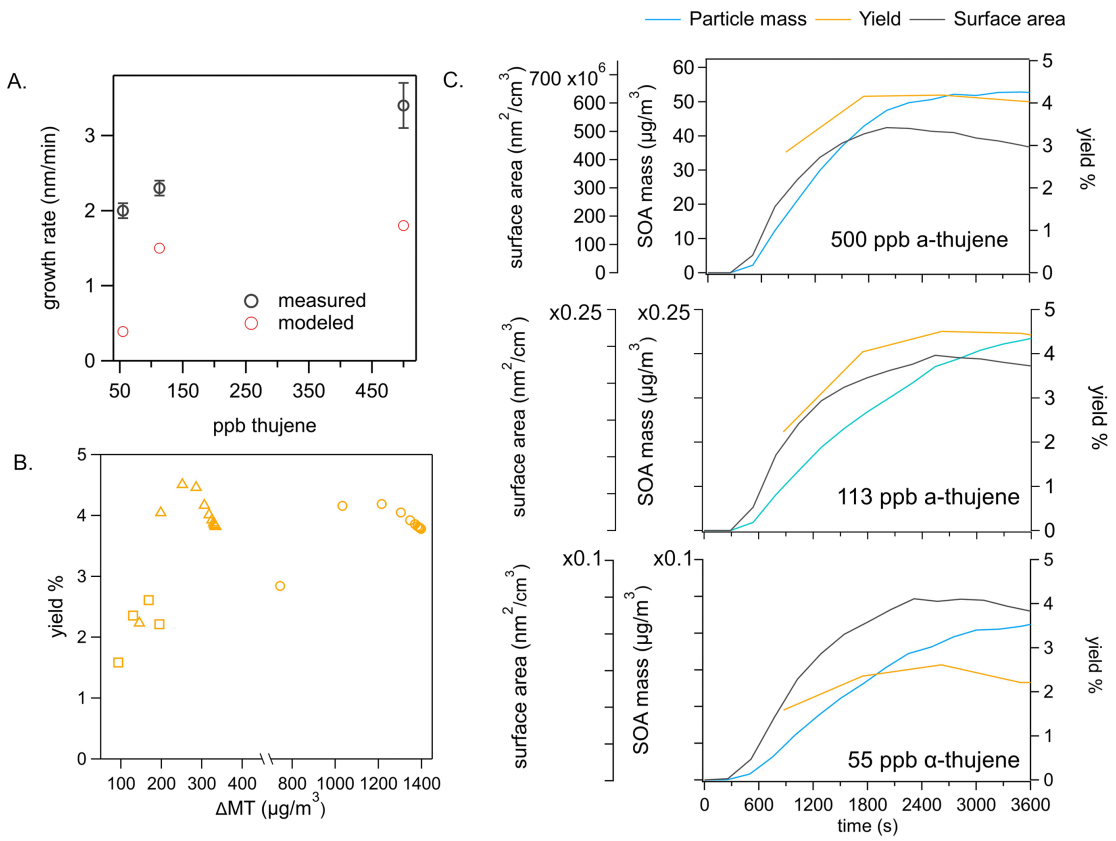

Figure 4.5: A. Measured and modeled growth rates for each experiment. Error bars for measured growth rates represent the uncertainty of the fitted geometric mean diameters. B. Particle mass yield plotted against α-thujene mass concentration consumed during the experiments (Δ-MT). Square, triangle and circle markers represent the 55 ppb, 113 ppb and 500 ppb α-thujene experiments, respectively. C. Time series of surface area, mass concentration of particles (left axes), and percent yield are shown for each experiment. The 55 ppb and 113 ppb left axes are scaled to the 500 ppb left axes.

account and may help to explain the discrepancy between measured and modeled growth rates. The experiment with the largest gap between measured and modeled growth rates was the 55 ppb α-thujene experiment. For this experiment, more than double the fraction of total measured reaction products were SVOCs (40%) compared to the 113 ppb (20%) and 500 ppb experiments (15%). Additionally, since the growth rate is scaled linearly with LVOC concentration, the concentration of LVOCs would need to be increased by a factor of 5 for the modeled growth rate to agree with the experimental growth rate for the 55 ppb experiment. For the 113 ppb and 500 ppb experiments, this factor needs to be close to 2. This means that SVOC and IVOC compounds need to be present in concentrations higher than these factors, as they are not assumed to irreversibly condense. A

crude estimate of the concentration of SVOCs measured with I^- CIMS using a collision-limit value (3.35 x 10^6 ppt cps[I-]/cps) calculated from the response of the instrument to N_2O_5 results in an SVOC concentration of ∼10 times greater than the L,EL,ULVOC concentration measured with NO_3^- CIMS for the 55 ppb experiment after 5 minutes from starting the experiment. This is an upper limit estimate and is subject to high uncertainty, but assuming half of the SVOCs measured with I^- CIMS are contributing to particle mass is enough to close the gap in modeled and measured growth rates. This provides qualitative evidence for the importance of SVOCs and IVOCs in accounting for particle growth.

The SOA mass yield was found to be 2% to 4% with SOA mass increasing from 100 to 1400 μg m^{-3}, respectively. We estimate an uncertainty of about 10% in our mass calculation in accordance with other studies (Shilling et al., 2008; Thomsen et al., 2021; Claflin and Ziemann, 2018; Xavier et al., 2019). For the 55 ppb experiment, we observed a maximum yield around 2%. For both the 113 ppb and 500 ppb α-thujene experiments, the maximum observed yield was around 4%. At a mass loading of 350 μg m^{-3}, the maximum SOA yield for α-pinene ozonolysis systems summarized in Shilling, et al. is around 30%(Shilling et al., 2008). Therefore, the SOA mass yields measured for these experiments are a factor of approximately 5-15 smaller than those reported for various α-pinene ozonolysis. This finding is consistent with our observation of SVOC and IVOC fragment compounds as large fractions of measured oxidation products.

4.5 Conclusions

We measured ozonolysis of α-thujene in a laboratory chamber to assess the potential formation of unique highly oxidized, low volatility products in the gas phase and subsequent nucleation and growth of SOA. Nucleation and growth were observed for every experimental condition except for the lowest MT:O_3 experiment. Measured growth rates were fast in our chamber (nm min^{-1}), but were consistently under-predicted by our simple condensational growth model which does not include the

reversible partitioning of semi-volatile compounds, which were produced in large abundance and measured with CIMS.

We measured gas composition using CIMS with nitrate and iodide reagent ions, which are selective towards highly oxidized organics and less highly oxidized organics, respectively. The volatilities of observed reaction products were estimated based on measured molecular formulas. As we varied the MT:O_3, we measured the production of LVOCs with both NO_3^- CIMS and I^- CIMS for all experimental conditions performed in this study. Oxidized parent compounds ($C_{10}H_{14\text{-}16}O_{3\text{-}7}$) dominated the I^- CIMS spectra, while the product distribution measured with NO_3^- CIMS was more varied with dimers, highly oxidized C_{10} compounds and small fragments (C_{5-7}) all significantly produced. After reaching an MT:O_3 over 1:2, increasing α-thujene mixing ratio ultimately increased the production of ultra low volatility dimers. However, these dimers partitioned more quickly to particles than they were produced, while intermediate and semi-volatile fragment products were produced faster than they condensed. Therefore, these fragment compounds were the major gas products at low MT:O_3 and after particle growth. In addition to gas composition, particle composition was measured offline using UHPLC-HRMS. The major species measured were large $C_{8,9}$ fragment compounds and oligomers. Comparing MS2 spectra for α-thujene ozonolysis SOA to α-pinene ozonolysis SOA revealed the presence of structural isomers in the particle phase.

The results of this study indicate that although the α-thujene ozonolysis system can produce high yields of low-volatility compounds, competitive fragmentation pathways exist under the represented chemical regimes that increase the volatility of the overall distribution of gas reaction products. Observed SOA yield for these studies were up to a factor of 15 smaller than those reported for α-pinene ozonolysis systems for comparable mass loadings. Although these fragmentation pathways were dominant in these studies, more studies need to be conducted in order to assess the relevance of these pathways in different chemical regimes, in which unimolecular and bimolecular peroxy radical reactions will vary. Future studies probing specific oxidation chemistry from O_3 and OH will help narrow down the driving forces behind the observed fragmentation.

4.6 Supporting Information

4.6.1 Particle size distributions

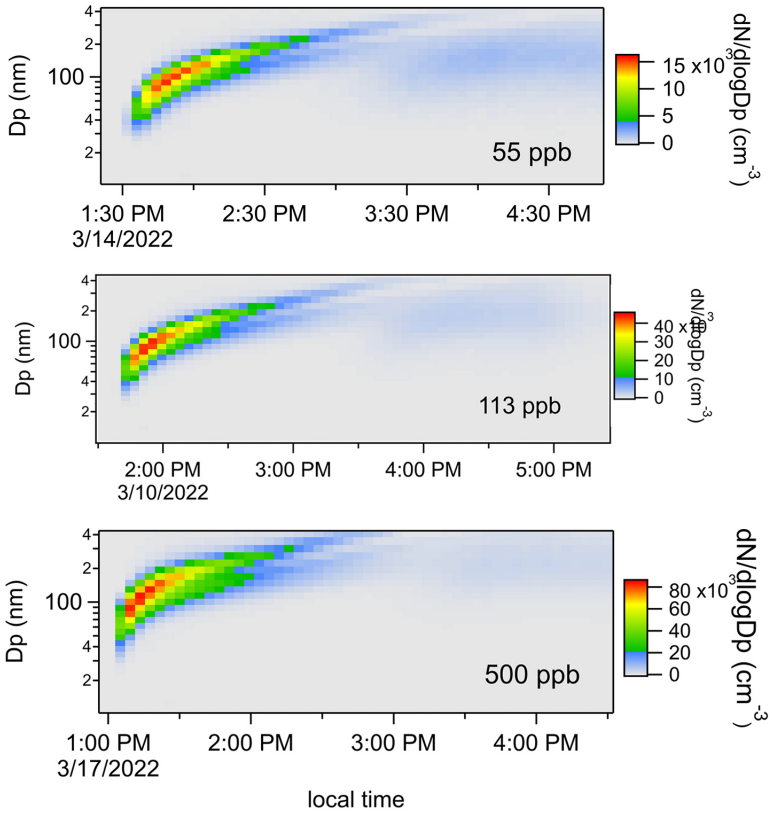

Figure 4.6: Measured particle size distributions for every experiment (55, 113 and 500 ppb α-thujene, 180 ppb ozone) except the 13 ppb α-thujene experiment, in which no particles were formed.

4.6.2 Measurement and modeling of α-thujene

Experimentally measured concentrations of O_3 and α-thujene were used to constrain the outputs a simple kinetic model that simulates dilution in our laboratory chamber and implements a rate constant tuned for α-thujene ozonolysis. Modeled residual α-thujene concentration was subtracted from modeled initial α-thujene concentration to calculate the amount of α-thujene reacted (ΔVOC)

during the experiment. Initial α-thujene concentration was calculated from the dilution of 13, 55, 113 and 500 ccm into 18 lpm for an 18 ppm α-thujene cylinder. For the 13 ppb α-thujene experiment, no residual α-thujene was measured in the chamber. Therefore, no data is shown. The residual α-thujene concentrations for the 55 ppb and 113 ppb experiments were constrained by GC-FID measurements. The ratio of residual to initial α-thujene from the 113 ppb α-thujene experiment was multiplied the modeled initial α-thujene trace from the 500 ppb experiment to generate a modeled residual α-thujene trace, as no GC-FID measurements are available for this experiment.

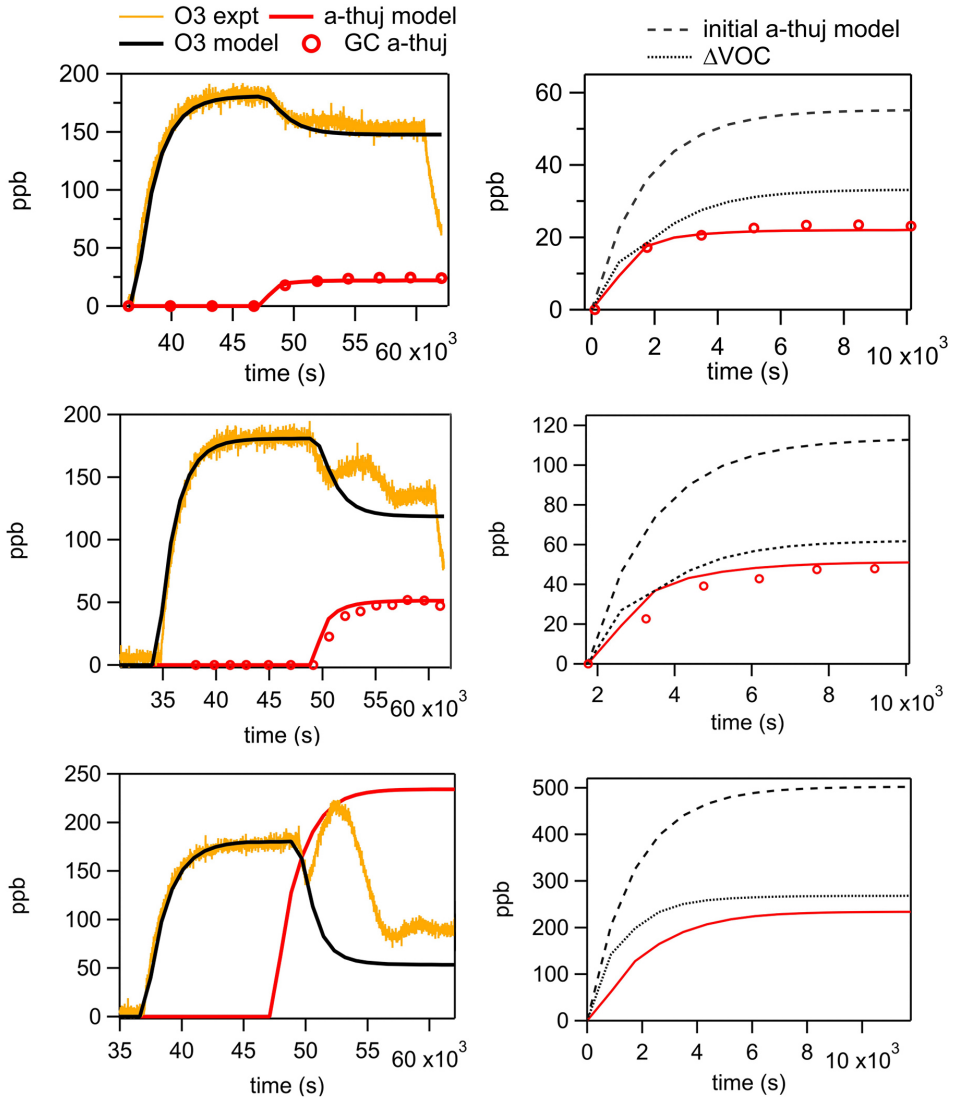

Figure 4.7: Experimentally measured O_3 and α-thujene concentration plotted with modeled concentrations against experiment time (left) for the 55, 113 and 500 ppb α-thujene experiments (top to bottom). The modeled initial and residual α-thujene concentrations and (Δ-VOC) is plotted against modeled experiment time (right).

4.6.3 Ratios of measured reaction products from nitrate and iodide chemical ionization mass spectrometry

The ratio of monomers to dimers was weighted by intensity and averaged over the first 20 minutes of the experiment. The ratio was relatively steady while increasing α-thujene for products measured with NO_3-CIMS, until the 500 ppb α-thujene experiment, in which the monomer to dimer ratio increased greatly (Figure 4.8A in SI Sect. 4.6.3). For the products measured with I-CIMS, the monomer to dimer ratio decreased with increasing α-thujene. Additionally, unratioed intensity of measured dimers increased with increasing α-thujene for compounds measured with either reagent ion (Figure 4.8B in SI Sect. 4.6.3), despite the ratio of of dimers to monomers remaining steady or decreasing for the NO_3-CIMS measurements.

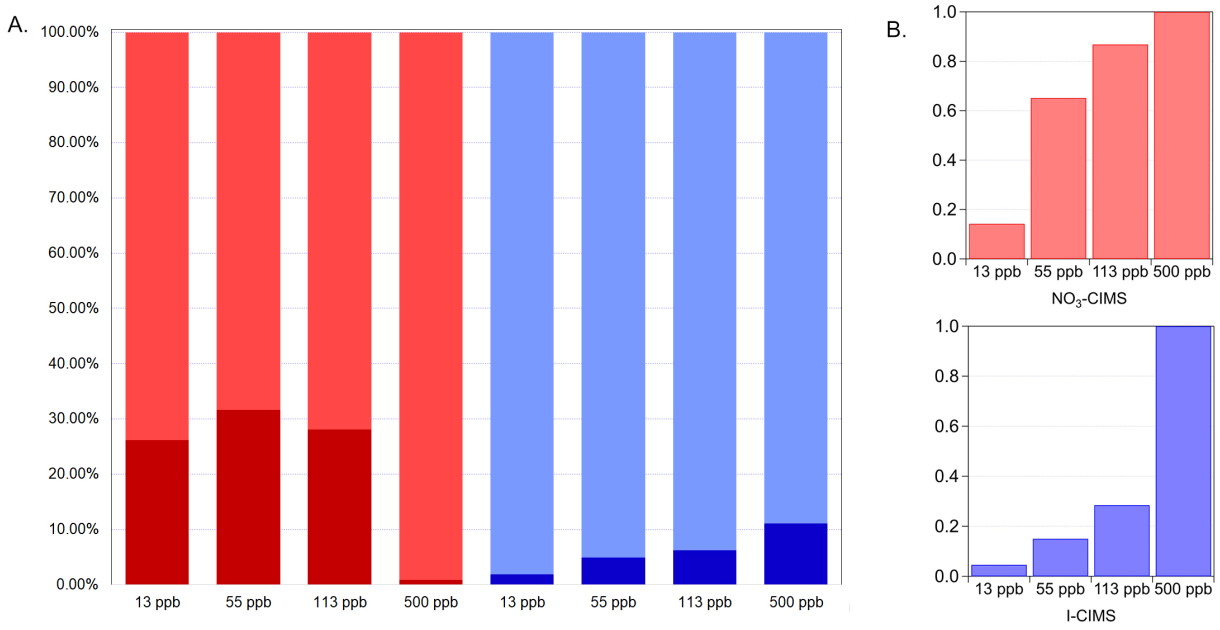

Figure 4.8: A. Ratio of intensity (arbitrary units) of monomers (light colored) and dimers (dark colored) for species measured with nitrate (red) and iodide (blue) CIMS for experiments with varying α-thujene mixing ratios (bottom). Intensities were averaged over the first 20 minutes of the experiments. B. Intensity of dimer species scaled to the intensity of the 500 ppb experiments, in which the highest intensities were measured.

4.6.4 α-pinene ozonolysis experiment

SOA was generated under dry conditions from the dark ozonolysis of α-pinene in a glass flow tube with a residence time of about one minute. A mixing ratio of $\sim$1 ppm of O_3 was generated by UV photolysis of purified air and added to the flow tube before addition of α-pinene, which was sampled by flowing nitrogen gas over the head space of liquid (+) α-pinene (98% purity, sigma-aldrich). No OH scavengers compounds were added to the flow tube. Particles were collected using an Aerosol Devices S3 Spot Sampler and extracted with acetonitrile and water (50:50) before being analyzed offline with UHPLC-HRMS. Comparison of Van Krevelen plots generated from mass spectra of this α-pinene ozonylsis experiment and the 500 ppb α-thujene ozonylsis experiment is shown in Figure 4.9 in SI Sect. 4.6.4.

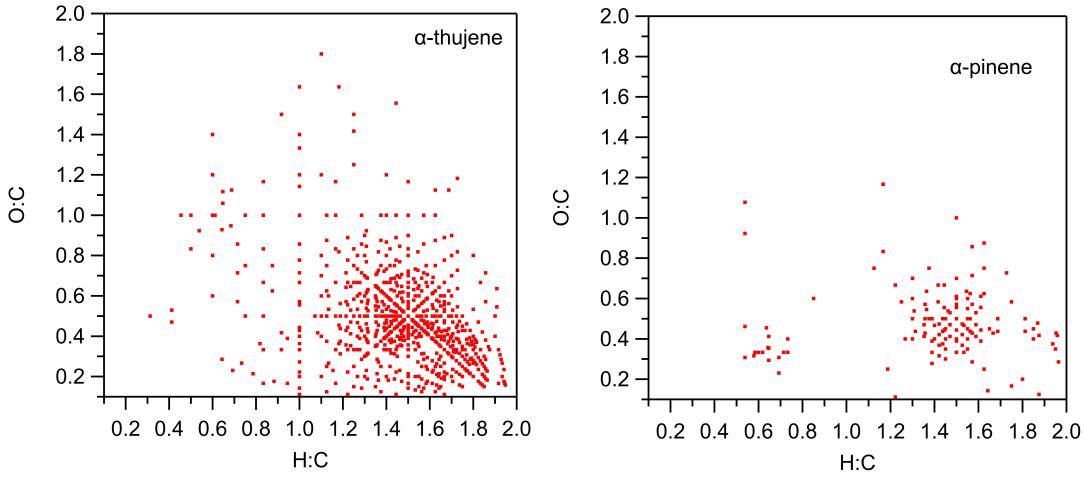

Figure 4.9: Van Krevelen plots (O:C plotted against H:C) for the α-pinene ozonylsis experiment and the 500 ppb α-thujene ozonylsis experiment.

Chapter 5

Conclusions and Future Perspectives

5.1 Conclusions

In this dissertation, we used chemical ionization mass spectrometry coupled with particle sizing and particle composition analysis techniques to investigate the chemical formation processes of ultrafine aerosol particles in three systems.

We observed emission of important precursor gases for nucleation and growth of ultrafine particles from braking processes simulated with our brake dynomometer facility. These gaseous emissions were dependent on the temperature of the brake rotor, the formulation (ceramic vs semi-metallic), and degree of wear (new, gently worn, heavily worn) of the brake pads. For new brake pads, gas emissions were generally higher at lower temperatures compared to worn pads for both tested pad formulations. This is consistent with our observation of a shift in the critical temperature for ultrafine particle formation to higher temperatures with increasing wear on the brake pads. High concentrations of sulfur trioxide, sulfuric acid and formic acid were emitted by both pads at temperatures that coincided with the producution of ultrafine particles, but these emissions were higher for semi-metallic brake pads overall. Formation of inorganic nitrogen species coincided with emission of both NOx and CO, indicating the potential for multiple formation pathways to

simultaneously occur in our chamber. The temperature dependence of CO emission was relatively constant between all brake pad formulations and degrees of wear, but NOx formation was overall less predictable. The ceramic brake pad emitted much higher concentrations of HONO, N_2O_5, and NOx than the semi-metallic pads. The observation of consistency between concentrations suggests cyclical conversion between these species as potential formation pathways. The emitted organic fraction for all brakes was dominated by formic acid, but further investigation of the contribution of observed oxidized organics to ultrafine particle formation and growth is necessary.

In the following study, we oxidized four monoterpenes (α-pinene, β-pinene, Δ-3-carene, α-thujene) with nitrate-radical to elucidate the effects of monoterpene structure on oxidation and SOA formation. The major oxidized, gas-phase reaction products measured with NO_3^- CIMS were distinctly different for each MT system. Measured effective O:C ratio and monomer:dimer ratio of reaction products were anti-correlated to the formation of particles for each system, suggesting condensation of highly oxidized products to the particle-phase. Yield of highly oxidized molecules, organonitrate compounds and SOA of the four systems were observed in this order: Δ-3-carene $>\beta$-pinene $>\alpha$-thujene $>\alpha$-pinene. Considering individual monoterpene structures, the Δ-3-carene and β-pinene first-generation alkoxy products have competitive carbon-carbon scission pathways that allow further propagation of radical sites, whereas these analogous compounds for the α-pinene and α-thujene systems have dominant radical termination pathways. However, the initial α-thujene alkyl radical species was predicted to have a rapid internal radical rearrangement pathway driven by the strained three-membered ring. Although this pathway was not confirmed, a relatively large amount of HOMs, including high molecular weight dimer species, were formed for the α-thujene system. However, nucleation was not observed for this system under the studied conditions, suggesting a complex relationship between monoterpene structure, formation of HOMs and nucleation and growth of ultrafine particles that requires further elucidation.

Finally, a detailed study of the gas-to-particle conversion process for the ozonolysis of α-thujene was conducted. A range of experimental conditions that varied α-thujene:O_3 were investigated to probe the effect of increasing initial RO_2 concentrations on SOA formation. Low-volatility reaction products were generated at similar yields to other monoterpene ozonolysis systems (1-5%). However,

measured SOA yields (2-4%) were suppressed compared to those measured from α-pinene ozonolysis (10-20%) at the same mass loading values. Theoretical growth rates calculated from a simple condensation growth mode under-predicts experimentally determined growth rates (on the order of nm min^{-1}) from particle size distribution measurements in our chamber. This simple model did not consider the contribution of semi-volatile fragment compounds, which were efficiently formed from the α-thujene ozonolysis system and comprised a large fraction of overall oxidized products. These fragment compounds were not previously reported for any monoterpene ozonolysis system, suggesting unique formation pathways that depend on monoterpene structure. Comparison of SOA particle composition from α-pinene and α-thujene ozonolysis using tandem mass spectrometry revealed structural isomers from two compounds with identical molecular formulas, further emphasizing the importance of understanding structural effects on oxidation mechanisms and subsequent reaction products.

5.2 Future Work

Although measurements from our brake dynamometer system provided valuable measurements of gaseous precursors generated from brake-wear, future work quantifying these emissions from real-world driving conditions is crucial for the assessment of their contribution to overall traffic emissions. Characterization of surface reactions of inorganic nitrogen species on the dynamometer chamber walls would help to constrain the role of heterogeneous reactions in formation of these species, as surface area is unrealistically high in chambers. Additional measurements are necessary to begin understanding gas-to-particle conversion processes including ultrafine particle composition, the presence of gaseous amines, and the presence of oxidant species (OH radical, ozone). Modeling of nucleation and growth rates in our system can be performed once these additional precursors are quantified. To this end, sensitivity calibration of the I^- CIMS to individual compounds should also be done to more accurately constrain concentrations.

Structural characterization of monoterpene oxidation products is important for representing volatility and propensity for nucleation and growth of ultrafine particles. Gaining structural information from mass spectrometry techniques is possible, but limited by preparation of samples and sensitivity of measurable ions. Therefore, additional techniques for structural characterization (spectroscopy, molecular assay) are necessary and an active area of study. Many discrepancies exist between laboratory studies of SOA formation from VOC oxidation and ambient observation of SOA, as chamber conditions are often not representative of those in the ambient atmosphere. Concentrations of VOCs and oxidants are often high in chamber experiments, and these experiments are often done in dry conditions. As bimolecular reactions impact the fate of early-generation oxidized reaction products, creating representative distributions of bimolecular reaction partners (RO_2, HO_2, NO_3, etc.) in chamber studies is necessary for evaluation of competitiveness of these pathways relative to unimolecular isomerization reactions. Dry conditions are often used in chamber studies, but the role of water in nucleation from oxidized organics is not well understood. Enhancement of SOA growth for many MT oxidation systems in chamber studies has been reported, but suppression of nucleation and growth of ultrafine particles was also observed. Considering reactive uptake of organics and condensed phase reactions is also important. One such process gaining attention is ion-mediated nucleation from low molecular weight, high volatility organics.

Bibliography

Acosta Navarro, J. C., Smolander, S., Struthers, H., Zorita, E., Ekman, A. M. L., Kaplan, J. O., Guenther, A., Arneth, A., and Riipinen, I.: Global emissions of terpenoid VOCs from terrestrial vegetation in the last millennium, Journal of Geophysical Research: Atmospheres, 119, https://doi.org/10.1002/2013JD021238, 2014.

Alicke, B.: OH formation by HONO photolysis during the BERLIOZ experiment, Journal of Geophysical Research, 108, 8247, https://doi.org/10.1029/2001JD000579, 2003.

Aljawhary, D., Lee, A. K., and Abbatt, J. P.: High-resolution chemical ionization mass spectrometry (ToF-CIMS): Application to study SOA composition and processing, Atmospheric Measurement Techniques, 6, 3211–3224, https://doi.org/10.5194/amt-6-3211-2013, 2013.

Allen, J. L., Oberdörster, G., Morris-schaffer, K., Wong, C., Klocke, C., Sobolewski, M., Conrad, K., Mayer-Proschel, M., and Cory-slechta, D. A.: Developmental Neurotoxicity of Inhaled Ambient Ultrafine Particle Air Pollution: Parallels with Neuropathological and Behavioral Features of Autism and Other Neurodevelopmental Disorders, Neurotoxicology, 59, 140–154, https://doi.org/10.1016/j.neuro.2015.12.014.Developmental, 2017.

Almeida, J., Schobesberger, S., Kürten, A., Ortega, I. K., Kupiainen-Määttä, O., Praplan, A. P., Adamov, A., Amorim, A., Bianchi, F., Breitenlechner, M., David, A., Dommen, J., Donahue, N. M., Downard, A., Dunne, E., Duplissy, J., Ehrhart, S., Flagan, R. C., Franchin, A., Guida, R., Hakala, J., Hansel, A., Heinritzi, M., Henschel, H., Jokinen, T., Junninen, H., Kajos, M., Kangasluoma, J., Keskinen, H., Kupc, A., Kurtén, T., Kvashin, A. N., Laaksonen, A., Lehtipalo, K., Leiminger, M., Leppä, J., Loukonen, V., Makhmutov, V., Mathot, S., McGrath, M. J., Nieminen, T., Olenius, T., Onnela, A., Petäjä, T., Riccobono, F., Riipinen, I., Rissanen, M., Rondo, L., Ruuskanen, T., Santos, F. D., Sarnela, N., Schallhart, S., Schnitzhofer, R., Seinfeld, J. H., Simon, M., Sipilä, M., Stozhkov, Y., Stratmann, F., Tomé, A., Tröstl, J., Tsagkogeorgas, G., Vaattovaara, P., Viisanen, Y., Virtanen, A., Vrtala, A., Wagner, P. E., Weingartner, E., Wex, H., Williamson, C., Wimmer, D., Ye, P., Yli-Juuti, T., Carslaw, K. S., Kulmala, M., Curtius, J., Baltensperger, U., Worsnop, D. R., Vehkamäki, H., and Kirkby, J.: Molecular understanding of sulphuric acid–amine particle nucleation in the atmosphere, Nature, 502, 359–363, https://doi.org/10.1038/nature12663, 2013.

Alves, C., Evtyugina, M., Vicente, A., Conca, E., and Amato, F.: Organic profiles of brake wear particles, Atmospheric Research, 255, 105 557, https://doi.org/10.1016/j.atmosres.2021.105557, 2021.

Atkinson, R. and Arey, J.: Gas-phase tropospheric chemistry of biogenic volatile organic compounds: a review, Atmospheric Environment, 37, 197–219, https://doi.org/https://doi.org/10.1016/S1352-2310(03)00391-1, the 1997 Southern California Ozone Study (SCOS97-NARSTO). Dedicated to the Memory of Dr. Glen Cass (1947-2001), 2003a.

Atkinson, R. and Arey, J.: Gas-phase tropospheric chemistry of biogenic volatile organic compounds: a review, Atmospheric Environment, 37, 197–219, https://doi.org/https://doi.org/10.1016/S1352-2310(03)00391-1, the 1997 Southern California Ozone Study (SCOS97-NARSTO). Dedicated to the Memory of Dr. Glen Cass (1947-2001), 2003b.

Atkinson, R., Winer, A. M., and Pitts, J. N.: Estimation of night-time N2O5 concentrations from ambient NO2 and NO3 radical concentrations and the role of N2O5 in night-time chemistry, Atmospheric Environment (1967), 20, 331–339, https://doi.org/10.1016/0004-6981(86)90035-1, 1986.

Ayres, B. R., Allen, H. M., Draper, D. C., Brown, S. S., Wild, R. J., Jimenez, J. L., Day, D. A., Campuzano-Jost, P., Hu, W., de Gouw, J., Koss, A., Cohen, R. C., Duffey, K. C., Romer, P., Baumann, K., Edgerton, E., Takahama, S., Thornton, J. A., Lee, B. H., Lopez-Hilfiker, F. D., Mohr, C., Wennberg, P. O., Nguyen, T. B., Teng, A., Goldstein, A. H., Olson, K., and Fry, J. L.: Organic nitrate aerosol formation via NO_3 + biogenic volatile organic compounds in the southeastern United States, Atmospheric Chemistry and Physics, 15, 13 377–13 392, https://doi.org/10.5194/acp-15-13377-2015, 2015.

Baboomian, V. J., Crescenzo, G. V., Huang, Y., Mahrt, F., Shiraiwa, M., Bertram, A. K., and Nizkorodov, S. A.: Sunlight can convert atmospheric aerosols into a glassy solid state and modify their environmental impacts, Proceedings of the National Academy of Sciences, 119, https://doi.org/10.1073/pnas.2208121119, 2022.

Baccarini, A., Karlsson, L., Dommen, J., Duplessis, P., Vüllers, J., Brooks, I. M., Saiz-Lopez, A., Salter, M., Tjernström, M., Baltensperger, U., Zieger, P., and Schmale, J.: Frequent new particle formation over the high Arctic pack ice by enhanced iodine emissions, Nature Communications, 11, 1–11, https://doi.org/10.1038/s41467-020-18551-0, 2020.

Barsanti, K. C., Kroll, J. H., and Thornton, J. A.: Formation of Low-Volatility Organic Compounds in the Atmosphere: Recent Advancements and Insights, The Journal of Physical Chemistry Letters, 8, 1503–1511, https://doi.org/10.1021/acs.jpclett.6b02969, pMID: 28281761, 2017.

Beck, L. J., Schobesberger, S., Sipilä, M., Kerminen, V.-M., and Kulmala, M.: Estimation of sulfuric acid concentration using ambient ion composition and concentration data obtained with atmospheric pressure interface time-of-flight ion mass spectrometer, Atmospheric Measurement Techniques, 15, 1957–1965, https://doi.org/10.5194/amt-15-1957-2022, 2022.

Berndt, T. and Böge, O.: Products and mechanism of the reaction of NO3 with selected acyclic monoalkenes, Journal of Atmospheric Chemistry, 21, 286, https://doi.org/10.1007/BF00696759, 1995.

Berndt, T., Stratmann, F., Sipilä, M., Vanhanen, J., Petäjä, T., Mikkilä, J., Grüner, A., Spindler, G., III, R. L. M., Curtius, J., Kulmala, M., and Heintzenberg, J.: Laboratory study on new particle formation from the reaction OH + SO2 influence of experimental conditions, H2O vapour, NH3 and the amine tert-butylamine on the overall process, Atmospheric Chemistry and Physics, 10, 7101–7116, https://doi.org/10.5194/acp-10-7101-2010, 2010.

Berndt, T., Richters, S., Kaethner, R., Voigtländer, J., Stratmann, F., Sipilä, M., Kulmala, M., and Herrmann, H.: Gas-Phase Ozonolysis of Cycloalkenes: Formation of Highly Oxidized RO2 Radicals and Their Reactions with NO, NO2, SO2, and Other RO2 Radicals, The Journal of Physical Chemistry A, 119, 10 336–10 348, https://doi.org/https://doi.org/10.1021/acs.jpca.5b07295, 2015.

Berndt, T., Richters, S., Jokinen, T., Hyttinen, N., Kurtén, T., Otkjær, R. V., Kjaergaard, H. G., Stratmann, F., Herrmann, H., Sipilä, M., Kumala, M., and Ehn, M.: Hydroxyl radical-induced formation of highly oxidized organic compounds, Nature Communications, 7, 9100, https://doi.org/https://doi.org/10.1038/ncomms13677, 2016.

Bi, C., Krechmer, J. E., Frazier, G. O., Xu, W., Lambe, A. T., Claflin, M. S., Lerner, B. M., Jayne, J. T., Worsnop, D. R., Canagaratna, M. R., and Isaacman-VanWertz, G.: Quantification of isomer-resolved iodide chemical ionization mass spectrometry sensitivity and uncertainty using a voltage-scanning approach, Atmospheric Measurement Techniques, 14, 6835–6850, https://doi.org/10.5194/amt-14-6835-2021, 2021.

Bianchi, F., Kurtén, T., Riva, M., Mohr, C., Rissanen, M. P., Roldin, P., Berndt, T., Crounse, J. D., Wennberg, P. O., Mentel, T. F., Wildt, J., Junninen, H., Jokinen, T., Kulmala, M., Worsnop, D. R., Thornton, J. A., Donahue, N., Kjaergaard, H. G., and Ehn, M.: Highly Oxygenated Organic Molecules (HOM) from Gas-Phase Autoxidation Involving Peroxy Radicals: A Key Contributor to Atmospheric Aerosol, Chemical Reviews, 119, 3472–3509, https://doi.org/10.1021/acs.chemrev.8b00395, pMID: 30799608, 2019.

Bofanti, A.: Low-impact friction materials for brake pads, 2016.

Borawski, A.: Testing Passenger Car Brake Pad Exploitation Time's Impact on the Values of the Coefficient of Friction and Abrasive Wear Rate Using a Pin-on-Disc Method, Materials, 15, 1991, https://doi.org/10.3390/ma15061991, 2022.

Boyd, C. M., Sanchez, J., Xu, L., Eugene, A. J., Nah, T., Tuet, W. Y., Guzman, M. I., and Ng, N. L.: Secondary organic aerosol formation from the β-pinene+NOlt;subgt;3lt;/subgt; system: effect of humidity and peroxy radical fate, Atmospheric Chemistry and Physics, 15, https://doi.org/10.5194/acp-15-7497-2015, 2015.

Brophy, P. and Farmer, D. K.: A switchable reagent ion high resolution time-of-flight chemical ionization mass spectrometer for real-time measurement of gas phase oxidized species: Characterization from the 2013 southern oxidant and aerosol study, Atmospheric Measurement Techniques, 8, 2945–2959, https://doi.org/10.5194/amt-8-2945-2015, 2015.

Brown, S. S. and Stutz, J.: Nighttime radical observations and chemistry, Chemical Society Reviews, 41, 6405–6447, https://doi.org/10.1039/c2cs35181a, 2012.

Cai, R. and Jiang, J.: A new balance formula to estimate new particle formation rate: reevaluating the effect of coagulation scavenging, Atmos. Chem. Phys, 17, 12 659–12 675, 2017.

Calvert, J. G., Atkinson, R., Kerr, J. A., Madronich, S., Moortgat, G., Wallington, T. J., and Yarwood, G.: The Mechanisms of Atmospheric Oxidation of the Alkenes, Oxford University Press, 2000.

Chu, B., Chen, T., Liu, Y., Ma, Q., Mu, Y., Wang, Y., Ma, J., Zhang, P., Liu, J., Liu, C., Gui, H., Hu, R., Hu, B., Wang, X., Wang, Y., Liu, J., Xie, P., Chen, J., Liu, Q., Jiang, J., Li, J., He, K., Liu, W., Jiang, G., Hao, J., and He, H.: Application of smog chambers in atmospheric process studies, National Science Review, 9, https://doi.org/10.1093/nsr/nwab103, 2022.

Claflin, M. S. and Ziemann, P. J.: Identification and Quantitation of Aerosol Products of the Reaction of -Pinene with NO3 Radicals and Implications for Gas- and Particle-Phase Reaction Mechanisms, The Journal of Physical Chemistry A, 122, 3640–3652, https://doi.org/10.1021/acs.jpca.8b00692, 2018.

Crounse, J. D., Nielsen, L. B., Jørgensen, S., Kjaergaard, H. G., and Wennberg, P. O.: Autoxidation of organic compounds in the atmosphere, Journal of Physical Chemistry Letters, 4, 3513–3520, https://doi.org/10.1021/jz4019207, 2013.

Crutzen, P. J. and Zimmermann, P. H.: The changing photochemistry of the troposphere, Tellus A: Dynamic Meteorology and Oceanography, 43, 136, https://doi.org/10.3402/tellusa.v43i4.11943, 1991.

Dam, M., Draper, D. C., Marsavin, A., Fry, J. L., and Smith, J. N.: Observations of gas-phase products from the nitrate-radical-initiated oxidation of four monoterpenes, Atmospheric Chemistry and Physics, 22, 9017–9031, https://doi.org/10.5194/acp-22-9017-2022, 2022.

de Almeida, L. F. R., de Oliveira Portella, R., Facanali, R., Marques, M. O. M., and Frei, F.: Dry and wet seasons set the phytochemical profile of the Copaifera langsdorffii Desf. essential oils, Journal of Essential Oil Research, 26, 292–300, https://doi.org/10.1080/10412905.2014.889050, 2014.

DeHaan, D. O., Brauers, T., Oum, K., Stutz, J., Nordmeyer, T., and Finlayson-Pitts, B. J.: Heterogeneous chemistry in the troposphere: Experimental approaches and applications to the chemistry of sea salt particles, International Reviews in Physical Chemistry, 18, 343–385, https://doi.org/10.1080/014423599229910, 1999.

Donahue, N. M., Epstein, S. A., Pandis, S. N., and Robinson, A. L.: A two-dimensional volatility basis set: 1. organic-aerosol mixing thermodynamics, Atmospheric Chemistry and Physics, 11, 3303–3318, https://doi.org/10.5194/acp-11-3303-2011, 2011.

Donahue, N. M., Kroll, J. H., Pandis, S. N., and Robinson, A. L.: A two-dimensional volatility basis set – Part 2: Diagnostics of organic-aerosol evolution, Atmospheric Chemistry and Physics, 12, https://doi.org/10.5194/acp-12-615-2012, 2012.

Dorich, R., Eger, P., Lelieveld, J., and Crowley, J. N.: Iodide CIMS and m/z 62: the detection of HNO_3 as NO_3^- in the presence of PAN, peroxyacetic acid and ozone, Atmospheric Measurement Techniques, 14, 5319–5332, https://doi.org/10.5194/amt-14-5319-2021, 2021.

Draper, D. C., Myllys, N., Hyttinen, N., Møller, K. H., Kjaergaard, H. G., Fry, J. L., Smith, J. N., and Kurtén, T.: Formation of Highly Oxidized Molecules from NO3 Radical Initiated Oxidation of δ-3-Carene: A Mechanistic Study, ACS Earth and Space Chemistry, 3, 1460–1470, https://doi.org/10.1021/acsearthspacechem.9b00143, 2019.

Dunne, E. M., Gordon, H., Kurten, A., Almeida, J., Duplissy, J., Williamson, C., Ortega, I. K., Pringle, K. J., Adamov, A., Baltensperger, U., Barmet, P., Benduhn, F., Bianchi, F., Breitenlechner, M., Clarke, A., Curtius, J., Dommen, J., Donahue, N. M., Ehrhart, S., Flagan, R. C., Franchin, A., Guida, R., Hakala, J., Hansel, A., Heinritzi, M., Jokinen, T., Kangasluoma, J., Kirkby, J., Kulmala, M., Kupc, A., Lawler, M. J., Lehtipalo, K., Makhmutov, V., Mann, G., Mathot, S., Merikanto, J., Miettinen, P., Nenes, A., Onnela, A., Rap, A., Reddington, C. L. S., Riccobono, F., Richards, N. A. D., Rissanen, M. P., Rondo, L., Sarnela, N., Schobesberger, S., Sengupta, K., Simon, M., Sipila, M., Smith, J. N., Stozkhov, Y., Tome, A., Trostl, J., Wagner, P. E., Wimmer, D., Winkler, P. M., Worsnop, D. R., and Carslaw, K. S.: Global atmospheric particle formation from CERN CLOUD measurements, Science, 354, 1119–1124, https://doi.org/10.1126/science.aaf2649, 2016.

Ehn, M., Kleist, E., Junninen, H., Petäjä, T., Lönn, G., Schobesberger, S., Dal Maso, M., Trimborn, A., Kulmala, M., Worsnop, D. R., Wahner, A., Wildt, J., and Mentel, T. F.: Gas phase formation of extremely oxidized pinene reaction products in chamber and ambient air, Atmospheric Chemistry and Physics, 12, 5113–5127, https://doi.org/10.5194/acp-12-5113-2012, 2012.

Ehn, M., Thornton, J. A., Kleist, E., Sipilä, M., Junninen, H., Pullinen, I., Springer, M., Rubach, F., Tillmann, R., Lee, B., Lopez-Hilfiker, F., Andres, S., Acir, I. H., Rissanen, M., Jokinen, T., Schobesberger, S., Kangasluoma, J., Kontkanen, J., Nieminen, T., Kurtén, T., Nielsen, L. B., Jørgensen, S., Kjaergaard, H. G., Canagaratna, M., Maso, M. D., Berndt, T., Petäjä, T., Wahner, A., Kerminen, V. M., Kulmala, M., Worsnop, D. R., Wildt, J., and Mentel, T. F.: A large source of low-volatility secondary organic aerosol, Nature, 506, 476–479, https://doi.org/10.1038/nature13032, 2014.

Eisele, F. L. and Tanner, D. J.: Measurement of the gas phase concentration of H2SO4 and methane sulfonic acid and estimates of H2SO4 production and loss in the atmosphere, Journal of Geophysical Research: Atmospheres, 98, 9001–9010, https://doi.org/10.1029/93JD00031, 1993.

Finlayson-Pitts, B. J. and Pitts, J. N.: Chemistry of the Upper and Lower Atmosphere, Academic Press, 2000.

Forster, P., Storelvmo, K., Armour, W., Collins, J., Dufresne, D., Frame, D., Lunt, T., Mauritsen, M., Palmer, M., Watanabe, M., and Zhang, H.: The Earth's Energy Budget, Climate Feedbacks and Climate Sensitivity, Climate Change 2021 – The Physical Science Basis, pp. 923–1054, https://doi.org/10.1017/9781009157896.009, 2023.

Friedman, B. and Farmer, D. K.: SOA and gas phase organic acid yields from the sequential photooxidation of seven monoterpenes, Atmospheric Environment, 187, 335–345, https://doi.org/https://doi.org/10.1016/j.atmosenv.2018.06.003, 2018.

Fry, J. L., Draper, D. C., Zarzana, K. J., Campuzano-Jost, P., Day, D. A., Jimenez, J. L., Brown, S. S., Cohen, R. C., Kaser, L., Hansel, A., Cappellin, L., Karl, T., Hodzic Roux, A., Turnipseed, A., Cantrell, C., Lefer, B. L., and Grossberg, N.: Observations of gas- and aerosol-phase organic nitrates at BEACHON-RoMBAS 2011, Atmospheric Chemistry and Physics, 13, 8585–8605, https://doi.org/10.5194/acp-13-8585-2013, 2013.

Fry, J. L., Draper, D. C., Barsanti, K. C., Smith, J. N., Ortega, J., Winkler, P. M., Lawler, M. J., Brown, S. S., Edwards, P. M., Cohen, R. C., and Lee, L.: Secondary organic aerosol formation and organic nitrate yield from NO3 oxidation of biogenic hydrocarbons, Environmental Science and Technology, 48, 11 944–11 953, https://doi.org/10.1021/es502204x, 2014.

Fussell, J. C., Franklin, M., Green, D. C., Gustafsson, M., Harrison, R. M., Hicks, W., Kelly, F. J., Kishta, F., Miller, M. R., Mudway, I. S., Oroumiyeh, F., Selley, L., Wang, M., and Zhu, Y.: A Review of Road Traffic-Derived Non-Exhaust Particles: Emissions, Physicochemical Characteristics, Health Risks, and Mitigation Measures, Environmental Science Technology, 56, 6813–6835, https://doi.org/10.1021/acs.est.2c01072, 2022.

Gauderman, W. J., Avol, E., Lurmann, F., Kuenzli, N., Gilliland, F., Peters, J., and McConnell, R.: Childhood Asthma and Exposure to Traffic and Nitrogen Dioxide, Epidemiology, 16, 737–743, https://doi.org/10.1097/01.ede.0000181308.51440.75, 2005.

Geron, C., Rasmussen, R., Arnts, R. R., and Guenther, A.: A review and synthesis of monoterpene speciation from forests in the United States, Atmospheric Environment, 34, 1761–1781, https://doi.org/10.1016/S1352-2310(99)00364-7, 2000.

Gordon, H., Kirkby, J., Baltensperger, U., Bianchi, F., Breitenlechner, M., Curtius, J., Dias, A., Dommen, J., Donahue, N. M., Dunne, E. M., Duplissy, J., Ehrhart, S., Flagan, R. C., Frege, C., Fuchs, C., Hansel, A., Hoyle, C. R., Kulmala, M., Kürten, A., Lehtipalo, K., Makhmutov, V., Molteni, U., Rissanen, M. P., Stozkhov, Y., Tröstl, J., Tsagkogeorgas, G., Wagner, R., Williamson, C., Wimmer, D., Winkler, P. M., Yan, C., and Carslaw, K. S.: Causes and importance of new particle formation in the present-day and preindustrial atmospheres, Journal of Geophysical Research: Atmospheres, 122, 8739–8760, https://doi.org/10.1002/2017JD026844, 2017.

Guenther, A.: Natural emissions of non-methane volatile organic compounds, carbon monoxide, and oxides of nitrogen from North America, Atmospheric Environment, 34, 2205–2230, https://doi.org/10.1016/S1352-2310(99)00465-3, 2000.

Guo, Y., Shen, H., Pullinen, I., Luo, H., Kang, S., Vereecken, L., Fuchs, H., Hallquist, M., Acir, I.-H., Tillmann, R., Rohrer, F., Wildt, J., Kiendler-Scharr, A., Wahner, A., Zhao, D., and Mentel, T. F.: Identification of highly oxygenated organic molecules and their role in aerosol formation in the reaction of limonene with nitrate radical, Atmospheric Chemistry and Physics, 22, 11 323–11 346, https://doi.org/10.5194/acp-22-11323-2022, 2022.

Hagino, H., Oyama, M., and Sasaki, S.: Laboratory testing of airborne brake wear particle emissions using a dynamometer system under urban city driving cycles, Atmospheric Environment, 131, 269–278, https://doi.org/10.1016/j.atmosenv.2016.02.014, 2016.

Hallquist, M., Wangberg, I., Ljungstrom, E., Barnes, I., and Becker, K.: Aerosol and Product Yields from NO3 radical-Initiated Oxidation of Selected Monoterpenes, Environmental Science and Technology, 33, 553–559, https://doi.org/10.1021/es980292s, 1999.

Hallquist, M., Wenger, J. C., Baltensperger, U., Rudich, Y., Simpson, D., Claeys, M., Dommen, J., Donahue, N. M., George, C., Goldstein, A. H., Hamilton, J. F., Herrmann, H., Hoffmann, T., Iinuma, Y., Jang, M., Jenkin, M. E., Jimenez, J. L., Kiendler-Scharr, A., Maenhaut, W., McFiggans, G., Mentel, T. F., Monod, A., Prévôt, A. S. H., Seinfeld, J. H., Surratt, J. D., Szmigielski, R., and Wildt, J.: The formation, properties and impact of secondary organic aerosol: current and emerging issues, Atmospheric Chemistry and Physics, 9, 5155–5236, https://doi.org/10.5194/acp-9-5155-2009, 2009.

Hasan, G., Salo, V.-T., Valiev, R. R., Kubečka, J., and Kurtén, T.: Comparing Reaction Routes for 3(RO···OR) Intermediates Formed in Peroxy Radical Self- and Cross-Reactions, The Journal of Physical Chemistry A, 124, 8305–8320, https://doi.org/10.1021/acs.jpca.0c05960, pMID: 32902986, 2020.

Huang, Y., Zhao, R., Charan, S. M., Kenseth, C. M., Zhang, X., and Seinfeld, J. H.: Unified Theory of Vapor–Wall Mass Transport in Teflon-Walled Environmental Chambers, Environmental Science Technology, 52, 2134–2142, https://doi.org/10.1021/acs.est.7b05575, 2018.

Hyttinen, N., Kupiainen-Määttä, O., Rissanen, M. P., Muuronen, M., Ehn, M., and Kurtén, T.: Modeling the Charging of Highly Oxidized Cyclohexene Ozonolysis Products Using Nitrate-Based Chemical Ionization, The Journal of Physical Chemistry A, 119, 6339–6345, https://doi.org/ https://doi.org/10.1021/acs.jpca.5b01818, 2015.

Hyttinen, N., Wolf, M., Rissanen, M. P., Ehn, M., Peräkylä, O., Kurtén, T., and Prisle, N. L.: Gas-to-Particle Partitioning of Cyclohexene- and α-Pinene-Derived Highly Oxygenated Dimers Evaluated Using COSMOtherm, The Journal of Physical Chemistry A, 125, 3726–3738, https://doi.org/10.1021/acs.jpca.0c11328, 2021.

Isaacman-VanWertz, G., Massoli, P., O'Brien, R., Lim, C., Franklin, J. P., Moss, J. A., Hunter, J. F., Nowak, J. B., Canagaratna, M. R., Misztal, P. K., et al.: Chemical evolution of atmospheric organic carbon over multiple generations of oxidation, Nature chemistry, 10, 462–468, 2018.

Iyer, S., Lopez-Hilfiker, F., Lee, B. H., Thornton, J. A., and Kurtén, T.: Modeling the Detection of Organic and Inorganic Compounds Using Iodide-Based Chemical Ionization, The Journal of Physical Chemistry A, 120, 576–587, https://doi.org/10.1021/acs.jpca.5b09837, 2016.

Iyer, S., He, X., Hyttinen, N., Kurtén, T., and Rissanen, M. P.: Computational and Experimental Investigation of the Detection of HO2 Radical and the Products of Its Reaction with Cyclohexene Ozonolysis Derived RO2 Radicals by an Iodide-Based Chemical Ionization Mass Spectrometer, The Journal of Physical Chemistry A, 121, 6778–6789, https://doi.org/10.1021/acs.jpca.7b01588, 2017.

Iyer, S., Rissanen, M. P., Valiev, R., Barua, S., Krechmer, J. E., Thornton, J., Ehn, M., and Kurtén, T.: Molecular mechanism for rapid autoxidation in α-pinene ozonolysis, Nature Communications, 12, 878, https://doi.org/10.1038/s41467-021-21172-w, 2021.

Jenkin, M. E., Valorso, R., Aumont, B., and Rickard, A. R.: Estimation of rate coefficients and branching ratios for reactions of organic peroxy radicals for use in automated mechanism construction, Atmospheric Chemistry and Physics, 19, 7691–7717, https://doi.org/10.5194/ acp-19-7691-2019, 2019.

Jimenez, J. L., Canagaratna, M. R., Donahue, N. M., Prevot, A. S. H., Zhang, Q., Kroll, J. H., DeCarlo, P. F., Allan, J. D., Coe, H., Ng, N. L., Aiken, A. C., Docherty, K. S., Ulbrich, I. M., Grieshop, A. P., Robinson, A. L., Duplissy, J., Smith, J. D., Wilson, K. R., Lanz, V. A., Hueglin, C., Sun, Y. L., Tian, J., Laaksonen, A., Raatikainen, T., Rautiainen, J., Vaattovaara, P., Ehn, M., Kulmala, M., Tomlinson, J. M., Collins, D. R., Cubison, M. J., Dunlea, J., Huffman, J. A., Onasch, T. B., Alfarra, M. R., Williams, P. I., Bower, K., Kondo, Y., Schneider, J., Drewnick, F., Borrmann, S., Weimer, S., Demerjian, K., Salcedo, D., Cottrell, L., Griffin, R., Takami, A., Miyoshi, T., Hatakeyama, S., Shimono, A., Sun, J. Y., Zhang, Y. M., Dzepina, K., Kimmel,

J. R., Sueper, D., Jayne, J. T., Herndon, S. C., Trimborn, A. M., Williams, L. R., Wood, E. C., Middlebrook, A. M., Kolb, C. E., Baltensperger, U., and Worsnop, D. R.: Evolution of Organic Aerosols in the Atmosphere, Science, 326, 1525–1529, https://doi.org/10.1126/science.1180353, 2009.

Johnson, D. and Marston, G.: The gas-phase ozonolysis of unsaturated volatile organic compounds in the troposphere, Chemical Society Reviews, 37, 699, https://doi.org/10.1039/b704260b, 2008.

Jokinen, T., Sipilä, M., Junninen, H., Ehn, M., Lönn, G., Hakala, J., Petäjä, T., Mauldin, R. L., Kulmala, M., and Worsnop, D. R.: Atmospheric sulphuric acid and neutral cluster measurements using CI-APi-TOF, Atmospheric Chemistry and Physics, 12, 4117–4125, https://doi.org/10.5194/acp-12-4117-2012, 2012.

Jokinen, T., Sipilä, M., Richters, S., Kerminen, V.-M., Paasonen, P., Stratmann, F., Worsnop, D., Kulmala, M., Ehn, M., Herrmann, H., and Berndt, T.: Rapid Autoxidation Forms Highly Oxidized RO2 Radicals in the Atmosphere, Angewandte Chemie International Edition, 53, 14 596–14 600, https://doi.org/10.1002/anie.201408566, 2014.

Keehan, N. I., Brownwood, B., Marsavin, A., Day, D. A., and Fry, J. L.: A thermal-dissociation–cavity ring-down spectrometer (TD-CRDS) for the detection of organic nitrates in gas and particle phases, Atmospheric Measurement Techniques, 13, 6255–6269, https://doi.org/10.5194/amt-13-6255-2020, 2020.

Kenseth, C. M., Hafeman, N. J., Huang, Y., Dalleska, N. F., Stoltz, B. M., and Seinfeld, J. H.: Synthesis of Carboxylic Acid and Dimer Ester Surrogates to Constrain the Abundance and Distribution of Molecular Products in α-Pinene and -Pinene Secondary Organic Aerosol, Environmental Science Technology, 54, 12 829–12 839, https://doi.org/10.1021/acs.est.0c01566, 2020.

Kercher, J. P., Riedel, T. P., and Thornton, J. A.: Chlorine activation by N2O5: simultaneous, in situ detection of ClNO2 and N2O5 by chemical ionization mass spectrometry, Atmospheric Measurement Techniques, 2, 193–204, https://doi.org/10.5194/amt-2-193-2009, 2009.

Kirkby, J., Curtius, J., Almeida, J., Dunne, E., Duplissy, J., Ehrhart, S., Franchin, A., Gagné, S., Ickes, L., Kürten, A., Kupc, A., Metzger, A., Riccobono, F., Rondo, L., Schobesberger, S., Tsagkogeorgas, G., Wimmer, D., Amorim, A., Bianchi, F., Breitenlechner, M., David, A., Dommen, J., Downard, A., Ehn, M., Flagan, R. C., Haider, S., Hansel, A., Hauser, D., Jud, W., Junninen, H., Kreissl, F., Kvashin, A., Laaksonen, A., Lehtipalo, K., Lima, J., Lovejoy, E. R., Makhmutov, V., Mathot, S., Mikkilä, J., Minginette, P., Mogo, S., Nieminen, T., Onnela, A., Pereira, P., Petäjä, T., Schnitzhofer, R., Seinfeld, J. H., Sipilä, M., Stozhkov, Y., Stratmann, F., Tomé, A., Vanhanen, J., Viisanen, Y., Vrtala, A., Wagner, P. E., Walther, H., Weingartner, E., Wex, H., Winkler, P. M., Carslaw, K. S., Worsnop, D. R., Baltensperger, U., and Kulmala, M.: Role of sulphuric acid, ammonia and galactic cosmic rays in atmospheric aerosol nucleation, Nature, 476, 429–433, https://doi.org/10.1038/nature10343, 2011.

Krechmer, J. E., Coggon, M. M., Massoli, P., Nguyen, T. B., Crounse, J. D., Hu, W., Day, D. A., Tyndall, G. S., Henze, D. K., Rivera-Rios, J. C., Nowak, J. B., Kimmel, J. R., Mauldin, R. L. I., Stark, H., Jayne, J. T., Sipilä, M., Junninen, H., St. Clair, J. M., Zhang, X., Feiner, P. A., Zhang, L., Miller, D. O., Brune, W. H., Keutsch, F. N., Wennberg, P. O., Seinfeld, J. H., Worsnop, D. R., Jimenez, J. L., and Canagaratna, M. R.: Formation of Low Volatility

Organic Compounds and Secondary Organic Aerosol from Isoprene Hydroxyhydroperoxide Low-NO Oxidation, Environmental Science & Technology, 49, 10 330–10 339, https://doi.org/10.1021/acs.est.5b02031, 2015.

Krechmer, J. E., Pagonis, D., Ziemann, P. J., and Jimenez, J. L.: Quantification of Gas-Wall Partitioning in Teflon Environmental Chambers Using Rapid Bursts of Low-Volatility Oxidized Species Generated in Situ, Environmental Science Technology, 50, 5757–5765, https://doi.org/10.1021/acs.est.6b00606, 2016.

Krechmer, J. E., Day, D. A., and Jimenez, J. L.: Always Lost but Never Forgotten: Gas-Phase Wall Losses Are Important in All Teflon Environmental Chambers, Environmental Science Technology, 54, https://doi.org/10.1021/acs.est.0c03381, 2020.

Kroll, J. H. and Seinfeld, J. H.: Chemistry of secondary organic aerosol: Formation and evolution of low-volatility organics in the atmosphere, https://doi.org/10.1016/j.atmosenv.2008.01.003, 2008.

Kuang, C., Riipinen, I., Sihto, S.-L., Kulmala, M., McCormick, A. V., and McMurry, P. H.: An improved criterion for new particle formation in diverse atmospheric environments, Atmospheric Chemistry and Physics, 10, 8469–8480, https://doi.org/10.5194/acp-10-8469-2010, 2010.

Kulmala, M., Vehkamäki, H., Petäjä, T., Dal Maso, M., Lauri, A., Kerminen, V.-M., Birmili, W., and McMurry, P.: Formation and growth rates of ultrafine atmospheric particles: a review of observations, Journal of Aerosol Science, 35, 143–176, https://doi.org/10.1016/j.jaerosci.2003.10.003, 2004.

Kulmala, M., Petäjä, T., Ehn, M., Thornton, J., Sipilä, M., Worsnop, D., and Kerminen, V.-M.: Chemistry of Atmospheric Nucleation: On the Recent Advances on Precursor Characterization and Atmospheric Cluster Composition in Connection with Atmospheric New Particle Formation, Annual Review of Physical Chemistry, 65, 21–37, https://doi.org/10.1146/annurev-physchem-040412-110014, 2014.

Kürten, A., Rondo, L., Ehrhart, S., and Curtius, J.: Calibration of a chemical ionization mass spectrometer for the measurement of gaseous sulfuric acid, Journal of Physical Chemistry A, 116, 6375–6386, https://doi.org/10.1021/jp212123n, 2012.

Kurtén, T., Tiusanen, K., Roldin, P., Rissanen, M., Luy, J.-N., Boy, M., Ehn, M., and Donahue, N.: α-Pinene Autoxidation Products May Not Have Extremely Low Saturation Vapor Pressures Despite High O:C Ratios, The Journal of Physical Chemistry A, 120, https://doi.org/10.1021/acs.jpca.6b02196, 2016.

Kurtén, T., Møller, K. H., Nguyen, T. B., Schwantes, R. H., Misztal, P. K., Su, L., Wennberg, P. O., Fry, J. L., and Kjaergaard, H. G.: Alkoxy Radical Bond Scissions Explain the Anomalously Low Secondary Organic Aerosol and Organonitrate Yields from α-Pinene + NO3, Journal of Physical Chemistry Letters, 8, 2826–2834, https://doi.org/10.1021/acs.jpclett.7b01038, 2017.

Kurtén, T., Rissanen, M. P., Mackeprang, K., Thornton, J. A., Hyttinen, N., Jørgensen, S., Ehn, M., and Kjaergaard, H. G.: Computational Study of Hydrogen Shifts and Ring-Opening Mechanisms in α-Pinene Ozonolysis Products, The Journal of Physical Chemistry A, pp. 11 366–11 375, https://doi.org/10.1021/acs.jpca.5b08948, 2015.

Lee, A., Goldstein, A. H., Keywood, M. D., Varutbangkul, V., Bahreini, R., Ng, N. L., Flagan, R. C., and Seinfeld, J. H.: Gas-phase products and secondary aerosol yields from the ozonolysis of ten different terpenes, JGR Atmospheres, 111, https://doi.org/https://doi.org/10.1029/2005JD006437, 2006.

Lee, B. H., Lopez-Hilfiker, F. D., Mohr, C., Kurtén, T., Worsnop, D. R., and Thornton, J. A.: An iodide-adduct high-resolution time-of-flight chemical-ionization mass spectrometer: Application to atmospheric inorganic and organic compounds, Environmental Science and Technology, 48, 6309–6317, https://doi.org/10.1021/es500362a, 2014.

Lee, B. H., Mohr, C., Lopez-Hilfiker, F. D., Lutz, A., Hallquist, M., Lee, L., Romer, P., Cohen, R. C., Iyer, S., Kurtén, T., Hu, W., Day, D. A., Campuzano-Jost, P., Jimenez, J. L., Xu, L., Ng, N. L., Guo, H., Weber, R. J., Wild, R. J., Brown, S. S., Koss, A., de Gouw, J., Olson, K., Goldstein, A. H., Seco, R., Kim, S., McAvey, K., Shepson, P. B., Starn, T., Baumann, K., Edgerton, E. S., Liu, J., Shilling, J. E., Miller, D. O., Brune, W., Schobesberger, S., D'Ambro, E. L., and Thornton, J. A.: Highly functionalized organic nitrates in the southeast United States: Contribution to secondary organic aerosol and reactive nitrogen budgets, Proceedings of the National Academy of Sciences, 113, 1516–1521, https://doi.org/10.1073/pnas.1508108113, 2016.

Lee, S. H., Gordon, H., Li, Y., Zhang, R., and Lehtipalo, K.: New Particle Formation in the Atmosphere : From Molecular Clusters to Global Climate Journal of Geophysical Research : Atmospheres, https://doi.org/10.1029/2018JD029356, 2019.

Leslie, M. D., Ridoli, M., Murphy, J. G., and Borduas-Dedekind, N.: Isocyanic acid (HNCO) and its fate in the atmosphere: a review, Environmental Science: Processes Impacts, 21, 793–808, https://doi.org/10.1039/C9EM00003H, 2019.

Li, X., Chee, S., Hao, J., Abbatt, J. P., Jiang, J., and Smith, J. N.: Relative humidity effect on the formation of highly oxidized molecules and new particles during monoterpene oxidation, Atmospheric Chemistry and Physics, 19, 1555–1570, https://doi.org/10.5194/acp-19-1555-2019, 2019.

Liao, S., Zhang, J., Yu, F., Zhu, M., Liu, J., Ou, J., Dong, H., Sha, Q., Zhong, Z., Xie, Y., Luo, H., Zhang, L., and Zheng, J.: High Gaseous Nitrous Acid (HONO) Emissions from Light-Duty Diesel Vehicles, Environmental Science Technology, 55, 200–208, https://doi.org/10.1021/acs.est.0c05599, 2021.

Lopez-Hilfiker, F. D., Iyer, S., Mohr, C., Lee, B. H., D'ambro, E. L., Kurtén, T., and Thornton, J. A.: Constraining the sensitivity of iodide adduct chemical ionization mass spectrometry to multifunctional organic molecules using the collision limit and thermodynamic stability of iodide ion adducts, Atmospheric Measurement Techniques, 9, 1505–1512, https://doi.org/10.5194/amt-9-1505-2016, 2016a.

Lopez-Hilfiker, F. D., Iyer, S., Mohr, C., Lee, B. H., D'ambro, E. L., Kurtén, T., and Thornton, J. A.: Constraining the sensitivity of iodide adduct chemical ionization mass spectrometry to multifunctional organic molecules using the collision limit and thermodynamic stability of iodide ion adducts, Atmospheric Measurement Techniques, 9, 1505–1512, https://doi.org/10.5194/amt-9-1505-2016, 2016b.

Lv, Y., Chen, X., Wei, S., Zhu, R., Wang, B., Chen, B., Kong, M., and Zhang, J. J.: Sources, concentrations, and transport models of ultrafine particles near highways: a Literature Review, Building and Environment, 186, 107 325, https://doi.org/10.1016/j.buildenv.2020.107325, 2020.

Malachova, K., Kukutschova, J., Rybkova, Z., Sezimova, H., Placha, D., Cabanova, K., and Filip, P.: Toxicity and mutagenicity of low-metallic automotive brake pad materials, Ecotoxicology and Environmental Safety, 131, 37–44, https://doi.org/10.1016/j.ecoenv.2016.05.003, 2016.

Malloy, Q. G. J., Nakao, S., Qi, L., Austin, R., Stothers, C., Hagino, H., and III, D. R. C.: Real-Time Aerosol Density Determination Utilizing a Modified Scanning Mobility Particle Sizer—Aerosol Particle Mass Analyzer System, Aerosol Science and Technology, 43, 673–678, https://doi.org/10.1080/02786820902832960, 2009.

Massoli, P., Stark, H., Canagaratna, M. R., Krechmer, J. E., Xu, L., Ng, N. L., Mauldin, R. L., Yan, C., Kimmel, J., Misztal, P. K., Jimenez, J. L., Jayne, J. T., and Worsnop, D. R.: Ambient Measurements of Highly Oxidized Gas-Phase Molecules during the Southern Oxidant and Aerosol Study (SOAS) 2013, ACS Earth and Space Chemistry, 2, 653–672, https://doi.org/10.1021/acsearthspacechem.8b00028, 2018.

Mathissen, M., Grochowicz, J., Schmidt, C., Vogt, R., zum Hagen, F. H. F., Grabiec, T., Steven, H., and Grigoratos, T.: A novel real-world braking cycle for studying brake wear particle emissions, Wear, 414-415, 219–226, https://doi.org/10.1016/j.wear.2018.07.020, 2018.

Matsunaga, A. and ‡, P. J. Z.: Gas-Wall Partitioning of Organic Compounds in a Teflon Film Chamber and Potential Effects on Reaction Product and Aerosol Yield Measurements, Aerosol Science and Technology, 44, 881–892, https://doi.org/10.1080/02786826.2010.501044, 2010.

Mentel, T. F., Springer, M., Ehn, M., Kleist, E., Pullinen, I., Kurtén, T., Rissanen, M., Wahner, A., and Wildt, J.: Formation of highly oxidized multifunctional compounds: autoxidation of peroxy radicals formed in the ozonolysis of alkenes – deduced from structure–product relationships, Atmospheric Chemistry and Physics, 15, 6745–6765, https://doi.org/10.5194/acp-15-6745-2015, 2015.

Merikanto, J., Spracklen, D. V., Mann, G. W., Pickering, S. J., and Carslaw, K. S.: Impact of nucleation on global CCN, Atmospheric Chemistry and Physics, 9, 8601–8616, https://doi.org/10.5194/acp-9-8601-2009, 2009.

Miljevic, B., Hedayat, F., Stevanovic, S., Fairfull-Smith, K. E., Bottle, S. E., and Ristovski, Z. D.: To Sonicate or Not to Sonicate PM Filters: Reactive Oxygen Species Generation Upon Ultrasonic Irradiation, Aerosol Science and Technology, 48, 1276–1284, https://doi.org/10.1080/02786826.2014.981330, 2014.

Millet, D. B., Baasandorj, M., Farmer, D. K., Thornton, J. A., Baumann, K., Brophy, P., Chaliyakunnel, S., de Gouw, J. A., Graus, M., Hu, L., Koss, A., Lee, B. H., Lopez-Hilfiker, F. D., Neuman, J. A., Paulot, F., Peischl, J., Pollack, I. B., Ryerson, T. B., Warneke, C., Williams, B. J., and Xu, J.: A large and ubiquitous source of atmospheric formic acid, Atmospheric Chemistry and Physics, 15, 6283–6304, https://doi.org/10.5194/acp-15-6283-2015, 2015.

Mohr, C., Thornton, J., Heitto, A., Lopez-Hilfiker, F., Lutz, A., Riipinen, I., Hong, J., Donahue, N., Hallquist, M., Petäjä, T., Kulmala, M., and Yli-Juuti, T.: Molecular identification

of organic vapors driving atmospheric nanoparticle growth, Nature Communications, p. 4442, https://doi.org/10.1038/s41467-019-12473-2, 2019.

Møller, K. H., Otkjær, R. V., Chen, J., and Kjaergaard, H. G.: Double Bonds Are Key to Fast Unimolecular Reactivity in First-Generation Monoterpene Hydroxy Peroxy Radicals, Journal of Physical Chemistry A, 124, 2885–2896, https://doi.org/10.1021/acs.jpca.0c01079, 2020.

Molteni, U., Simon, M., Heinritzi, M., Hoyle, C. R., Bernhammer, A.-K., Bianchi, F., Breitenlechner, M., Brilke, S., Dias, A., Duplissy, J., Frege, C., Gordon, H., Heyn, C., Jokinen, T., Kürten, A., Lehtipalo, K., Makhmutov, V., Petäjä, T., Pieber, S. M., Praplan, A. P., Schobesberger, S., Steiner, G., Stozhkov, Y., Tomé, A., Tröstl, J., Wagner, A. C., Wagner, R., Williamson, C., Yan, C., Baltensperger, U., Curtius, J., Donahue, N. M., Hansel, A., Kirkby, J., Kulmala, M., Worsnop, D. R., and Dommen, J.: Formation of Highly Oxygenated Organic Molecules from α-Pinene Ozonolysis: Chemical Characteristics, Mechanism, and Kinetic Model Development, ACS Earth and Space Chemistry, 3, 873–883, https://doi.org/10.1021/acsearthspacechem.9b00035, 2019.

Nakao, S., Tang, P., Tang, X., Clark, C. H., Qi, L., Seo, E., Asa-Awuku, A., and Cocker, D.: Density and elemental ratios of secondary organic aerosol: Application of a density prediction method, Atmospheric Environment, 68, 273–277, https://doi.org/https://doi.org/10.1016/j.atmosenv.2012.11.006, 2013.

Nakashima, Y. and Kondo, Y.: Nitrous acid (HONO) emission factors for diesel vehicles determined using a chassis dynamometer, Science of The Total Environment, 806, 150 927, https://doi.org/10.1016/j.scitotenv.2021.150927, 2022.

Namgung, H.-G., Kim, J.-B., Woo, S.-H., Park, S., Kim, M., Kim, M.-S., Bae, G.-N., Park, D., and Kwon, S.-B.: Generation of Nanoparticles from Friction between Railway Brake Disks and Pads, Environmental Science Technology, 50, 3453–3461, https://doi.org/10.1021/acs.est.5b06252, 2016.

Ng, N., Brown, S. S., Archibald, A. T., Atlas, E., Cohen, R. C., Crowley, J. N., Day, D. A., Donahue, N. M., Fry, J. L., Fuchs, H., Griffin, R. J., Guzman, M. I., Herrmann, H., Hodzic, A., Iinuma, Y., Kiendler-Scharr, A., Lee, B. H., Luecken, D. J., Mao, J., McLaren, R., Mutzel, A., Osthoff, H. D., Ouyang, B., Picquet-Varrault, B., Platt, U., Pye, H. O., Rudich, Y., Schwantes, R. H., Shiraiwa, M., Stutz, J., Thornton, J. A., Tilgner, A., Williams, B. J., and Zaveri, R. A.: Nitrate radicals and biogenic volatile organic compounds: Oxidation, mechanisms, and organic aerosol, 17, 2103–2162, https://doi.org/10.5194/acp-17-2103-2017, 2017.

Nie, W., Ding, A. J., Xie, Y. N., Xu, Z., Mao, H., Kerminen, V.-M., Zheng, L. F., Qi, X. M., Huang, X., Yang, X.-Q., Sun, J. N., Herrmann, E., Petäjä, T., Kulmala, M., and Fu, C. B.: Influence of biomass burning plumes on HONO chemistry in eastern China, Atmospheric Chemistry and Physics, 15, 1147–1159, https://doi.org/10.5194/acp-15-1147-2015, 2015.

Niemann, H., Winner, H., Asbach, C., Kaminski, H., and Zessinger, M.: System Identification Method for Brake Particle Emission Measurements of Passenger Car Disc Brakes on a Dynamometer, https://doi.org/10.4271/2018-01-1884, 2018.

Nizkorodov, S. A., Laskin, J., and Laskin, A.: Molecular chemistry of organic aerosols through the application of high resolution mass spectrometry, Physical Chemistry Chemical Physics, 13, 3612–3629, https://doi.org/10.1039/c0cp02032j, 2011.

Nosko, O. and Olofsson, U.: Quantification of ultrafine airborne particulate matter generated by the wear of car brake materials, Wear, 374-375, 92–96, https://doi.org/10.1016/j.wear.2017.01.003, 2017.

Nosko, O., Vanhanen, J., and Olofsson, U.: Emission of 1.3–10 nm airborne particles from brake materials, Aerosol Science and Technology, 51, 91–96, https://doi.org/10.1080/02786826.2016.1255713, 2017.

Novelli, A., Cho, C., Fuchs, H., Hofzumahaus, A., Rohrer, F., Tillmann, R., Kiendler-Scharr, A., Wahner, A., and Vereecken, L.: Experimental and theoretical study on the impact of a nitrate group on the chemistry of alkoxy radicals, Physical Chemistry Chemical Physics, 23, https://doi.org/10.1039/D0CP05555G, 2021.

Oberdörster, G., Sharp, Z., Atudorei, V., Elder, A., Gelein, R., Kreyling, W., and Cox, C.: Translocation of Inhaled Ultrafine Particles to the Brain, Inhalation Toxicology, 16, 437–445, 2004.

OECD: Non-exhaust Particulate Emissions from Road Transport, https://doi.org/https://doi.org/https://doi.org/10.1787/4a4dc6ca-en, 2020.

Otkjær, R. V., Jakobsen, H. H., Tram, C. M., and Kjaergaard, H. G.: Calculated Hydrogen Shift Rate Constants in Substituted Alkyl Peroxy Radicals, Journal of Physical Chemistry A, 122, 8665–8673, https://doi.org/10.1021/acs.jpca.8b06223, 2018.

Pankow, J. F. and Asher, W. E.: SIMPOL.1: a simple group contribution method for predicting vapor pressures and enthalpies of vaporization of multifunctional organic compounds, Atmospheric Chemistry and Physics, 8, 2773–2796, https://doi.org/10.5194/acp-8-2773-2008, 2008.

Park, J., Joo, B., Seo, H., Song, W., Lee, J. J., Lee, W. K., and Jang, H.: Analysis of wear induced particle emissions from brake pads during the worldwide harmonized light vehicles test procedure (WLTP), Wear, 466-467, 203 539, https://doi.org/10.1016/j.wear.2020.203539, 2021.

Peeters, J., Vereecken, L., and Fantechi, G.: The detailed mechanism of the OH-initiated atmospheric oxidation of α-pinene: a theoretical study, Phys. Chem. Chem. Phys., 3, 5489–5504, https://doi.org/10.1039/B106555F, 2001.

Peng, Z. and Jimenez, J. L.: KinSim: A Research-Grade, User-Friendly, Visual Kinetics Simulator for Chemical-Kinetics and Environmental-Chemistry Teaching, Journal of Chemical Education, 96, 806–811, https://doi.org/10.1021/acs.jchemed.9b00033, 2019.

Pichelstorfer, L., Stolzenburg, D., Ortega, J., Karl, T., Kokkola, H., Laakso, A., Lehtinen, K. E. J., Smith, J. N., McMurry, P. H., and Winkler, P. M.: Resolving nanoparticle growth mechanisms from size- and time-dependent growth rate analysis, Atmospheric Chemistry and Physics, 18, 1307–1323, https://doi.org/10.5194/acp-18-1307-2018, 2018.

Pierce, J. R. and Adams, P. J.: Uncertainty in global CCN concentrations from uncertain aerosol nucleation and primary emission rates, Atmos. Chem. Phys, 9, 1339–1356, 2009.

Pinto, D. M., Tiiva, P., Miettinen, P., Joutsensaari, J., Kokkola, H., Nerg, A.-M., Laaksonen, A., and Holopainen, J. K.: The effects of increasing atmospheric ozone on biogenic monoterpene profiles and the formation of secondary aerosols, Atmospheric Environment, 41, 4877–4887, https://doi.org/10.1016/j.atmosenv.2007.02.006, 2007.

Piscitello, A., Bianco, C., Casasso, A., and Sethi, R.: Non-exhaust traffic emissions: Sources, characterization, and mitigation measures, Science of The Total Environment, 766, 144 440, https://doi.org/10.1016/j.scitotenv.2020.144440, 2021.

Plachá, D., Vaculík, M., Mikeska, M., Dutko, O., Peikertová, P., Kukutschová, J., Kutláková, K. M., Růžičková, J., Tomášek, V., and Filip, P.: Release of volatile organic compounds by oxidative wear of automotive friction materials, Wear, 376-377, 705–716, https://doi.org/10.1016/j.wear.2016.12.016, 2017.

Riedel, T. P., Wagner, N. L., Dubé, W. P., Middlebrook, A. M., Young, C. J., Öztürk, F., Bahreini, R., VandenBoer, T. C., Wolfe, D. E., Williams, E. J., Roberts, J. M., Brown, S. S., and Thornton, J. A.: Chlorine activation within urban or power plant plumes: Vertically resolved ClNO ₂ and Cl ₂ measurements from a tall tower in a polluted continental setting, Journal of Geophysical Research: Atmospheres, 118, 8702–8715, https://doi.org/10.1002/jgrd.50637, 2013.

Rissanen, M., Kurtén, T., Sipilä, M., Thornton, J., Kangasluoma, J., Sarnela, N., Junninen, H., Jørgensen, S., Schallhart, S., Kajos, M., Taipale, R., Springer, M., Mentel, T., Ruuskanen, T., Petäjä, T., Worsnop, D., Kjaergaard, H., and Ehn, M.: The Formation of Highly Oxidized Multifunctional Products in the Ozonolysis of Cyclohexene, Journal of the American Chemical Society, 136, 15 596–15 606, https://doi.org/https://doi.org/10.1021/ja507146s, 2014.

Rissanen, M. P., Kurtén, T., Sipilä, M., Thornton, J. A., Kausiala, O., Garmash, O., Kjaergaard, H. G., Petäjä, T., Worsnop, D. R., Ehn, M., and Kulmala, M.: Effects of Chemical Complexity on the Autoxidation Mechanisms of Endocyclic Alkene Ozonolysis Products: From Methylcyclohexenes toward Understanding α-Pinene, The Journal of Physical Chemistry A, 119, 4633–4650, https://doi.org/10.1021/jp510966g, 2015.

Riva, G., Valota, G., Perricone, G., and Wahlström, J.: An FEA approach to simulate disc brake wear and airborne particle emissions, Tribology International, 138, 90–98, https://doi.org/10.1016/j.triboint.2019.05.035, 2019a.

Riva, M., Rantala, P., Krechmer, J. E., Peräkylä, O., Zhang, Y., Heikkinen, L., Garmash, O., Yan, C., Kulmala, M., Worsnop, D., and Ehn, M.: Evaluating the performance of five different chemical ionization techniques for detecting gaseous oxygenated organic species, Atmospheric Measurement Techniques, 12, 2403–2421, https://doi.org/10.5194/amt-12-2403-2019, 2019b.

Schervish, M. and Donahue, N. M.: Peroxy radical chemistry and the volatility basis set, Atmospheric Chemistry and Physics, 20, 1183–1199, https://doi.org/10.5194/acp-20-1183-2020, 2020.

Schraufnagel, D. E.: The health effects of ultrafine particles, Experimental Molecular Medicine, 52, 311–317, https://doi.org/10.1038/s12276-020-0403-3, 2020.

Shilling, J. E., Chen, Q., King, S. M., Rosenoern, T., Kroll, J. H., Worsnop, D. R., McKinney, K. A., and Martin, S. T.: Particle mass yield in secondary organic aerosol formed by the dark ozonolysis of α-pinene, Atmospheric Chemistry and Physics, 8, 2073–2088, https://doi.org/10.5194/acp-8-2073-2008, 2008.

Sindelarova, K., Granier, C., Bouarar, I., Guenther, A., Tilmes, S., Stavrakou, T., Müller, J. F., Kuhn, U., Stefani, P., and Knorr, W.: Global data set of biogenic VOC emissions calculated by

the MEGAN model over the last 30 years, Atmospheric Chemistry and Physics, 14, 9317–9341, https://doi.org/10.5194/acp-14-9317-2014, 2014.

Sipilä, M., Berndt, T., Petaja, T., Brus, D., Vanhanen, J., Stratmann, F., Patokoski, J., Mauldin III, R. L., Hyvarinen, A.-P., Lihavainen, H., and Kulmala, M.: The Role of Sulfuric Acid in Atmospheric Nucleation, Science, 327, 1243–1246, 2010.

Sipilä, M., Jokinen, T., Berndt, T., Richters, S., Makkonen, R., Donahue, N. M., III, R. L. M., Kurtén, T., Paasonen, P., Sarnela, N., Ehn, M., Junninen, H., Rissanen, M. P., Thornton, J., Stratmann, F., Herrmann, H., Worsnop, D. R., Kulmala, M., Kerminen, V.-M., and Petäjä, T.: Reactivity of stabilized Criegee intermediates (sCIs) from isoprene and monoterpene ozonolysis toward SOamp;lt;subamp;gt;2amp;lt;/subamp;gt; and organic acids, Atmospheric Chemistry and Physics, 14, 12 143–12 153, https://doi.org/10.5194/acp-14-12143-2014, 2014.

Smith, J. N., Dunn, M. J., VanReken, T. M., Iida, K., Stolzenburg, M. R., McMurry, P. H., and Huey, L. G.: Chemical composition of atmospheric nanoparticles formed from nucleation in Tecamac, Mexico: Evidence for an important role for organic species in nanoparticle growth, Geophysical Research Letters, 35, L04 808, https://doi.org/10.1029/2007GL032523, 2008.

Smith, N. R., Crescenzo, G. V., Huang, Y., Hettiyadura, A. P. S., Siemens, K., Li, Y., Faiola, C. L., Laskin, A., Shiraiwa, M., Bertram, A. K., and Nizkorodov, S. A.: Viscosity and liquid–liquid phase separation in healthy and stressed plant SOA, Environmental Science: Atmospheres, 1, 140–153, https://doi.org/10.1039/D0EA00020E, 2021.

Song, M., Zhao, X., Liu, P., Mu, J., He, G., Zhang, C., Tong, S., Xue, C., Zhao, X., Ge, M., and Mu, Y.: Atmospheric NOx oxidation as major sources for nitrous acid (HONO), npj Climate and Atmospheric Science, 6, 30, https://doi.org/10.1038/s41612-023-00357-8, 2023.

Spracklen, D. V., Carslaw, K. S., Kulmala, M., Kerminen, V.-M., Sihto, S.-L., Riipinen, I., Merikanto, J., Mann, G. W., Chipperfield, M. P., Wiedensohler, A., Birmili, W., and Lihavainen, H.: Contribution of particle formation to global cloud condensation nuclei concentrations, Geophysical Research Letters, 35, L06 808, https://doi.org/10.1029/2007GL033038, 2008.

Srivastava, D., Vu, T. V., Tong, S., Shi, Z., and Harrison, R. M.: Formation of secondary organic aerosols from anthropogenic precursors in laboratory studies, npj Climate and Atmospheric Science, 5, 22, https://doi.org/10.1038/s41612-022-00238-6, 2022.

Stark, H., Yatavelli, R. L., Thompson, S. L., Kimmel, J. R., Cubison, M. J., Chhabra, P. S., Canagaratna, M. R., Jayne, J. T., Worsnop, D. R., and Jimenez, J. L.: Methods to extract molecular and bulk chemical information from series of complex mass spectra with limited mass resolution, International Journal of Mass Spectrometry, 389, 26–38, https://doi.org/https://doi.org/10.1016/j.ijms.2015.08.011, 2015.

Stocker, T., Qin, D., Plattner, M., Tignor, S., Allen, J., Boschung, A., Nauels, Y., Xia, V., Midgley, B., and P.M.: Climate Change 2013: The Physical Science Basis. Contribution of Working Group I to the Fifth Assessment Report of the Intergovernmental Panel on Climate Change, Cambridge University Press, p. 1535, 2013a.

Stocker, T., Qin, D., Plattner, M., Tignor, S., Allen, J., Boschung, A., Nauels, Y., Xia, V., Midgley, B., and P.M.: Climate Change 2013: The Physical Science Basis. Contribution of Working Group

I to the Fifth Assessment Report of the Intergovernmental Panel on Climate Change, Cambridge University Press, p. 1535, 2013b.

Tessum, C. W., Paolella, D. A., Chambliss, S. E., Apte, J. S., Hill, J. D., and Marshall, J. D.: PM 2.5 polluters disproportionately and systemically affect people of color in the United States, Science Advances, 7, https://doi.org/10.1126/sciadv.abf4491, 2021.

Thomsen, D., Elm, J., Rosati, B., Skønager, J. T., Bilde, M., and Glasius, M.: Large Discrepancy in the Formation of Secondary Organic Aerosols from Structurally Similar Monoterpenes, ACS Earth and Space Chemistry, 5, 632–644, https://doi.org/10.1021/acsearthspacechem.0c00332, 2021.

Trostl, J., Chuang, W., Gordon, H., Heinritzi, M., Yan, C., Molteni, U., Ahlm, L., Frege, C., Bianchi, F., Wagner, R., et al.: The role of low-volatility organic compounds in initial particle growth in the atmosphere, Nature, 533, 527, 2016.

Vereecken, L. and Francisco, J. S.: Theoretical studies of atmospheric reaction mechanisms in the troposphere, Chem. Soc. Rev., 41, 6259–6293, https://doi.org/10.1039/C2CS35070J, 2012.

Vereecken, L. and Nozière, B.: H migration in peroxy radicals under atmospheric conditions, Atmospheric Chemistry and Physics, 20, https://doi.org/10.5194/acp-20-7429-2020, 2020.

Vereecken, L. and Peeters, J.: Decomposition of substituted alkoxy radicals - Part I: A generalized structure-activity relationship for reaction barrier heights, Physical Chemistry Chemical Physics, 11, 9062–9074, https://doi.org/10.1039/b909712k, 2009.

Vereecken, L. and Peeters, J.: A structure-activity relationship for the rate coefficient of H-migration in substituted alkoxy radicals, Physical Chemistry Chemical Physics, 12, 12 608–12 620, https://doi.org/10.1039/c0cp00387e, 2010.

Vereecken, L. and Peeters, J.: A theoretical study of the OH-initiated gas-phase oxidation mechanism of α-pinene (C10H16): first generation products, Phys. Chem. Chem. Phys., 14, 3802–3815, https://doi.org/10.1039/C2CP23711C, 2012.

Vereecken, L., Vu, G., Wahner, A., Kiendler-Scharr, A., and Nguyen, H. M. T.: A structure activity relationship for ring closure reactions in unsaturated alkylperoxy radicals, Physical Chemistry Chemical Physics, 23, https://doi.org/10.1039/D1CP02758A, 2021.

Wang, X., Jacob, D. J., Eastham, S. D., Sulprizio, M. P., Zhu, L., Chen, Q., Alexander, B., Sherwen, T., Evans, M. J., Lee, B. H., Haskins, J. D., Lopez-Hilfiker, F. D., Thornton, J. A., Huey, G. L., and Liao, H.: The role of chlorine in global tropospheric chemistry, Atmospheric Chemistry and Physics, 19, 3981–4003, https://doi.org/10.5194/acp-19-3981-2019, 2019.

Weber, R. J., McMurry, P. H., Eisele, F. L., and Tanner, D. J.: Measurement of Expected Nucleation Precursor Species and 3–500-nm Diameter Particles at Mauna Loa Observatory, Hawaii, Journal of the Atmospheric Sciences, 52, 2242–2257, 1995.

Westervelt, D. M., Pierce, J. R., Riipinen, I., Trivitayanurak, W., Hamed, A., Kulmala, M., Laaksonen, A., Decesari, S., and Adams, P. J.: Formation and growth of nucleated particles into cloud condensation nuclei: Model-measurement comparison, Atmospheric Chemistry and Physics, 13, 7645–7663, https://doi.org/10.5194/acp-13-7645-2013, 2013.

Whitby, K. T.: The physical characteristics of sulfur aerosols, Atmospheric Environment, 12, 135–159, https://doi.org/10.1016/j.atmosenv.2007.10.057, 1978.

Whytlaw-Gray, R., Speakman, J., and Campbell, J.: Smokes: Part I.—A study of their behaviour and a method of determining the number of particles they contain, Proceedings of the Royal Society of London. Series A, Containing Papers of a Mathematical and Physical Character, 102, 600–615, https://doi.org/10.1098/rspa.1923.0018, 1923.

Xavier, C., Rusanen, A., Zhou, P., Dean, C., Pichelstorfer, L., Roldin, P., and Boy, M.: Aerosol mass yields of selected biogenic volatile organic compounds – a theoretical study with nearly explicit gas-phase chemistry, Atmospheric Chemistry and Physics, 19, 13 741–13 758, https://doi.org/10.5194/acp-19-13741-2019, 2019.

Xie, H. B., Elm, J., Halonen, R., Myllys, N., Kurtén, T., Kulmala, M., and Vehkamäki, H.: Atmospheric Fate of Monoethanolamine: Enhancing New Particle Formation of Sulfuric Acid as an Important Removal Process, Environmental Science and Technology, 51, 8422–8431, https://doi.org/10.1021/acs.est.7b02294, 2017.

Xu, L., Møller, K. H., Crounse, J. D., Otkjær, R. V., Kjaergaard, H. G., and Wennberg, P. O.: Unimolecular Reactions of Peroxy Radicals Formed in the Oxidation of -Pinene and -Pinene by Hydroxyl Radicals, The Journal of Physical Chemistry A, 123, 1661–1674, https://doi.org/10.1021/acs.jpca.8b11726, 2019.

Yao, L., Fan, X., Yan, C., Kurtén, T., Daellenbach, K. R., Li, C., Wang, Y., Guo, Y., Dada, L., Rissanen, M. P., Cai, J., Tham, Y. J., Zha, Q., Zhang, S., Du, W., Yu, M., Zheng, F., Zhou, Y., Kontkanen, J., Chan, T., Shen, J., Kujansuu, J. T., Kangasluoma, J., Jiang, J., Wang, L., Worsnop, D. R., Petäjä, T., Kerminen, V.-M., Liu, Y., Chu, B., He, H., Kulmala, M., and Bianchi, F.: Unprecedented Ambient Sulfur Trioxide (SO3) Detection: Possible Formation Mechanism and Atmospheric Implications, Environmental Science Technology Letters, 7, 809–818, https://doi.org/10.1021/acs.estlett.0c00615, 2020.

Ye, P., Ding, X., Hakala, J., Hofbauer, V., Robinson, E. S., and Donahue, N. M.: Vapor wall loss of semi-volatile organic compounds in a Teflon chamber, Aerosol Science and Technology, 50, 822–834, https://doi.org/10.1080/02786826.2016.1195905, 2016.

Zauner-Wieczorek, M., Heinritzi, M., Granzin, M., Keber, T., Kürten, A., Kaiser, K., Schneider, J., and Curtius, J.: Mass spectrometric measurements of ambient ions and estimation of gaseous sulfuric acid in the free troposphere and lowermost stratosphere during the CAFE-EU/BLUESKY campaign, Atmospheric Chemistry and Physics, 22, 11 781–11 794, https://doi.org/10.5194/acp-22-11781-2022, 2022.

Zhang, H., Yee, L. D., Lee, B. H., Curtis, M. P., Worton, D. R., Isaacman-VanWertz, G., Offenberg, J. H., Lewandowski, M., Kleindienst, T. E., Beaver, M. R., Holder, A. L., Lonneman, W. A., Docherty, K. S., Jaoui, M., Pye, H. O., Hu, W., Day, D. A., Campuzano-Jost, P., Jimenez, J. L., Guo, H., Weber, R. J., De Gouw, J., Koss, A. R., Edgerton, E. S., Brune, W., Mohr, C., Lopez-Hilfiker, F. D., Lutz, A., Kreisberg, N. M., Spielman, S. R., Hering, S. V., Wilson, K. R., Thornton, J. A., and Goldstein, A. H.: Monoterpenes are the largest source of summertime organic aerosol in the southeastern United States, Proceedings of the National Academy of Sciences of the United States of America, 115, 2038–2043, https://doi.org/10.1073/pnas.1717513115, 2018.

Zhang, R., Khalizov, A., Wang, L., Hu, M., and Xu, W.: Nucleation and Growth of Nanoparticles in the Atmosphere, Chemical Reviews, 112, 1957–2011, https://doi.org/10.1021/cr2001756, 2012.

Zhang, W. and Zhang, H.: Secondary Ion Chemistry Mediated by Ozone and Acidic Organic Molecules in Iodide-Adduct Chemical Ionization Mass Spectrometry, Analytical Chemistry, 93, https://doi.org/10.1021/acs.analchem.1c01486, 2021.

Zhao, D. F., Kaminski, M., Schlag, P., Fuchs, H., Acir, I.-H., Bohn, B., Häseler, R., Kiendler-Scharr, A., Rohrer, F., Tillmann, R., Wang, M. J., Wegener, R., Wildt, J., Wahner, A., and Mentel, T. F.: Secondary organic aerosol formation from hydroxyl radical oxidation and ozonolysis of monoterpenes, Atmospheric Chemistry and Physics, 15, 991–1012, https://doi.org/10.5194/acp-15-991-2015, 2015.

Zhao, J., Ortega, J., Chen, M., McMurry, P. H., and Smith, J. N.: Dependence of particle nucleation and growth on high-molecular-weight gas-phase products during ozonolysis of α-pinene, Atmospheric Chemistry and Physics, 13, 7631–7644, https://doi.org/10.5194/acp-13-7631-2013, 2013.

Zhao, Y., Thornton, J. A., and Pye, H. O. T.: Quantitative constraints on autoxidation and dimer formation from direct probing of monoterpene-derived peroxy radical chemistry, Proceedings of the National Academy of Sciences, 115, 12 142–12 147, https://doi.org/10.1073/pnas.1812147115, 2018.

Ziemann, P. J. and Atkinson, R.: Kinetics, products, and mechanisms of secondary organic aerosol formation, Chemical Society Reviews, 41, 6582, https://doi.org/10.1039/c2cs35122f, 2012.

zum Hagen, F. H. F., Mathissen, M., Grabiec, T., Hennicke, T., Rettig, M., Grochowicz, J., Vogt, R., and Benter, T.: On-road vehicle measurements of brake wear particle emissions, Atmospheric Environment, 217, 116 943, https://doi.org/10.1016/j.atmosenv.2019.116943, 2019.

Appendix A

Chapter 3 Peak Lists

d-carene peak list														
HR Peak ID (NO_3- cluster)	m/Q	normalized intensity	HR Peak ID (NO_3- cluster)	m/Q	normalized intensity	HR Peak ID (NO_3- cluster)	m/Q	normalized intensity	HR Peak ID (NO_3- cluster)	m/Q	normalized intensity	HR Peak ID (NO_3- cluster)	m/Q	normalized intensity
NO3	61.988	6.00E+10	C10H15N2O14	387.052	1.31E+07	C7H10N3O11	312.032	3.66E+06	C19H30N2O15	526.165	1.35E+06	C16H26N3O15	500.136	2.70E+05
HN2O6	124.983	2.25E+10	C19H15NO12	449.059	1.23E+07	C20H31N2O14	523.178	3.66E+06	C19H29N4O17	585.153	1.35E+06	C17H28N3O15	514.152	2.15E+05
C20H32N3O17	586.173	3.53E+08	H2N3O9	187.979	1.22E+07	C18H28N3O16	542.147	3.63E+06	C20H31N2O13	507.183	1.35E+06	C19H29N4O22	665.127	1.92E+05
C20H32N3O16	570.178	2.73E+08	C20H33N4O20	649.169	1.14E+07	C10H17N2O14	389.068	3.45E+06	C18H30N3O14	512.173	1.34E+06	C18H30N3O13	496.178	1.73E+05
C10H16N2O13	372.065	2.70E+08	C9H16N3O13	374.068	1.10E+07	C20H31N3O18	601.160	3.35E+06	C17H26N4O15	526.139	1.28E+06			
C9H14N3O15	404.042	2.30E+08	C20H32N3O21	650.153	1.10E+07	C20H32N5O20	662.164	3.30E+06	C16H24N3O16	514.116	1.24E+06			
C20H32N3O19	618.163	1.53E+08	C9H13N2O10	309.057	1.04E+07	C10H14NO9	292.067	3.19E+06	C18H30N4O17	574.161	1.22E+06			
C10H16N2O11	340.075	1.43E+08	C18H28N4O17	572.145	1.01E+07	C10H15N3O12	369.066	3.19E+06	C20H32N4O19	632.166	1.22E+06			
C20H32N3O14	538.188	1.40E+08	C20H32NO17	558.167	9.91E+06	C10H16N3O17	450.048	3.19E+06	C18H30N3O18	576.152	1.21E+06			
C10H15N2O10	323.073	1.27E+08	C20H32N3O20	634.158	9.58E+06	C18H28N2O17	544.139	3.01E+06	C20H32N5O21	678.159	1.19E+06			
C19H30N3O16	556.163	1.09E+08	C20H31N4O20	647.153	9.55E+06	C19H30N3O13	508.178	2.99E+06	C19H32N3O18	590.168	1.11E+06			
C10H17N2O12	357.078	7.06E+07	C9H15N2O12	343.062	9.45E+06	C20H32N2O15	540.180	2.96E+06	C20H31N4O21	663.148	1.07E+06			
C9H13N2O11	325.052	7.00E+07	C10H16N3O14	402.063	8.65E+06	C9H12NO9	278.051	2.94E+06	C17H26N4O18	574.124	1.02E+06			
C10H16N3O15	418.058	5.77E+07	C20H31N4O18	615.163	8.24E+06	C20H32N3O13	522.194	2.88E+06	C16H24N3O18	546.105	1.02E+06			
C20H31N4O17	599.168	5.28E+07	C7H11N2O11	299.036	8.21E+06	C17H26N3O15	512.136	2.63E+06	C19H29N4O16	569.158	9.55E+05			
C20H32N3O15	554.183	5.05E+07	C10H16N2O14	388.060	6.59E+06	C20H33NO17	559.175	2.46E+06	C18H28N3O13	494.162	8.50E+05			
C10H15N2O12	355.062	4.61E+07	C19H13NO12	447.044	6.18E+06	C15H22N3O17	516.095	2.40E+06	C19H29N3O21	635.129	8.47E+05			
C10H17N2O13	373.073	4.35E+07	C9H15N2O11	327.068	6.08E+06	C19H32N3O19	606.163	2.39E+06	C10H17N3O12	371.081	7.73E+05			
C20H32N3O18	602.168	3.81E+07	C20H32N2O17	572.170	5.95E+06	C20H31N4O15	567.179	2.33E+06	C18H28N3O19	590.132	7.55E+05			
C10H16N3O13	386.068	3.01E+07	C9H15N2O9	295.078	5.74E+06	C20H30N3O19	616.147	2.13E+06	C20H30N3O20	632.142	7.55E+05			
C10H15N3O14	401.055	2.83E+07	C9H12NO8	262.056	5.18E+06	C20H32N3O12	506.199	2.11E+06	C16H24N4O19	576.103	7.47E+05			
C19H30N3O14	524.173	2.65E+07	C9H13N2O9	293.062	4.97E+06	C17H26N3O18	560.121	2.09E+06	C20H33N4O21	665.164	7.47E+05			
C10H14N3O13	384.053	2.12E+07	C20H33N4O19	633.174	4.79E+06	C20H33N4O15	569.194	1.98E+06	C19H32N2O16	544.175	7.18E+05			
C10H16NO9	294.083	2.04E+07	C10H16N3O12	370.073	4.71E+06	C20H31N4O16	583.174	1.76E+06	C20H32N3O22	666.148	6.13E+05			
C10H16N2O12	356.070	1.80E+07	C20H32N3O11	490.204	4.40E+06	C19H32N3O15	542.183	1.70E+06	C20H33N2O12	493.203	5.64E+05			
C10H15N2O13	371.057	1.60E+07	C19H29N2O14	509.162	4.20E+06	C10H16N2O9	308.086	1.58E+06	C20H33N4O22	681.159	5.18E+05			
C10H15N2O11	339.068	1.59E+07	C10H14NO10	308.062	4.09E+06	C20H33N4O16	585.189	1.49E+06	C17H26N3O14	496.141	5.15E+05			
C10H17N3O14	403.071	1.51E+07	C19H31N4O15	555.179	3.99E+06	C19H30N3O21	636.137	1.45E+06	C15H22N3O16	500.100	5.05E+05			
C9H14N2O11	326.060	1.48E+07	C10H16N2O16	420.050	3.97E+06	C20H30N3O15	552.168	1.39E+06	C19H31NO16	529.164	5.00E+05			
C20H33N4O18	617.179	1.46E+07	C20H31N4O19	631.158	3.97E+06	C20H31N4O22	679.143	1.38E+06	C19H27N3O21	633.114	4.25E+05			
C19H30N3O19	604.147	1.45E+07	C20H30N3O17	584.158	3.94E+06	C19H30N2O14	510.170	1.38E+06	C18H30N3O17	560.158	3.45E+05			
C20H33N4O17	601.184	1.45E+07	C10H15N3O13	385.060	3.76E+06	C18H30N4O19	606.150	1.37E+06	C19H29N2O13	493.167	3.24E+05			

β-pinene peak list											
HR Peak ID (NO_3- cluster)	m/Q	normalized intensity	HR Peak ID (NO_3- cluster)	m/Q	normalized intensity	HR Peak ID (NO_3- cluster)	m/Q	normalized intensity	HR Peak ID (NO_3- cluster)	m/Q	normalized intensity
NO3	61.988	6.00E+10	C20H32N3O18	602.168	5.44E+06	C9H15N3O11	341.071	1.54E+06	C9H11N2O10	307.041	5.15E+05
HN2O6	124.983	1.95E+10	C7H10N3O14	360.016	5.03E+06	C20H33N3O19	619.171	1.49E+06	C20H33N2O15	541.188	4.95E+05
C7H9N2O11	297.021	8.98E+07	C10H17N3O15	419.066	4.39E+06	C20H33N3O18	603.176	1.43E+06	C9H13N2O9	293.062	4.91E+05
C10H16N2O12	356.070	5.76E+07	C10H16N3O13	386.068	4.19E+06	C9H16N2O12	344.070	1.43E+06	C9H6N2O12	333.992	4.87E+05
C10H15N2O13	371.057	4.95E+07	C20H31N4O18	615.163	4.11E+06	C19H32N3O16	558.178	1.30E+06	C9H15N2O13	359.057	4.71E+05
C20H32N3O16	570.178	4.87E+07	C10H16N3O15	418.058	3.87E+06	C7H10N2O14	346.013	1.27E+06	C10H13N2O11	337.052	4.59E+05
C20H32N3O13	522.194	4.79E+07	C10H16N3O14	402.063	3.73E+06	C20H24N4O11	496.144	1.23E+06	C10H16N3O11	354.078	4.35E+05
C7H10N2O12	314.023	2.68E+07	C10H16N3O12	370.073	3.48E+06	C10H14N3O12	368.058	1.21E+06	C10H17N2O15	405.063	3.96E+05
C17H26N3O15	512.136	2.67E+07	C10H17N2O13	373.073	3.26E+06	C10H16N2O16	420.050	1.18E+06	C9H16N3O13	374.068	3.40E+05
C20H32N3O15	554.183	2.53E+07	C9H13N2O11	325.052	3.13E+06	C20H32N2O15	540.180	1.17E+06	C10H14NO9	292.067	2.79E+05
C20H32N3O17	586.173	2.27E+07	C10H16N2O13	372.065	3.09E+06	C7H10N3O11	312.032	1.14E+06	C10H15N3O13	385.060	2.79E+05
C10H15N2O11	339.068	2.20E+07	C19H32N3O13	510.194	2.96E+06	C10H17N4O17	465.059	1.10E+06	C19H31N3O16	557.170	2.77E+05
C19H32N3O15	542.183	1.85E+07	C10H14N3O14	400.048	2.79E+06	C19H29N2O15	525.157	1.02E+06	C10H16NO9	294.083	2.73E+05
C10H15N2O12	355.062	1.68E+07	C19H32N3O14	526.188	2.69E+06	C20H33N2O17	573.178	1.00E+06	C19H30N5O17	600.164	2.58E+05
C10H16N2O11	340.075	1.43E+07	C10H14N3O16	432.037	2.63E+06	C20H30N3O16	568.163	9.30E+05	C19H29N2O16	541.152	2.40E+05
C9H15N2O11	327.068	1.36E+07	C17H26N3O13	480.147	2.50E+06	C20H32N3O20	634.158	9.30E+05	C10H15N3O12	369.066	2.32E+05
C10H16N2O14	388.060	1.31E+07	C20H32N3O12	506.199	2.44E+06	C20H31N4O17	599.168	9.14E+05	C9H12NO9	278.051	1.96E+05
C20H32N3O14	538.188	1.22E+07	C17H26N3O19	576.116	2.03E+06	C10H16N2O15	404.055	8.90E+05	C9H12NO8	262.056	1.15E+05
C17H35N2O16	523.199	1.16E+07	C20H32N2O17	572.170	1.99E+06	C9H13N2O10	309.057	8.86E+05			
C7H9N2O13	329.010	9.58E+06	C20H32N2O16	556.175	1.98E+06	C20H31N4O19	631.158	8.70E+05			
C17H26N3O17	544.126	8.98E+06	C9H14N2O12	342.055	1.96E+06	C9H15N2O9	295.078	8.17E+05			
C10H17N2O12	357.078	8.98E+06	C10H16N3O16	434.053	1.85E+06	C20H33N4O17	601.184	7.93E+05			
C17H26N3O16	528.131	7.49E+06	C19H29N2O13	493.167	1.83E+06	C10H14N3O13	384.053	7.65E+05			
C10H15N2O15	403.047	6.56E+06	C10H16NO13	358.062	1.79E+06	C10H14N3O15	416.042	7.61E+05			
C10H15N2O14	387.052	6.44E+06	C9H15N2O12	343.062	1.72E+06	C20H33N4O18	617.179	7.13E+05			
C10H15N2O10	323.073	6.12E+06	C20H33N4O16	585.189	1.67E+06	C10H15N3O14	401.055	7.05E+05			
C20H32N3O19	618.163	6.12E+06	C10H15N3O15	417.050	1.65E+06	C20H31N4O16	583.174	6.89E+05			
C10H16N2O10	324.080	6.04E+06	C19H32N3O17	574.173	1.61E+06	C10H17N2O14	389.068	5.80E+05			
C20H33N3O17	587.181	5.48E+06	C10H15N2O9	307.078	1.61E+06	C20H31N4O15	567.179	5.32E+05			

α-thujene peak list															
HR Peak ID (NO_3- cluster)	m/Q	normalized intensity	HR Peak ID (NO_3- cluster)	m/Q	normalized intensity	HR Peak ID (NO_3- cluster)	m/Q	normalized intensity	HR Peak ID (NO_3- cluster)	m/Q	normalized intensity	HR Peak ID (NO_3- cluster)	m/Q	normalized intensity
NO3	61.988	6.00E+10	C10H15N2O16	419.042	3.95E+06	C9H13N2O12	341.047	1.63E+06	C20H33NO16	543.180	9.95E+05	C10H14N3O15	416.042	5.67E+05
HN2O6	124.983	1.86E+10	C20H32N3O19	618.163	3.55E+06	C10H14NO9	292.067	1.59E+06	C9H14N2O14	374.045	9.91E+05	C9H16NO10	298.077	5.41E+05
H2N3O9	187.979	1.42E+07	C10H15N2O10	323.073	3.46E+06	C19H29N2O13	493.167	1.58E+06	C19H28NO16	526.141	9.88E+05	C17H26N3O19	576.116	5.41E+05
C10H15N2O12	355.062	1.90E+08	C9H16N3O14	390.063	3.36E+06	C19H32N3O20	622.158	1.56E+06	C9H15N2O14	375.052	9.65E+05	C10H16N3O17	450.048	5.35E+05
C10H15N2O13	371.057	1.21E+08	C9H16N2O11	328.075	3.29E+06	C19H31N3O14	525.181	1.54E+06	C20H30N3O18	600.152	9.55E+05	C18H30N2O17	546.154	5.28E+05
C20H32N3O18	602.168	9.13E+07	C20H32N3O13	522.194	3.26E+06	C10H15NO12	341.059	1.53E+06	C19H33N2O15	529.188	9.46E+05	C19H29NO15	511.154	5.12E+05
C10H16N2O13	372.065	8.71E+07	C8H12NO12	314.036	3.21E+06	C10H13N2O12	353.047	1.47E+06	C10H14N3O12	368.058	9.36E+05	C19H32N2O18	576.165	4.89E+05
C10H15N2O14	387.052	4.17E+07	C20H31N2O14	523.178	3.12E+06	C20H31NO16	541.164	1.47E+06	C17H26N3O16	528.131	9.13E+05	C20H31N4O17	599.168	4.89E+05
C20H32N3O16	570.178	3.04E+07	C20H31N2O17	571.162	3.06E+06	C9H14NO7	248.077	1.45E+06	C10H13N2O11	337.052	8.61E+05	C10H15N3O14	401.055	4.73E+05
C9H16N2O12	344.070	2.98E+07	C20H31N2O18	587.157	2.86E+06	C20H30N3O17	584.158	1.45E+06	C20H33N4O21	665.164	8.38E+05	C20H33NO14	511.190	4.66E+05
C20H32N3O15	554.183	2.90E+07	C10H15N2O15	403.047	2.82E+06	C10H16N3O13	386.068	1.37E+06	C8H12N2O12	328.039	8.15E+05	C10H17N2O15	405.063	4.57E+05
C19H30N3O17	572.158	2.58E+07	C19H31N4O15	555.179	2.68E+06	C20H33N4O18	617.179	1.32E+06	C19H32N3O13	510.194	8.09E+05	C9H13N2O9	293.062	4.34E+05
C19H32N3O17	574.173	1.95E+07	C19H30N3O15	540.168	2.58E+06	C7H9N2O13	329.010	1.30E+06	C20H30N3O20	632.142	8.02E+05	C8H11N2O10	295.041	4.04E+05
C10H16N3O15	418.058	1.90E+07	C9H15N2O13	359.057	2.57E+06	C19H28N2O17	556.139	1.28E+06	C18H29N2O14	497.162	7.89E+05	C20H33NO17	559.175	4.01E+05
C10H17N2O12	357.078	1.56E+07	C19H32N3O14	526.188	2.52E+06	C10H14N2O12	354.055	1.27E+06	C19H29NO18	559.138	7.73E+05	C10H17N3O16	435.061	3.75E+05
C9H15N2O11	327.068	1.48E+07	C20H32N3O21	650.153	2.50E+06	C20H30N3O16	568.163	1.27E+06	C10H16N2O16	420.050	7.73E+05	C18H27NO17	529.128	3.55E+05
C10H15N2O11	339.068	1.45E+07	C10H15NO11	325.065	2.44E+06	C18H30N3O17	560.158	1.25E+06	C9H16N3O13	374.068	7.50E+05	C19H33N2O13	497.198	3.52E+05
C19H32N3O15	542.183	1.23E+07	C19H30N3O18	588.152	2.41E+06	C9H5N3O7	267.013	1.24E+06	C9H12N3O13	370.037	7.14E+05	C8H11N2O14	359.021	3.52E+05
C20H33N2O13	509.198	8.74E+06	C9H16N3O12	358.073	2.27E+06	C10H16N3O16	434.053	1.23E+06	C20H31N3O17	585.165	6.65E+05	C19H31N2O20	607.147	3.46E+05
C9H15N2O10	311.073	8.25E+06	C19H32N3O19	606.163	2.19E+06	C9H11N2O11	323.036	1.21E+06	C7H10N2O13	330.018	6.65E+05	C17H26NO16	500.125	2.90E+05
C9H17N2O11	329.083	7.86E+06	C10H15NO15	389.044	2.14E+06	C10H16N3O12	370.073	1.20E+06	C9H13N2O10	309.057	6.62E+05	C7H11N2O11	299.036	2.58E+05
C20H32N3O17	586.173	7.86E+06	C19H31N2O15	527.172	2.03E+06	C9H17N2O12	345.078	1.18E+06	C19H29N2O20	605.131	6.62E+05	C9H12NO8	262.056	2.37E+05
C19H32N3O16	558.178	7.34E+06	C19H30N3O20	620.142	2.01E+06	C20H31N2O21	635.142	1.15E+06	C18H26NO19	560.110	6.59E+05	C10H16NO9	294.083	2.29E+05
C7H9N2O11	297.021	5.67E+06	C10H16N2O15	404.055	1.97E+06	C19H29NO17	543.144	1.14E+06	C19H31N2O12	479.188	6.49E+05	C19H29NO16	527.149	2.26E+05
C19H30N3O14	524.173	5.48E+06	C20H32N3O14	538.188	1.93E+06	C10H14NO11	324.057	1.13E+06	C20H33N2O19	605.168	6.33E+05	C19H34N2O16	546.191	1.70E+05
C20H33N2O16	557.183	5.45E+06	C20H32N2O19	604.160	1.87E+06	C10H16NO11	326.072	1.07E+06	C19H30NO16	528.156	6.29E+05			
C9H14N3O11	340.063	5.18E+06	C10H14NO10	308.062	1.82E+06	C9H14N2O13	358.050	1.03E+06	C9H15N2O9	295.078	6.23E+05			
C10H15NO13	357.054	5.02E+06	C20H32N2O16	556.175	1.81E+06	C10H16NO12	342.067	1.03E+06	C10H16N2O10	324.080	6.23E+05			
C9H15N2O12	343.062	4.92E+06	C20H31N2O15	539.172	1.79E+06	C8H11N3O15	389.019	1.03E+06	C10H14N3O14	400.048	6.20E+05			
C18H30N3O16	544.163	4.37E+06	C10H16N2O14	388.060	1.76E+06	C9H15NO10	297.070	1.01E+06	C10H14N3O13	384.053	6.20E+05			
C19H32N3O18	590.168	4.01E+06	C20H33N2O11	477.208	1.74E+06	C10H16N3O14	402.063	1.01E+06	C9H15N3O16	421.045	6.13E+05			
C10H17N2O13	373.073	3.95E+06	C20H32N3O20	634.158	1.71E+06	C10H14N3O16	432.037	9.98E+05	C9H16N2O13	360.065	5.71E+05			

α-pinene peak list								
HR Peak ID (NO_3- cluster)	m/Q	normalized intensity	HR Peak ID (NO_3- cluster)	m/Q	normalized intensity	HR Peak ID (NO_3- cluster)	m/Q	normalized intensity
NO3	61.988	6.00E+10	C10H15NO12	341.059	6.84E+05	C9H15N2O9	295.078	2.82E+05
HN2O6	124.983	1.89E+10	C20H31N2O16	555.167	6.37E+05	C10H15N3O12	369.066	2.49E+05
H2N3O9	187.979	1.16E+07	C9H11N2O10	307.041	6.17E+05	C10H16N2O16	420.050	2.47E+05
C7H9N2O11	297.021	3.08E+07	C7H10N3O13	344.021	6.04E+05	C9H15N2O11	327.068	2.45E+05
C10H16N2O12	356.070	6.06E+06	C20H31N2O17	571.162	5.79E+05	C10H17N2O12	357.078	2.43E+05
C7H9N2O13	329.010	2.22E+06	C10H15N2O10	323.073	5.46E+05	C20H30NO18	572.146	2.43E+05
C10H14NO12	340.052	1.73E+06	C10H15N2O11	339.068	5.46E+05	C20H32N2O15	540.180	2.37E+05
C18H26NO18	544.115	1.67E+06	C10H16N3O14	402.063	5.46E+05	C19H30N3O16	556.163	2.37E+05
C20H32N3O17	586.173	1.45E+06	C10H14N2O12	354.055	5.36E+05	C9H15N2O12	343.062	1.91E+05
C10H15N2O13	371.057	1.37E+06	C10H14NO10	308.062	5.33E+05	C10H16N3O15	418.058	1.89E+05
C10H15N2O15	403.047	1.36E+06	C9H14N2O15	390.039	5.21E+05	C9H13N2O9	293.062	1.75E+05
C7H10N2O12	314.023	1.31E+06	C10H16N3O13	386.068	5.10E+05	C19H13NO12	447.044	1.75E+05
C10H16N2O14	388.060	1.17E+06	C10H14N3O12	368.058	5.05E+05	C19H30N5O17	600.164	1.70E+05
C10H16N3O17	450.048	1.15E+06	C20H31N2O14	523.178	4.67E+05	C9H14N2O11	326.060	1.32E+05
C9H14N3O13	372.053	1.10E+06	C10H15N2O12	355.062	4.64E+05	C9H12NO9	278.051	1.01E+05
C10H14N3O15	416.042	1.09E+06	C10H14N3O16	432.037	4.58E+05	C10H14NO9	292.067	9.83E+04
C20H32N3O15	554.183	1.06E+06	C10H14NO11	324.057	4.34E+05	C9H12NO8	262.056	8.92E+04
C10H14N2O13	370.050	1.03E+06	C7H10N2O13	330.018	4.09E+05	C10H16NO9	294.083	8.52E+04
C9H14N2O13	358.050	1.02E+06	C10H15N3O15	417.050	4.07E+05	C10H16N2O9	308.086	0.00E+00
C20H32N3O16	570.178	1.00E+06	C10H15N2O14	387.052	3.98E+05	C10H17N3O12	371.081	0.00E+00
C20H32N3O13	522.194	9.55E+05	C20H31N2O18	587.157	3.96E+05			
C9H14N3O15	404.042	9.27E+05	C10H15N3O14	401.055	3.89E+05			
C10H15NO14	373.049	9.12E+05	C10H16N2O10	324.080	3.76E+05			
C20H32N3O14	538.188	8.82E+05	C10H15N3O13	385.060	3.76E+05			
C20H32N3O19	618.163	8.47E+05	C9H13N2O10	309.057	3.53E+05			
C20H32N3O18	602.168	8.41E+05	C10H17N2O14	389.068	3.42E+05			
C7H10N3O11	312.032	7.96E+05	C19H30N2O18	574.149	3.38E+05			
C9H13N2O11	325.052	7.96E+05	C10H14N3O13	384.053	3.20E+05			
C10H15N2O9	307.078	6.97E+05	C20H31N2O20	619.147	2.97E+05			

Figure A.1: Peak lists for each MT system

.